Journal of Medicinal Chemistry

pubs.acs.org/jmc

Article

Identification of Transthyretin Tetramer Kinetic Stabilizers That Are Capable of Inhibiting the Retinol-Dependent Retinol Binding Protein 4-Transthyretin Interaction: Potential Novel Therapeutics for Macular Degeneration, Transthyretin Amyloidosis, and Their Common Age-Related Comorbidities

Christopher L. Cioffi,* Arun Raja, Parthasarathy Muthuraman, Aravindan Jayaraman, Srinivasan Jayakumar, Andras Varadi, Boglarka Racz, and Konstantin Petrukhin*

Cite This: *J. Med. Chem.* 2021, 64, 9010−9041

Read Online

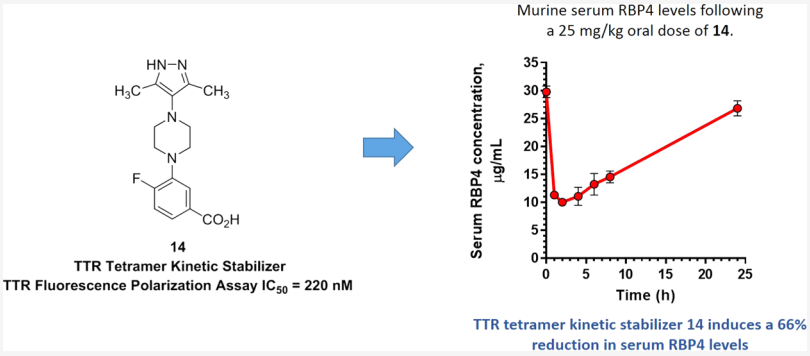

TTR tetramer kinetic stabilizer 14 induces a 66% reduction in serum RBP4 levels

ABSTRACT: Dissociation of transthyretin (TTR) tetramers may lead to misfolding and aggregation of proamyloidogenic monomers, which underlies TTR amyloidosis (ATTR) pathophysiology. ATTR is a progressive disease resulting from the deposition of toxic fibrils in tissues that predominantly presents clinically as amyloid cardiomyopathy and peripheral polyneuropathy. Ligands that bind to and kinetically stabilize TTR tetramers prohibit their dissociation and may prevent ATTR onset. Drawing from clinically investigated AG10, we designed a constrained congener (**14**) that exhibits excellent TTR tetramer binding potency, prevents TTR aggregation in a gel-based assay, and possesses desirable pharmacokinetics in mice. Additionally, **14** significantly lowers murine serum retinol binding protein 4 (RBP4) levels despite a lack of binding at that protein's all-*trans*-retinol site. We hypothesize that kinetic stabilization of TTR tetramers *via* **14** is allosterically hindering all-*trans*-retinol-dependent RBP4−TTR tertiary complex formation and that the compound could present ancillary therapeutic utility for indications treated with RBP4 antagonists, such as macular degeneration.

■ INTRODUCTION

In recent years, the circulating RBP4−TTR−all-*trans*-retinol transport complex has become a target for pharmacological intervention in ophthalmic diseases associated with enhanced accumulation of cytotoxic lipofuscin bisretinoids in the retina. Transport of all-*trans*-retinol (vitamin A, **1**) (Figure 1) from the liver to tissues, including the retina, involves a transport complex composed of retinol binding protein 4 (RBP4) and transthyretin (TTR, thyroxine binding prealbumin).[1,2] Reports indicate that prevention of ternary complex formation between all-*trans*-retinol, RBP4, and TTR can be achieved *via* selective antagonists that compete with all-*trans*-retinol for binding at RBP4.[3−7] Prevention of holo-RBP4 (all-*trans*-retinol bound to RBP4) formation precludes complexation with TTR and subsequently leads to a lowering of serum RBP4 levels facilitated by rapid glomerular filtration of the protein due to its relatively low molecular weight (21 kDa).[2] Evidence suggests that pharmacological reduction of serum RBP4 levels induces a concomitant reduction in circulating all-*trans*-retinol that impedes ocular influx of the critical retinoid, resulting in a cessation of cytotoxic lipofuscin bisretinoid accumulation in the retina.[8,9] This approach to modulate retinal lipofuscin bisretinoid production is hypothesized to slow the progression of geographic atrophy in

Received: January 19, 2021
Published: June 17, 2021

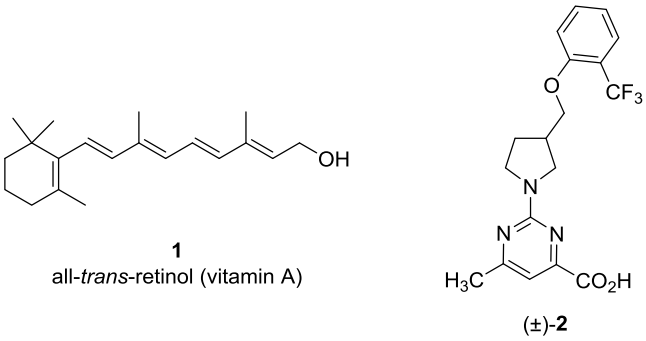

Figure 1. All-*trans*-retinol (vitamin A) (**1**) and bispecific RBP4 antagonist−TTR tetramer kinetic stabilizer (±)-**2**.

dry age-related macular degeneration (AMD) and Stargardt disease patients. We have shown that potent and selective RBP4 antagonists disrupt holo-RBP4−TTR ternary complex formation *in vitro* and significantly reduce serum RBP4 levels *in vivo* in rodents and nonhuman primates.[4−7,10,11] Furthermore, chronic oral administration of RBP4 antagonists in *Abca4*$^{-/-}$ knockout mice, a model of excessive lipofuscinogenesis that recapitulates the Stargardt disease phenotype, led to a reduction in retinal cytotoxic bisretinoid accumulation with an ancillary stabilization of complement system protein expression in the retinal pigment epithelium (RPE).[9,10] Additional dosing studies in wild-type (WT) BALB/cJ mice revealed that RBP4 antagonist-induced reductions in circulating RBP4 levels correlated with partial reductions in bisretinoid precursor concentrations without disruption of visual cycle kinetics.[10]

To date, only selective all-*trans*-retinol-competitive antagonists of RBP4 have been reported to block the formation of a ternary complex with TTR and lead to a reduction in circulating RBP4 levels *in vivo*. While selective RBP4 antagonists can be a safe and effective bisretinoid-lowering therapy for a majority of dry AMD and Stargardt disease patients, this class of compounds may potentially be counterindicated for a fraction of macular degeneration patients who are predisposed to diseases associated with TTR aggregation,[12−16] such as senile systemic amyloidosis (SSA).[17−19] Selective RBP4 antagonists would release unliganded TTR tetramer from the circulating holo-RBP4−TTR transport complex. This outcome may have serious implications as it has been previously suggested that in addition to transporting all-*trans*-retinol, the holo-RBP4−TTR complex may also serve to stabilize circulating TTR tetramers, as approximately 50% of TTR in circulation is bound to holo-RBP4.[20,21] Thus, the release of a significant pool of unliganded TTR tetramer induced by selective RBP4 antagonists may facilitate TTR amyloid fibril formation in susceptible individuals promoting TTR amyloidosis (ATTR)-related diseases. In an effort to address this potential liability, we recently identified and disclosed a series of potent RBP4 antagonists that also exhibit TTR tetramer kinetic stabilization activity. A standout analogue of this novel class of bispecific ligands, (±)-**2**, exhibited a favorable balance of *in vitro* RBP4 potency (RBP4 scintillation proximity assay (SPA) half-maximal inhibitory concentration (IC_{50}) = 80 nM and homogeneous time-resolved fluorescence (HTRF-fluorescence resonance energy transfer (FRET)) assay IC_{50} = 0.250 μM) and TTR potency (TTR fluorescence polarization (FP) assay IC_{50} = 2.85 μM), which was found to induce a robust and sustained lowering of serum RBP4 levels (>80%) upon oral dosing in mice and was also capable of decreasing the formation of high-molecular-weight TTR aggregates in an *in vitro* gel-based TTR aggregation assay.[7] These data suggest that (±)-**2** and its related analogues might hold promise as orally bioavailable therapeutics for the treatment of dry AMD and Stargardt disease that may also prevent potential ATTR comorbidities such as SSA in susceptible patients.

Concurrent with our recently reported bispecific RBP4 antagonist−TTR tetramer kinetic stabilizer work, we also conducted a medicinal chemistry campaign that focused on the identification of novel, potent, and selective TTR tetramer kinetic stabilizers for the treatment of ATTR-related diseases. During the course of this ancillary drug discovery campaign, we sought to determine whether our newly designed TTR tetramer stabilizers were also capable of inducing concomitant reductions in serum RBP4 levels by potentially antagonizing the formation of the holo-RBP4−TTR complex.

TTR Tetramer Kinetic Stabilizers. TTR is a 55 kDa homotetramer composed of four β-sheet-rich, 127-residue polypeptide monomers that is largely synthesized in the liver for secretion into the blood.[22] TTR tetramers possess two high-affinity binding sites for the thyroid hormone thyroxine (T4, **3**) (Figure 2). However, less than 1% of circulating TTR carries T4,

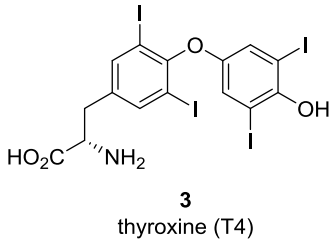

Figure 2. Thyroid hormone thyroxine (T4) (**3**).

while another serum protein, thyroxine binding globulin (TBG), functions as its primary transporter in the blood.[22] While TTR is not a primary carrier of T4 in the serum, it serves as the major transport protein for thyroxine in the central nervous system (CNS), where choroid plexus-derived TTR delivers T4 from the cerebrospinal fluid (CSF) to the choroid plexus and the brain.[23] Accumulating evidence suggests that TTR may play an auxiliary role in sequestering β-amyloid (Aβ) peptides within the CSF by promoting their clearance from the CNS to the periphery, potentially providing neuroprotective effects against Alzheimer's disease.[24,25]

The quaternary structure of TTR is of a homotetramer principally formed between two dimers.[22] Formation of the structure begins with the association of two identical 127-residue β-sheet-rich polypeptide monomers that contain a total of eight antiparallel β-strands (denoted as β-strands A−H), with β-strand E presenting a short α-helix located at its terminus. The monomers associate *via* their edge β-strands (H-bond interactions involving the two edge β-strands H and F) yielding a dimer subunit, which further associates with a second dimer subunit in a back-to-back arrangement. The resulting dimer of dimer bears a large solvent channel, which passes between the two sheets and presents two identical C_2-symmetric binding sites for T4.[22] The TTR dimer−dimer interface is relatively weak and its dissociation is the rate-limiting step in the overall TTR tetramer dissociation process.[26] The free dimer subunits may subsequently further dissociate into monomers that could potentially proceed to misfold and oligomerize. Oligomerization

https://doi.org/10.1021/acs.jmedchem.1c00099
J. Med. Chem. 2021, 64, 9010−9041

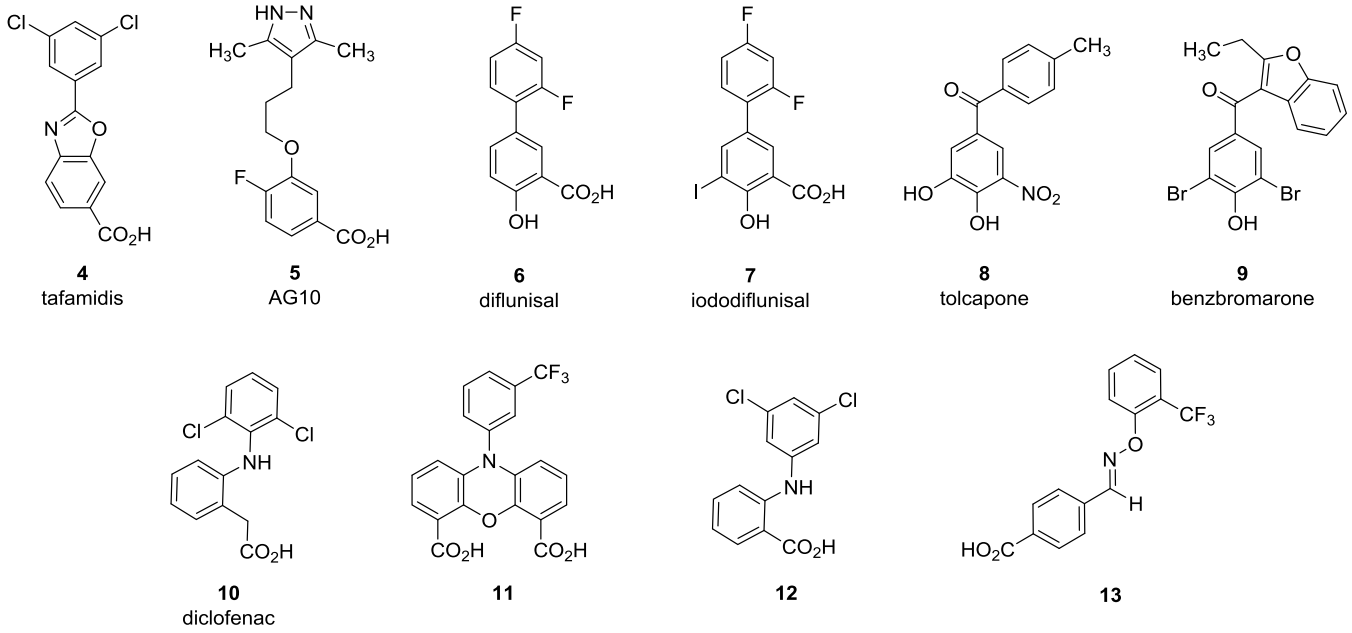

Figure 3. Representative examples of various reported TTR tetramer stabilizer structural classes that bind at the T4 binding site. This sample set of TTR tetramer stabilizers include tafamidis (**4**),[35] AG10 (**5**),[43] diflunisal (**6**),[47] iododiflunisal (**7**),[49] tolcapone (**8**),[48] benzbromarone (**9**), diclofenac (**10**),[50] *N*-phenyl phenoxazine (**11**),[5151] dibenzofuran (**12**),[52] and bis-aryloxime ether (**13**).[53] The following compounds highlighted in the figure above are registered drugs for various indications: tafamidis (vyndaqel and vyndamax, **4**) for treating ATTR-PN, diflunisal (dolobid, **6**), an NSAID also used for ATTR, tolcapone (tasmar, **8**), a COMT inhibitor for treating Parkinson's disease, benzbromarone (**9**), a uricosuric agent and noncompetitive inhibitor of xanthine oxidase previously shown by us to act as a potent TTR ligand,[7,54,55] and diclofenac (voltaren, **10**), an NSAID to treat pain, inflammatory disorders, and dysmenorrhea.

can eventually lead to aggregation and formation of toxic amyloid fibrils, which underlies the pathophysiology of ATTR.[26]

Autosomal-dominant ATTR is a rare and progressive disease that involves severe organ damage due to the extracellular deposition of the aforementioned toxic TTR amyloid fibrils in tissues. The disease typically presents clinically as either TTR amyloid cardiomyopathy (ATTR-CM; can lead to arrhythmias, arterial fibrillation, and biventricular heart failure)[27,28] or peripheral polyneuropathy (ATTR-PN; can cause loss of sensation, tingling, numbness, or pain as well as damage to the autonomic nervous system)[29] and can arise from propathogenic monomers with inherited TTR mutations. Nonhereditary ATTR may emerge from wild-type TTR (WT-TTR) monomer misfolding in older individuals.[30] There are at least 77 TTR mutations associated with familial ATTR diseases, and these variants influence amyloidogenicity by either (1) reducing the thermodynamic stability of the TTR tetramer (*i.e.*, the monomers are less likely to associate into a TTR tetramer and are more likely to misfold into an amyloidogenic intermediate), (2) reducing the kinetic barrier for tetramer dissociation (the TTR tetramer with the variant dissociates at a faster rate than WT-TTR with a concomitant increase in monomer aggregation rate), or (3) both thermodynamically and kinetically destabilizing the TTR tetramer.[12] The kinetically stable but thermodynamically destabilized variant V30M[13] is predominantly associated with late-onset familial amyloid polyneuropathy (FAP) and is strongly pathogenic. The most common amyloidogenic TTR variant, V122I,[14] presents at a relatively high frequency within the African-American population (approximately 3.4%) and is predominantly associated with familial amyloid cardiomyopathy (FAC). Its pathogenicity is attributed to its ability to kinetically destabilize the TTR tetramer and induce a dissociation rate that is approximately 2-fold faster than WT-TTR.[31] The L55P mutation both thermodynamically and kinetically destabilizes tetramer formation and can aggressively promote early-onset ATTR-CM and ATTR-PN.[16] Conversely, compound heterozygotes carrying a proamyloidogenic TTR mutation (*e.g.*, V30M) and a disease-suppressing mutation that hyperstabilizes TTR tetramers, such as T119M or R104H,[32] are reported to either develop a mild late-onset pathology or be completely protected against ATTR. The T119M variant kinetically stabilizes the TTR tetramer, whereas the R104H variant provides thermodynamic stability to the quaternary structure. This difference in mechanism of stabilization is crucial as the T119M variant is resistant to tetramer dissociation and aggregation and provides a greater level of protection against TTR aggregation *in vitro* relative to R104H. Finally, WT-TTR misfolding and aggregation that occur nongenetically with age are associated with SSA, a late-onset and prevalent form of ATTR that is estimated to affect 10−20% of individuals aged 80 years and older.[19]

Currently available Food and Drug Administration (FDA)-approved approaches for treating ATTR-CM and ATTR-PN include two treatments that reduce circulating TTR levels (the antisense oligonucleotide inotersen[33] and the small interfering RNA (siRNA) patisiran[34]) and the small molecule tafamidis (vyndaqel and vyndamax, **4**)[35−40] (Figure 3) that binds to and stabilizes circulating TTR tetramers. Ligand binding at the T4 sites has been shown to kinetically stabilize TTR tetramers by increasing the dissociative energy barrier of the native tetrameric state. Due to the presence of two additional T4 transport proteins (TGB and albumin), the majority of TTR in circulation is not bound to TTR. Thus, drug discovery approaches to identify T4-competitive small molecules capable of kinetically stabilizing TTR tetramers have garnered significant interest as a therapeutic option for treating ATTR. Numerous structurally

https://doi.org/10.1021/acs.jmedchem.1c00099
J. Med. Chem. 2021, 64, 9010−9041

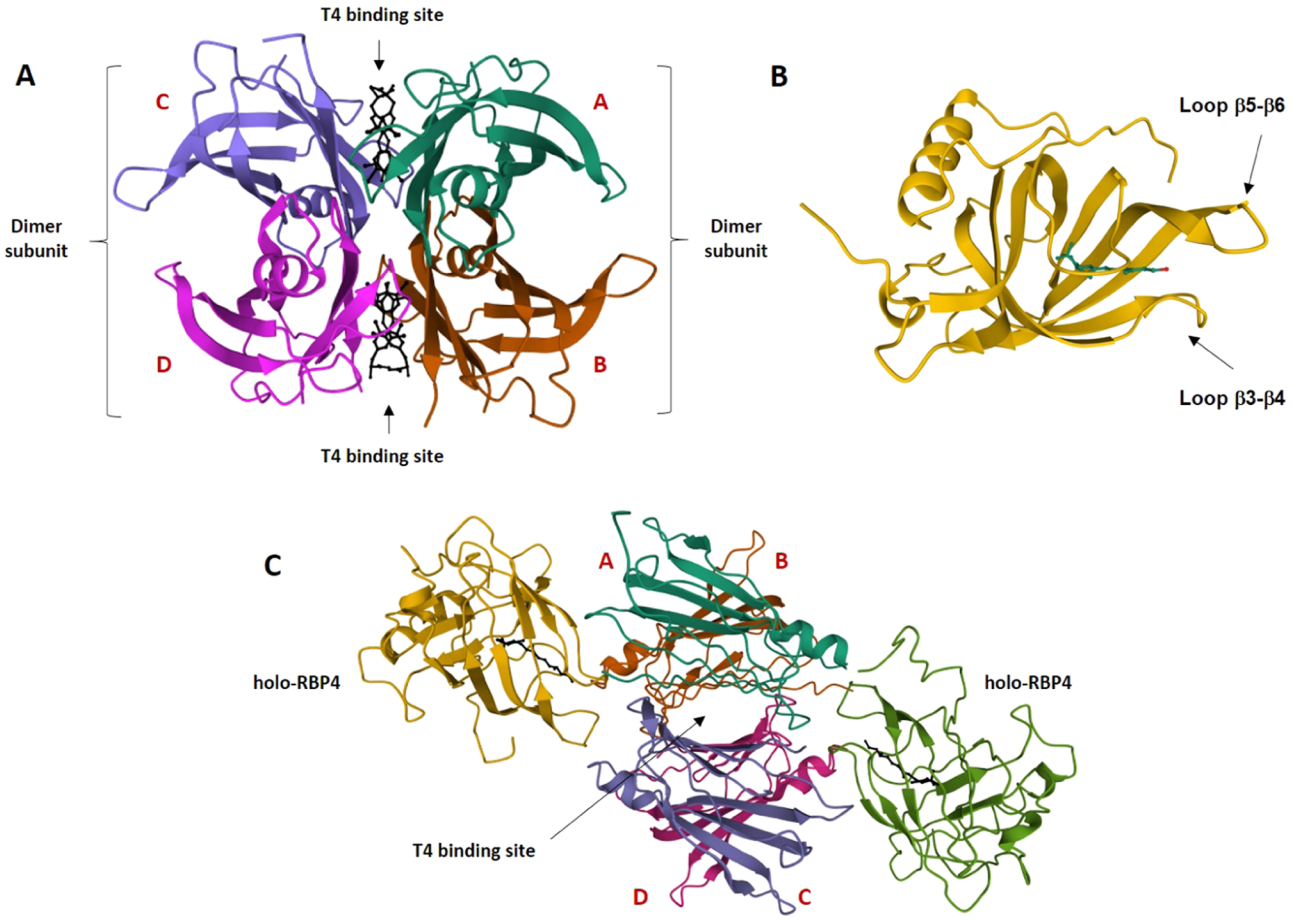

Figure 4. Quaternary structures of TTR with T4-bound, holo-RBP4, and the holo-RBP4−TTR ternary complexes. (A) Ribbon diagram of the quaternary homotetrameric structure of TTR with T4 (3) bound within its respective binding site (PDB: 2ROX).[59] The two dimer subunits are each composed of two individual monomers (labeled A (blue-green), B (orange), C (light blue), and D (pink)). The dimers are associated back-to-back and present two C_2 symmetrical T4 binding sites running through the center of the protein. The binding of T4 is shown in a ball and stick format (black). (B) Ribbon diagram of holo-RBP4 (PDB: 1RBP). Holo-RBP4 is shown as yellow and all-*trans*-retinol is depicted in a ball and stick format (black). (C) The holo-RBP4−TTR complex (PDB: 1QAB) colored by chain and viewed from the front. The TTR tetramer is located at the center of the complex with two holo-RBP4 molecules (one holo-RBP4 molecule is shown as yellow and the other as light green) docked at a twofold axis of symmetry that is perpendicular to the T4 binding sites. All-*trans*-retinol is depicted in a ball and stick format (black), which is encapsulated by the complex and its binding site is blocked. The T4 binding site is not occluded.

diverse scaffolds in addition to tafamidis have been reported to bind at the T4 site and stabilize TTR tetramers, and representatives of this class are highlighted in Figure 3. The two most advanced small molecule TTR tetramer stabilizers to date include the aforementioned FDA-approved tafamidis and clinically investigated AG10 (acoramidis, **5**).[41−43] Tafamidis has been approved for the treatment of FAP and ATTR-CM. A phase III study with 441 ATTR-CM patients showed that administration of the drug reduced the risk of death by 30% and the rate of cardiovascular-related hospitalizations by 32% compared to placebo controls.[44] TTR stabilizer AG10 was reported to be well tolerated and demonstrated near-complete stabilization of TTR in a 28 day phase II proof-of-concept trial with ATTR-CM patients presenting symptomatic chronic heart failure.[45] Approximately 30% of patients with hereditary ATTR do not respond to tafamidis,[46] indicating a need for exploring additional classes of TTR tetramer stabilizers. Phase III clinical trials with AG10 for the treatment of ATTR-CM and ATTR-PN are currently ongoing. In addition, the repurposed FDA-approved nonsteroidal anti-inflammatory drugs (NSAIDs) diflunisal (dolobid, **6**)[47] and catechol-*O*-methyl transferase (COMT) inhibitor tolcapone (tasmar, **8**)[48] are also reported to exhibit TTR tetramer stabilization activity and have been investigated for clinical efficacy against ATTR-PN.

Nature of the Holo-RBP4−TTR Protein−Protein Interaction (PPI). RBP4 is a single domain protein that contains an N-terminal coil, eight antiparallel β-strands (denoted as β-strands A−H), and a short α-helix within close proximity to the C-terminus.[56] The all-*trans*-retinol binding cavity resides within the core of the protein and consists of an eight-stranded up-and-down β-barrel. Formation of the aforementioned transport complex requires that all-*trans*-retinol be initially bound to its respective RBP4 binding cavity as apo-RBP4 poorly associates with TTR. The reported Protein Data Bank (PDB) high-resolution holo-RBP4−TTR complex X-ray crystal structures 1QAB[57] (RBP4−all-*trans*-retinol−TTR ternary complex) and 3BSZ[58] (RBP4−all-*trans*-retinol−TTR ternary complex bound to an anti-RBP Fab) show all-*trans*-retinol bound within its RBP4 binding cavity in a forward-facing pose (hand-in-glove-like fit) with its lipophilic β-ionone ring projecting into a vacuous hydrophobic and phenylalanine (Phe)-rich pocket located deep within the protein. The all-*trans*-retinol polyene chain traverses through a narrow β-barrel core region with the pendant terminal hydroxyl group projecting slightly out of the

https://doi.org/10.1021/acs.jmedchem.1c00099
J. Med. Chem. 2021, 64, 9010−9041

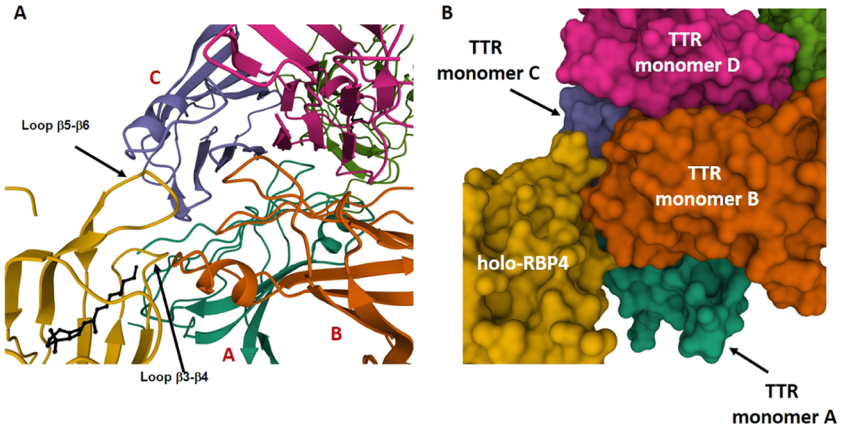

Figure 5. PPI interaction surfaces between holo-RBP4 and TTR. (A) Close-up view of the holo-RBP4−TTR PPI (PDB: 1QAB) colored by chain. Holo-RBP4 is shown as yellow and all-*trans*-retinol is depicted in a ball and stick format (black) and buried in the hydrophobic cavity of the RBP4 β-barrel. The alcohol moiety points toward the EF loop of TTR (subunit B) and engages in a H-bond interaction with Gly83. The TTR monomer subunits are labeled as A (blue-green), B (orange), C (light blue), and D (pink). The image shows how the loops $\beta3-\beta4$ and $\beta5-\beta6$ of holo-RBP4 provide a surface that fits into a crevice formed by the arrangement of three TTR subunits (A−C). (B) Molecular surface representation of holo-RBP4−TTR PPI that more clearly shows holo-RBP4 making contact with three TTR subunits (A−C) (PDB: 1QAB).

binding pocket and toward the solvent. These X-ray crystal structures show that the exterior RBP4 loops that surround the opening of the binding pocket (loops $\beta3-\beta4$ and $\beta5-\beta6$) present an interaction contact surface for docking with TTR.[58] Binding of all-*trans*-retinol to RBP4 induces conformational changes within these exterior loops that facilitate recognition of TTR, allowing holo-RBP4 to bind to TTR at a twofold axis of symmetry that is perpendicular to the T4 binding sites (Figure 4).[58] Furthermore, TTR features two equivalent sites for holo-RBP4 binding, providing a holo-RBP4 to TTR tetramer stoichiometry of 2:1. Finally, the structure of the holo-RBP4−TTR ternary complex fully encapsulates all-*trans*-retinol and conceals its binding site. However, the T4 binding sites are not occluded.[58]

Both holo-RBP4 and TTR each contribute 21 amino acids to their respective PPI interface domains, which are both largely hydrophobic at their cores and hydrophilic at their peripheries.[58] The TTR amino acids Val-20, Trp79, Leu82, Ile84, Pro113, and Tyr114 from subunits B and C form a hydrophobic patch, which strongly associates with the complementary RBP4 hydrophobic patch composed of residues Trp67, Leu63, Leu64, Val69, Phe96, and Leu97. The resulting PPI involves a holo-RBP4 molecule simultaneously interacting with three TTR subunits (A−C)[58] (Figure 5). Interacting hydrophilic residues from participating TTR subunit A are closer to the border of the contact surface of the protein. Four hydrogen bonds (H-bonds) between RBP4 and TTR subunit B also contribute to the PPI.[58] Notably, further stabilization of the complex is also achieved *via* a H-bond interaction between the hydroxyl group of all-*trans*-retinol and Gly83 of the TTR subunit B (EF loop).[58]

The mechanism of action for selective all-*trans*-retinol-competitive RBP4 antagonists has been attributed to the significant and unfavorable conformational changes they induce in loops $\beta3-\beta4$ and $\beta5-\beta6$ that preclude facile association with the TTR PPI domain.[60] We questioned whether ligands that bind at the T4 site of TTR could confer unfavorable changes to the protein's PPI domain and allosterically antagonize its ability to associate with holo-RBP4 and disrupt complex formation. Such ligands could potentially induce serum RBP4 and all-*trans*-retinol reductions, thereby presenting RBP4 antagonist pharmacological activity with significant TTR tetramer stabilization capability. Prior to the work reported herein, TTR has not been considered as a drug target for indications that may be treated *via* RBP4 antagonists, such as Stargardt disease and dry AMD. Thus, such drugs may potentially prevent the formation of amyloid fibrils in patients who, in addition to dry AMD and Stargardt disease, may also carry proamyloidogenic mutations in the TTR gene.

In our work reported herein, we initiated a structure-based drug design effort to identify a novel class of TTR tetramer kinetic stabilizers that would be assessed for their ability to both stabilize TTR tetramers *in vitro* and reduce circulating levels of RBP4 *in vivo*. We selected AG10 as a benchmark scaffold from which to develop a novel series of ligands as (1) the compound has been reported to effectively bind to and stabilize WT-TTR and the proamyloidogenic V122I-TTR variant and (2) the compound is also reported to be more potent and selective for stabilizing TTR tetramers in buffer and human serum than tafamidis, despite both compounds exhibiting similar TTR binding affinities (K_d for AG10 = 4.8 ± 1.9 nM; K_d for tafamidis = 4.4 ± 1.3 nM).[42,43] Our primary goals were to identify novel chemical matter capable of (1) retaining or improving the observed *in vitro* TTR tetramer binding potency observed for AG10, (2) exhibiting suitable pharmacokinetics (PK) properties to allow for adequate TTR tetramer stabilization and prevention of aggregation *in vivo* upon oral administration, and (3) presenting a favorable absorption distribution metabolism and excretion (ADME) profile and no limiting off-target pharmacology that would preclude drug development. In addition, recently published phase I human PK data for AG10 revealed that the major metabolic pathway for the compound involves acyl glucuronidation of its carboxylic acid.[61] Thus, we also sought to include analogues within our sample set that may potentially circumvent this metabolic pathway, which is generally reported to be associated with increased incidences of idiosyncratic toxicity.

We utilized the X-ray crystallographic data PDB 4HIQ[43] in our structure-based drug design efforts, which shows AG10 occupying both T4 binding sites of V122I-TTR tetramer (Figure 6A). AG10 was reported to bind to V122I-TTR with negative cooperativity (K_{d_1} = 4.8 nM, K_{d_2} = 314 nM).[43] The C_2 symmetrical T4 binding sites are subdivided into inner and outer

https://doi.org/10.1021/acs.jmedchem.1c00099
J. Med. Chem. 2021, 64, 9010−9041

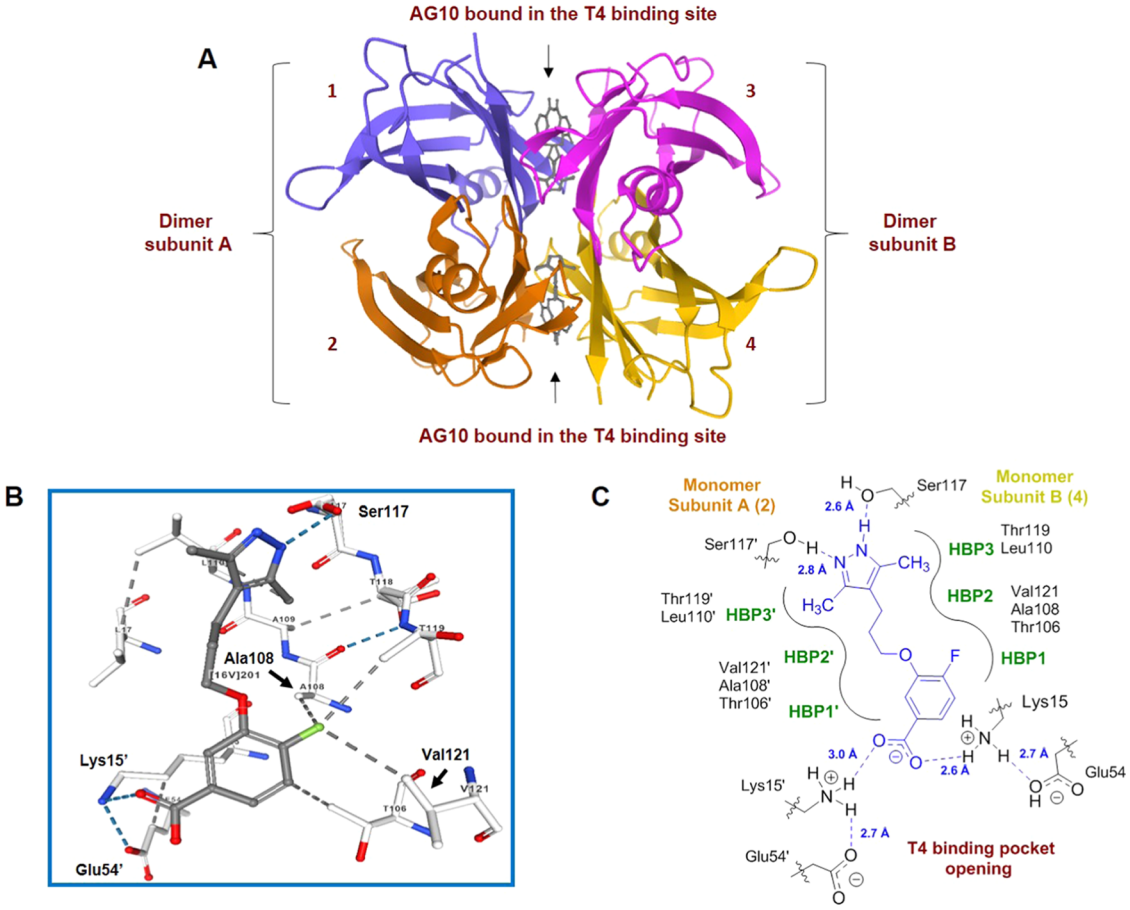

Figure 6. X-ray crystallographic structure showing AG10 (**5**) bound to V122I-TTR (PDB: 4HIQ). (A) Ribbon diagram of the quaternary homotetrameric structure of TTR with AG10 bound in the T4 binding sites with both symmetry-related binding conformations shown. The TTR dimers are shown as dimer subunits A and B, and each monomer subunit of the tetramer (labeled 1−4) is shown with its secondary structural elements and colored differently. The monomer components of dimer A are shown in cyan (monomer 1) and orange (monomer 2). The monomer components of dimer B are shown in pink (monomer 3) and yellow (monomer 4). The dimers are associated back-to-back creating a large channel through the center of the tetramer that presents two C_2 symmetrical T4 binding sites. AG10 is shown in stick format (gray). (B) TTR tetramer kinetic stabilizer AG10 is shown in a ball and stick format (dark gray), with contacting residues labeled and illustrated in stick format (white). The binding pose of AG10 (**5**) positions the benzoic acid motif bent out of the plane with the rest of the molecule in a nearly orthogonal orientation. (C) Ligand interaction diagram of AG10 (shown as blue) derived from PDB 4HIQ, which features the HBPs with their associated localized amino acids. The diagram further illustrates key binding interactions observed in the X-ray crystallographic data, including pivotal H-bonds and salt-bridge interactions. The pyrazole head group of AG10 projects deep within the inner binding cavity of the T4 binding pocket where it engages in two H-bond interactions with Ser117 and Ser117′. The pyrazole 3,5-dimethyl groups of AG10 occupy HBP3 and HBP3′. The aliphatic chain of AG10 comes in contact with the residues lining HBP2/HBP2′. The fluorine atom of AG10 projects into a hydrophobic region of HBP1 in the outer T4 binding cavity. The carboxylic acid of AG10 is sandwiched between Lys15 and Lys15′. The H-bond interactions are depicted as blue dashed lines, with the atomic distances labeled in angstrom.

binding cavities containing three pairs of halogen binding pockets (HBP1, HBP1′, HBP2, HBP2′, HBP3, and HBP3′) that the iodine atoms of thyroxine occupy. Within the innermost region of the T4 binding cavity, residues Ser117 and Ser117′ engage in bridging H-bond interactions with a resident structural water molecule. These residues are within close proximity to the T4 inner binding cavity HBP3 and HBP3′ pockets. The lipophilic HBP2 and HBP2′ pockets are located between the inner and outer binding cavities, and the HBP1 and HBP1′ pockets are housed near the outer region of the binding cavity. The ionizable residues Lys15/Lys15′ and Glu54/Glu54′ reside near the periphery of the T4 binding site opening.

The occupancy of AG10 within the T4 site involves a forward binding mode, with the 3,5-dimethyl-1*H*-pyrazole group projecting deep within the inner cavity where it engages in two H-bond interactions with Ser117 and Ser117′ (Figure 6B,C).[42,43] The two pyrazole methyl groups occupy the neighboring HBP3 and HBP3′ pockets, and the *n*-propyloxy linker resides within the center of the binding site channel where it makes van der Waals contacts with the residues lining HBP2 and HBP2′. The fluorine atom of the benzoic acid fragment projects toward the lipophilic HBP1 pocket (Figure 6B,C),[42,43] while the carboxylic acid is positioned in close proximity to the opening of the T4 binding site where it is sandwiched between the two symmetry-related ε-amino groups of Lys15 and Lys15′. The interactions between the carboxylic acid of AG10 and Lys15/Lys15′ induce partial closure of the T4 binding site opening and effectively shield the compound from the solvent.[42,43]

The reported isothermal titration calorimetry (ITC) thermograms for tafamidis and AG10 show that although both compounds present similar changes in Gibbs free energy of binding (ΔG, where $\Delta G = \Delta H - T\Delta S$) ($\Delta G$ for AG10 = −11.34 kcal/mol; ΔG for tafamidis = −11.34 kcal/mol), the compounds

https://doi.org/10.1021/acs.jmedchem.1c00099
J. Med. Chem. 2021, 64, 9010−9041

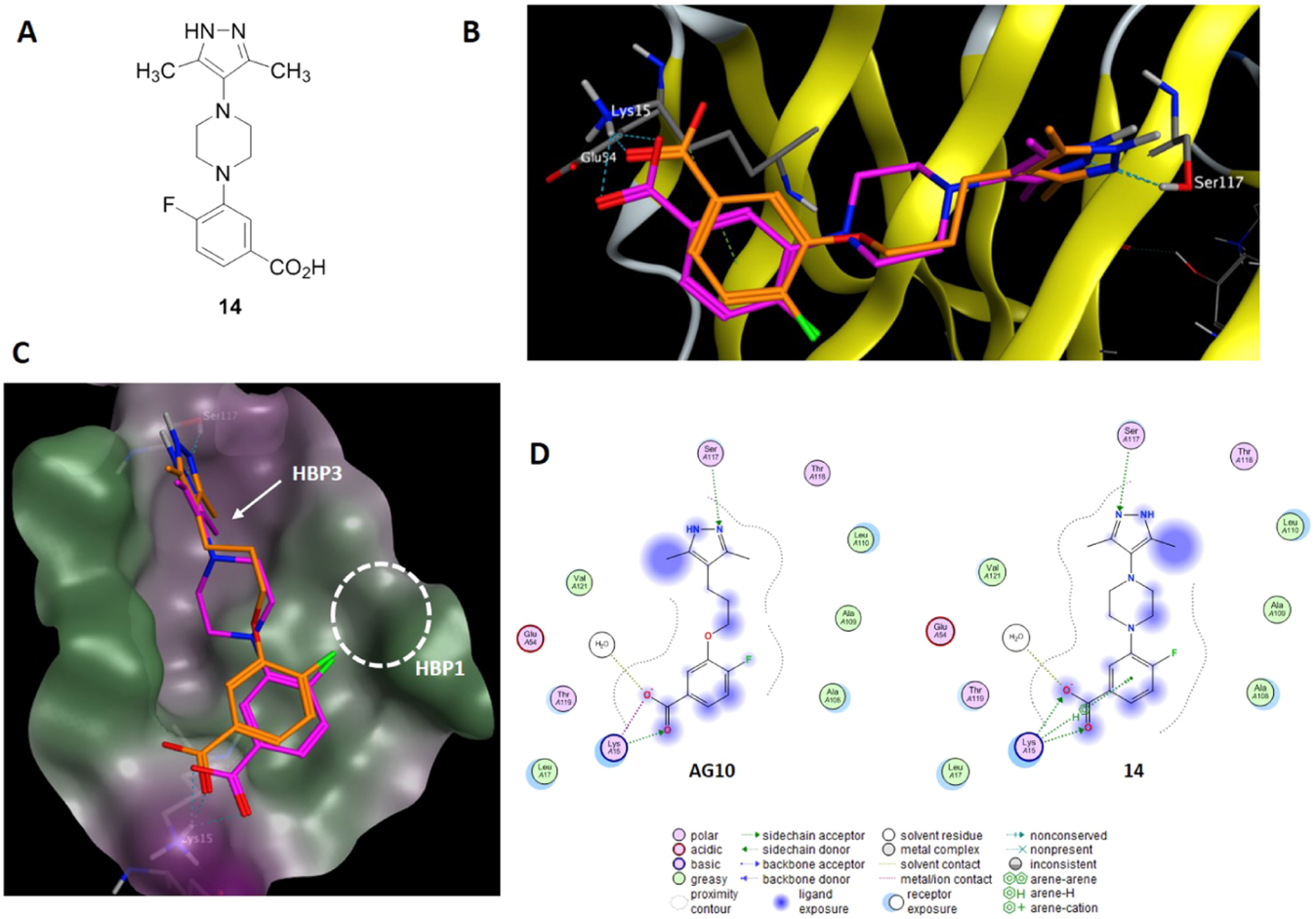

Figure 7. Putative binding mode of piperazine compound **14** within the T4 binding site. (A) Proposed TTR tetramer kinetic stabilizer **14**, which contains a piperazine core. (B) Overlay of docked poses of piperazine **14** (magenta) and AG10 (orange) within the TTR T4 binding cavity using PDB 4HIQ (obtained from the Protein Data Bank); contacting residues are labeled and illustrated in stick format; H-bond interactions are depicted as blue dashed lines. (C) Molecular surface with the overlay of docked poses of piperazine **14** (magenta) and AG10 (orange) within the TTR T4 binding cavity using PDB 4HIQ. The protein surface is colored by hydrophobicity (green) and hydrophilicity (purple) using contact preferences; contacting residues are labeled and illustrated in stick format; H-bond interactions are depicted as blue dashed lines. (D) Legend for the ligand interaction diagrams in the binding pose using MOE. (MOE) 2020.09 (Chemical Computing Group, Inc., Montreal, Quebec, Canada, http://www.chemcomp.com).

differed significantly with regard to their relative enthalpic and entropic contributions.[42,43] The binding of AG10 was found to be largely enthalpically driven ($\Delta H = -13.60$ kcal/mol and $T\Delta S = -2.26$ kcal/mol), while tafamidis demonstrated equal enthalpic and entropic contributions to binding ($\Delta H = -5.00$ kcal/mol and $T\Delta S = 6.39$ kcal/mol). The larger enthalpic contribution for AG10 is attributed to the H-bond interactions between its pyrazole head group and Ser117 and Ser117′, which are not present for tafamidis. Importantly, these additional H-bond interactions of AG10 with Ser117 and Ser117′ appear to mimic the direct H-bond interaction observed between these two residues in the T119M-TTR disease-suppressing variant.[42,43] The Ser117 and Ser117′ residues of T119M-TTR are within close proximity (~2.8 Å) to form an intramolecular H-bond interaction between them. This pivotal H-bond interaction helps to draw the dimer subunits closer and fortifies the aggregate molecular interactions between them. This is hypothesized to significantly increase in the T119M-TTR dimer−dimer dissociation energy barrier, thus providing superior kinetic stabilization relative to WT-TTR quaternary structure, which does not contain this key Ser117/Ser117′ H-bond interaction. Indeed, the T119M variant displays a 40-fold slower dissociation rate relative to WT-TTR. Thus, the ability of AG10 to mimic this critical Ser117/Ser117′ binding interaction of T119-TTR may explain why it demonstrates superior potency to tafamidis with regard to stabilizing TTR tetramers in buffer and human serum despite exhibiting a similar binding affinity.[42,43]

Our medicinal chemistry strategy utilized the X-ray crystallographic data of PDB 4HIQ to construct a computational docking model that would assist with the design of novel scaffolds with the goal of (1) maintaining the pivotal H-bond interactions with Ser117/Ser117′ and key van der Waals interactions observed for AG10 and (2) potentially improving entropic contributions to binding by reducing the number of rotatable bonds and conformational flexibility presented by AG10. The model was generated with Molecular Operating Environment (MOE) 2020.09 (Chemical Computing Group, Inc., Montreal, Quebec, Canada, http://www.chemcomp.com) and utilized the protein structure preparation tool followed by Protonate3D, as implemented in MOE. Our initial docking analysis involved piperazine analogue **14** (Figure 7A), a novel and conformationally constrained congener of AG10, and the data generated was primarily used to determine whether the

https://doi.org/10.1021/acs.jmedchem.1c00099
J. Med. Chem. 2021, 64, 9010−9041

SAR Approach Toward Novel TTR Tetramer Kinetic Stabilizers Derived From Benchmark AG10 (5)

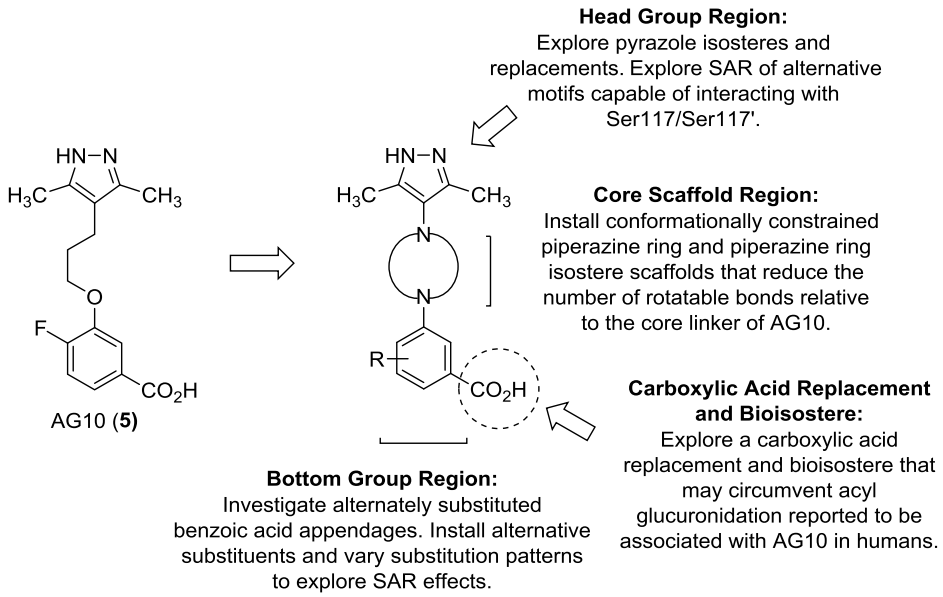

Figure 8. Medicinal chemistry work plan for the identification of novel and conformationally constrained TTR tetramer kinetic stabilizers.

proposed compound was predicted to have good docking orientations by positioning it within the T4 binding cavity relative to AG10. The docking model images shown in Figure 7 present AG10 and **14** bound with one-half of the C_2-symmetric T4 binding site removed to visualize the binding poses and interactions for the compounds. The model predicted that **14** would exhibit good convergence with AG10 in the T4 binding site, as evidenced in the observed calculated root-mean-square deviation (RMSD) value of 1.7 Å. Figure 7B,C shows compound **14** presenting a similar binding pose as AG10 in the T4 site, with both compounds exhibiting a forward binding mode projecting their respective 3,5-dimethyl-1*H*-pyrazole head groups into the inner binding cavity and oriented orthogonally. The 3,5-dimethyl-1*H*-pyrazole of **14** is proposed to reside within the inner T4 binding cavity, where it is predicted to engage in a H-bond interaction with Ser117 and van der Waals interactions between its methyl group and HBP3 in a similar manner to AG10. Our docking model also predicts that the piperazine ring serves as a suitable replacement for the *n*-propyloxy linker, as it is shown to effectively place the 3,5-dimethyl-1*H*-pyrazole head group within the T4 inner binding cavity while also presenting the benzoic acid in an optimal position to engage in electrostatic interactions with Lys15 and Lys15′ residing near the opening of the binding site. Finally, our model also shows the fluorine atom of **14** positioned to occupy HBP1 in a similar manner to the AG10 aryl fluoride (Figure 7C).

As outlined in Figure 8, our medicinal chemistry plan focused on exploring the aforementioned computational docking results as we conducted structure−activity relationship (SAR) campaigns that focused on three key regions of lead AG10 and piperazine **14**. This included exploring the SAR of (1) alternative conformationally constrained cyclic core linkers, (2) isosteres and replacements for the 3,5-dimethyl-1*H*-pyrazole "head group region", and (3) variation of substituents and substitution patterns on benzoic acid "bottom-group region" appendage. Based on our docking model, we designed and synthesized illustrative examples of constrained analogues of AG10 that initially incorporated a piperazine linker and later included fused bicyclic and spirocyclic piperazine ring isosteres. We subsequently investigated the SAR of a series of analogues that featured a 3,5-dimethyl-1*H*-pyrazole head group with a piperazine core linker while presenting differing benzoic acid substituents. Previously reported SAR campaigns for AG10 suggest that positioning the carboxylic acid meta to its *n*-propyloxy linker was optimal for electrostatic binding interactions with the Lys15 and Lys15′ residues residing near the periphery of the T4 binding site opening. Thus, we fixed the carboxylic acid at the same position for our series of analogues while exploring alternative substituents and substitution patterns to the fluorine of AG10. We also explored the SAR of a small set of isosteres and replacements for the 3,5-dimethyl-1*H*-pyrazole head group of AG10, which projects deep into the T4 binding site and engages in H-bond interactions with Ser117 and Ser117′. Finally, we investigated the SAR effects of a carboxylic acid replacement and bioisostere that could mitigate or circumvent potential undesirable acyl glucuronidation metabolism.

■ CHEMISTRY

The synthetic route for a series of substituted 3-(4-(3,5-dimethyl-1*H*-pyrazol-4-yl)piperazin-1-yl)benzoic acid analogues (**14**, **20a−i**), highlighted in Scheme 1, begins with a palladium(0)-catalyzed amination between *tert*-butyl piperazine-1-carboxylate (**15**) and a corresponding substituted methyl bromobenzoate. The resulting aryl amines (**16a−j**) were *N*-Boc-deprotected with trifluoroacetic acid (TFA) in dichloromethane (CH_2Cl_2) at 0 °C, yielding **17a−j**. Amines **17a−j** were subsequently alkylated with 3-chloropentane-2,4-dione to give dione intermediates **18b−j** *in situ*, which then underwent condensation with hydrazine hydrate ($N_2H_4{\cdot}H_2O$) to provide the respective dimethyl pyrazoles **19a−j** in one pot (the exception to this sequence was dione **18a**, which was isolated). The methyl esters of **19a−j** were hydrolyzed with anhydrous lithium hydroxide (LiOH), and the lithium carboxylate salts were carefully neutralized with 2 N aqueous hydrochloric acid

https://doi.org/10.1021/acs.jmedchem.1c00099
J. Med. Chem. 2021, 64, 9010−9041

Scheme 1

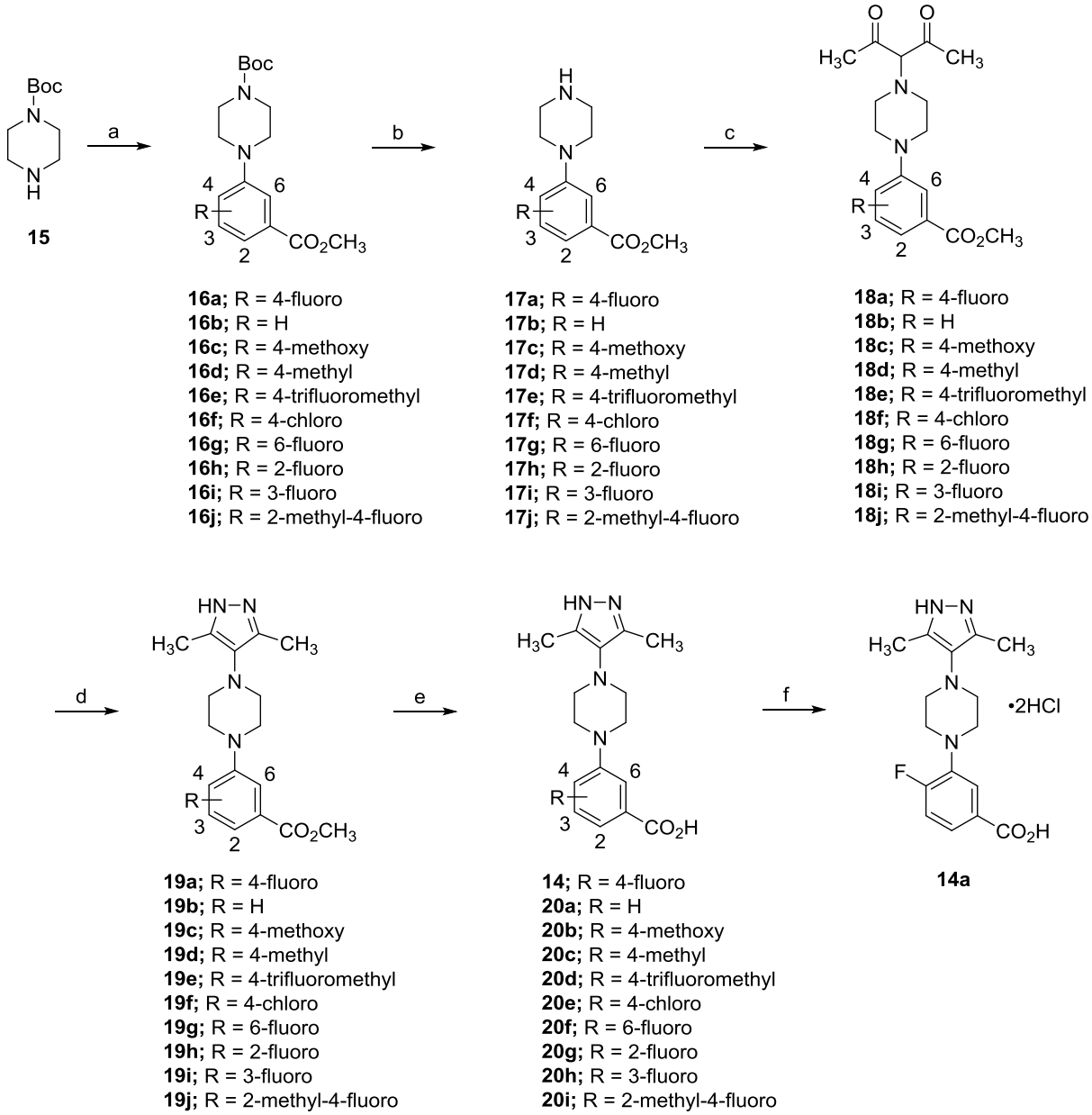

[a]Reagents and conditions: (a) substituted methyl bromobenzoate, 2-dicyclohexylphosphino-2′,4′,6′-triisopropylbiphenyl (X-Phos), Tris-(dibenzylideneacetone)dipalladium(0)-chloroform adduct ($Pd_2(dba)_3{\cdot}CHCl_3$), cesium carbonate (Cs_2CO_3), 1,4-dioxane, stirred at reflux for 16 h under an atmosphere of N_2 or heated in a sealed vessel at 110 °C, 16 h; (b) TFA, CH_2Cl_2, 0 °C to room temperature (rt), 3 h; (c) 3-chloropentane-2,4-dione, *N*,*N*-diisopropylethylamine (*i*-Pr_2NEt), tetrahydrofuran (THF), 0 °C to rt, 16 h; (d) $N_2H_4{\cdot}H_2O$ (64−65% in H_2O), THF, rt, 1 h; (e) (i) anhydrous LiOH, CH_3OH, THF, H_2O, rt, 3 h; (ii) 2 N aqueous HCl; (f) 2 N HCl in Et_2O, 0 °C to rt, 3 h.

(HCl) to yield the desired carboxylic acids **14** and **20a−i**. Compound **14** was subsequently converted to the bis-hydrochloride salt **14a** *via* treatment with a solution of 2 N HCl in diethyl ether (Et_2O).

The iodo analogue of **14** (**26**) was prepared *via* the route depicted in Scheme 2. The synthesis begins with a nucleophilic substitution reaction (S_NAr) displacement between methyl 3-fluoro-4-nitrobenzoate and **15**, proving intermediate **21**. Aryl nitro compound **21** was readily hydrogenated to the corresponding aniline **22**, which was subsequently converted to the aryl iodide *via* a Sandmeyer reaction involving 0.25 N aqueous sulfuric acid (H_2SO_4), H_2O, and potassium iodide (KI). The Sandmeyer reaction conditions served to produce the desired conversion to the aryl iodide as well as induce removal of the Boc group in one pot, affording **23** directly from **22**. Construction of the 3,5-dimethyl-1*H*-pyrazole head group was conducted in the same manner outlined in Scheme 1. The desired iodo-substituted benzoic acid **26** was achieved upon hydrolysis of ethyl ester **25** and neutralization of the resulting lithium carboxylate salt with 2 N aqueous HCl.

Fused bicyclic and spirocyclic piperazine ring isostere analogues of **14** (**32**, (±)-**38**, and **44**) were prepared and their corresponding syntheses are shown in Scheme 3. The preparation of each analogue of this sample set began with a palladium(0)-catalyzed amination between the corresponding *N*-Boc-protected piperazine ring isostere (*tert*-butyl (3a*R*,6a*S*)-

https://doi.org/10.1021/acs.jmedchem.1c00099
J. Med. Chem. 2021, 64, 9010−9041

Scheme 2

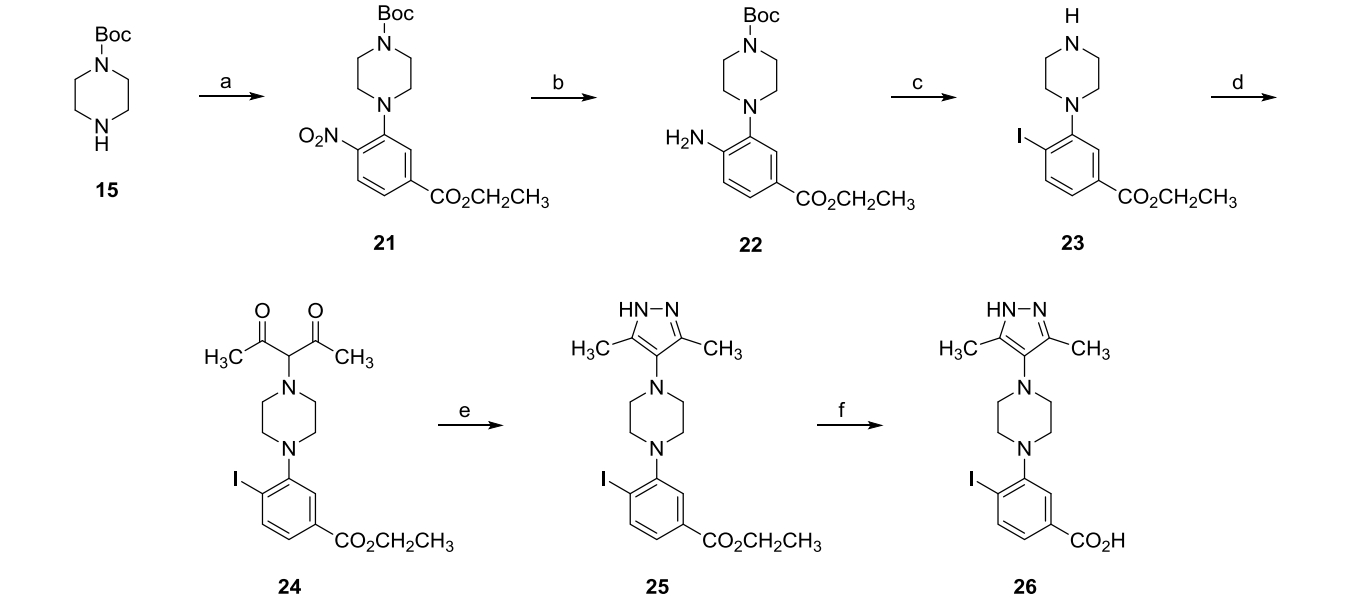

[a]Reagents and conditions: (a) ethyl 3-fluoro-4-nitrobenzoate, potassium carbonate (K_2CO_3), CH_3CN, 60 °C, 16 h; (b) H_2 (1 atm pressure), 10% Pd/C, CH_3OH, rt, 24 h; (c) (i) 0.25 N aqueous H_2SO_4, sodium nitrite ($NaNO_2$), H_2O, 0 °C, 30 min; (ii) KI, urea, rt, 1 h; (d) 3-chloropentane-2,4-dione, *i*-Pr_2NEt, THF, 0 °C to rt, 16 h; (e) $N_2H_4{\cdot}H_2O$ (64−65% in H_2O), THF, rt, 1 h; (f) (i) anhydrous LiOH, CH_3OH, THF, H_2O, rt, 3 h; (ii) 2 N aqueous HCl.

Scheme 3

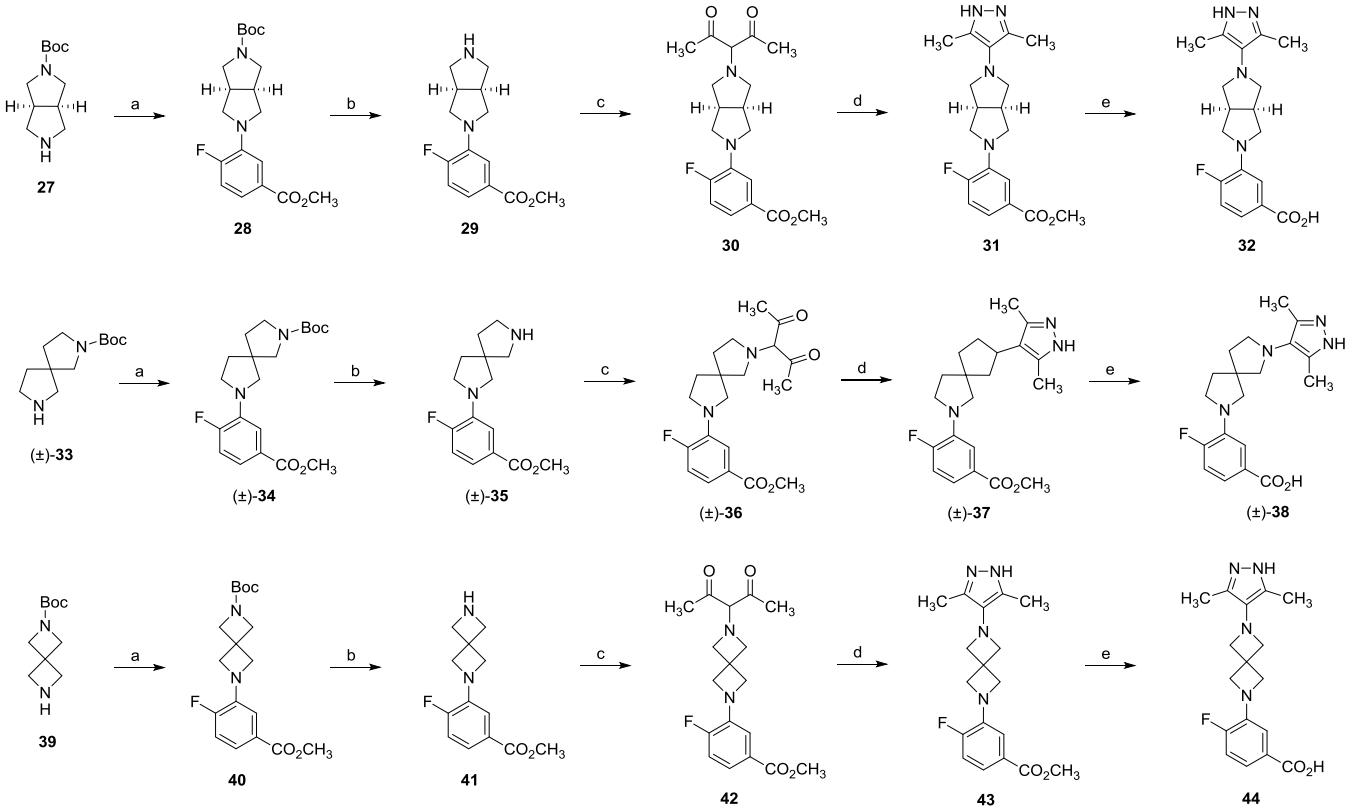

[a]Reagents and conditions: (a) *tert*-butyl (3a*R*,6a*S*)-hexahydropyrrolo[3,4-*c*]pyrrole-2(1*H*)-carboxylate (**27**), (±)-*tert*-butyl 2,7-diazaspiro[4.4]-nonane-2-carboxylate ((±)-**33**), or *tert*-butyl 2,6-diazaspiro[3.3]heptane-2-carboxylate (**39**), methyl 3-bromo-4-fluorobenzoate, X-Phos, $Pd_2(dba)_3{\cdot}CHCl_3$, Cs_2CO_3, 1,4-dioxane, sealed vessel at 110 °C, 16 h; (b) TFA, CH_2Cl_2, 0 °C to rt, 3 h; (c) 3-chloropentane-2,4-dione, *i*-Pr_2NEt, THF, 0 °C to rt, 16 h; (d) $N_2H_4{\cdot}H_2O$ (64−65% in H_2O), THF, rt, 1 h; (e) (i) anhydrous LiOH, CH_3OH, THF, H_2O, rt, 3 h; (ii) 2 N aqueous HCl.

https://doi.org/10.1021/acs.jmedchem.1c00099
J. Med. Chem. 2021, 64, 9010−9041

Scheme 4

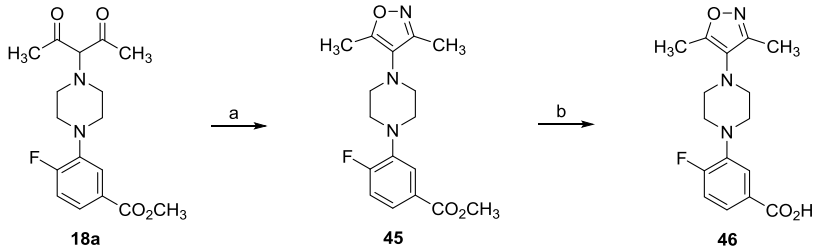

[a]Reagents and conditions: (a) $NH_2OH{\cdot}HCl$, CH_3OH, rt, 16 h; (b) (i) anhydrous LiOH, CH_3OH, THF, H_2O, rt, 1 h; (ii) 2 N aqueous HCl.

Scheme 5

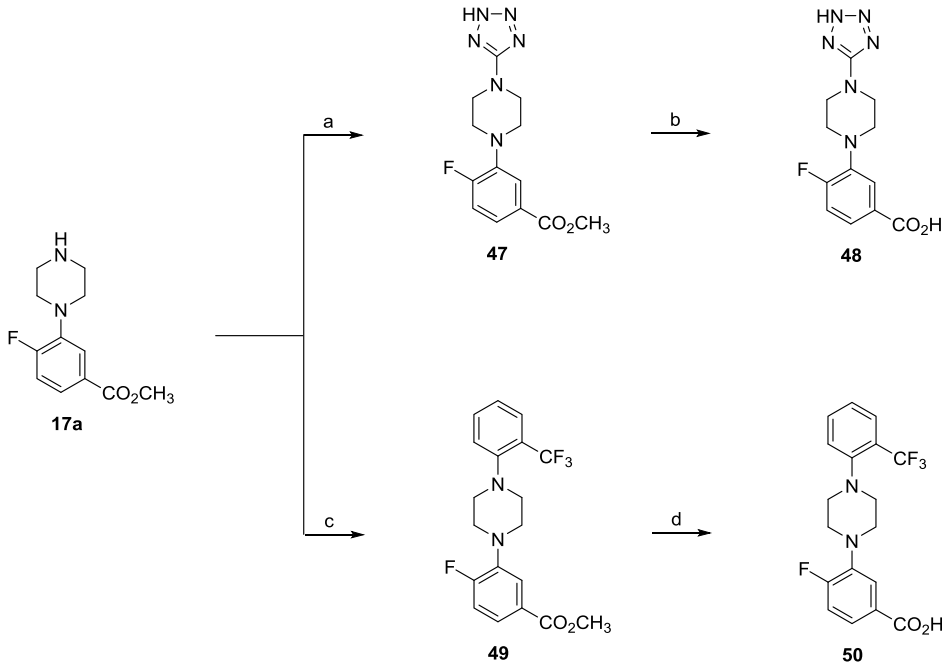

[a]Reagents and conditions: (a) (i) CNBr, *i*-Pr_2NEt, THF, 0 °C to rt, 1 h, (ii) ammonium chloride (NH_4Cl), NaN_3, DMF, 120 °C, 12 h; (b) (i) anhydrous LiOH, CH_3OH, THF, H_2O, rt, 1 h; (ii) 2 N aqueous HCl; (c) 1-bromo-2-(trifluoromethyl)benzene, X-Phos, $Pd_2(dba)_3{\cdot}CHCl_3$, Cs_2CO_3, 1,4-dioxane, sealed vessel, 110 °C, 16 h; (d) (i) anhydrous LiOH, CH_3OH, THF, H_2O, rt, 1 h; (ii) 2 N aqueous HCl.

Scheme 6

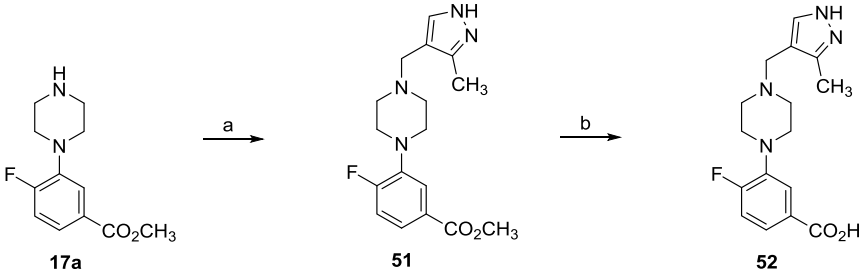

[a]Reagents and conditions: (a) 3-methyl-1*H*-pyrazole-4-carbaldehyde, $NaBH(OAc)_3$, acetic acid (HOAc), 1,2-dichloroethane, 60 °C, 12 h; (b) (i) anhydrous LiOH, CH_3OH, THF, H_2O, rt, 3 h; (ii) 2 N aqueous HCl.

hexahydropyrrolo[3,4-*c*]pyrrole-2(1*H*)-carboxylate (**27**), (±)-*tert*-butyl 2,7-diazaspiro[4.4]nonane-2-carboxylate ((±)-**33**), and *tert*-butyl 2,6-diazaspiro[3.3]heptane-2-carboxylate (**39**)) and methyl 3-bromo-4-fluorobenzoate. TFA-promoted *N*-Boc deprotection followed by 3,5-dimethyl-1*H*-pyrazole construction was conducted using the same three-step process as outlined in Scheme 1. LiOH-mediated hydrolysis of the corresponding methyl esters followed by neutralization of the lithium carboxylate salts with 2 N aqueous HCl provided the desired piperazine ring isostere analogues **32**, (±)-**38**, and **44**.

The previously described dione intermediate 3-(4-(2,4-dioxopentan-3-yl)piperazin-1-yl)-4-fluorobenzoate (**18a**) also afforded a handle for the construction of isoxazole **46** (Scheme 4), an analogue bearing a 3,5-dimethyl-1*H*-pyrazole head group isostere. Condensation of **18a** with hydroxyl amine hydrochloride ($NH_2OH{\cdot}HCl$) provided methyl 3-(4-(3,5-dimethyli-

https://doi.org/10.1021/acs.jmedchem.1c00099
J. Med. Chem. 2021, 64, 9010−9041

Scheme 7

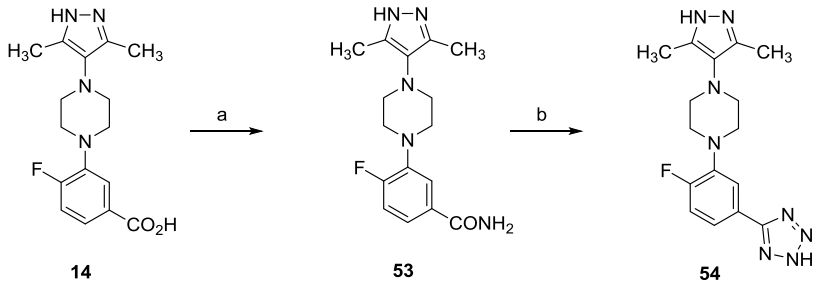

[a]Reagents and conditions: (a) NH_4Cl, HBTU, *i*-Pr_2NEt, DMF, rt, 18 h; (b) NaN_3, tetrachlorosilane, CH_3CN, 80 °C, 18 h.

soxazol-4-yl)piperazin-1-yl)-4-fluorobenzoate (**45**), which was hydrolyzed with anhydrous LiOH followed by neutralization with 2 N aqueous HCl to give the final product 3-(4-(3,5-dimethylisoxazol-4-yl)piperazin-1-yl)-4-fluorobenzoic acid (**46**).

Scheme 5 presents the routes starting with aryl piperazine intermediate **17a** that enabled the preparation of both tetrazole head group analogue **48** and 2-trifluoromethylphenyl head group analogue **50**. Treatment of **17a** with cyanogen bromide (CNBr) at 0 °C in THF in the presence of *N*,*N*-diisopropylethylamine (*i*-Pr_2NEt) afforded an intermediary cyanopiperazine, which underwent cycloaddition with sodium azide (NaN_3) in *N*,*N*-dimethylformamide (DMF) at 120 °C to give tetrazole **47**. Subsequent LiOH saponification of the methyl ester of **47** and neutralization of the lithium carboxylate salt with 2 N aqueous HCl gave the desired tetrazole **48**. The preparation of 2-trifluoromethylphenyl analogue **50** began with a palladium(0)-catalyzed amination between **17a** and 1-bromo-2-(trifluoromethyl)benzene to give methyl ester intermediate **49**. The aforementioned saponification and neutralization process was conducted with **49** affording the desired 2-trifluoromethylphenyl head group analogue **50**.

The preparation of the homologated variant of **14**, analogue **52**, is shown in Scheme 6. A sodium triacetoxyborohydride ($NaBH(OAc)_3$)-mediated reductive amination between amine **17a** and 3-methyl-1*H*-pyrazole-4-carbaldehyde provided methyl ester **51**, which upon saponification and subsequent 2 N aqueous HCl neutralization provided the desired homologated analogue **52**.

Replacement of the carboxylic acid of **14** with a primary carboxamide (**53**) and the bioisostere tetrazole (**54**) was also explored (Scheme 7). Production of primary carboxamide **53** involved amide bond formation between ammonium chloride and **14** using the peptide coupling agent *O*-(benzotriazol-1-yl)-*N*,*N*,*N*′,*N*′-tetramethyluronium hexafluorophosphate (HBTU). The bioisostere tetrazole **54** was furnished from **53** using tetrachlorosilane-sodium azide (NaN_3). Tetrachlorosilane-mediated dehydration of primary carboxamide **53** afforded the corresponding nitrile *in situ*, which underwent 1,3-dipolar cycloaddition with NaN_3 to afford tetrazole **54** in one pot.

RESULTS AND DISCUSSION

Structure–Activity Relationships. Compound binding potency (IC_{50} values) of novel compounds for unliganded TTR tetramers isolated from human plasma was measured using an established fluorescence polarization assay designed for TTR kinetic stabilizers.[41] The assay measured competitive displacement of a fluorescent probe (fluorescein isothiocyanate (FITC) coupled to a diclofenac analogue *via* a PEGylated linker) from TTR.

The less favorable entropic binding energy observed with the reported ITC thermogram of AG10 relative to tafamidis (AG10 $T\Delta S$ = −2.26 kcal/mol; tafamidis $T\Delta S$ = 6.39 kcal/mol)[42,43] may potentially be attributed to the conformational flexibility of the *n*-propyloxy core linker, which contains five rotatable bonds. Thus, our initial goal was to prepare a conformationally constrained congener of AG10 by installing a piperazine ring as a replacement for the *n*-propyloxy linker. We hoped to potentially further improve potency relative to AG10 by maintaining its key enthalpic contributions to binding while ameliorating a putative entropic penalty by reducing the number of rotatable bonds within the molecule's linker region. Indeed, piperazine **14** did exhibit excellent potency at TTR (TTR FP IC_{50} = 220 nM) that was approximately 2-fold better than tafamidis (TTR FP IC_{50} = 410 nM) and comparable to that of AG10 (TTR FP IC_{50} = 160 nM) (Table 1).

With **14** in hand, we next sought to explore the SAR effects of varying the substituents and substitution patterns of the benzoic acid bottom-group motif. We prepared a focused sample set of follow-up analogues to **14** that replaced its *para*-fluorine atom with alternative groups that might better occupy the neighboring HBP1 pocket, stabilize a putative forward binding pose, and potentially further improve potency (**20a–e**). The HBP1 pocket, and its twofold symmetry-related HBP1′ pocket, resides near the outer binding cavity and is occupied by one of the iodine atoms of T4. They are hydrophobic and are composed of residues Leu17, Thr106, and Val121 as well as the methylene groups of Lys15 and Glu54. Our docking model predicted that the fluorine of **14** would project toward HBP1 in a similar manner as the fluorine of AG10. Therefore, we sought to initially explore this region of the scaffold to see if substituents other than fluorine could lead to improved potency *via* better HBP1 occupancy and more robust van der Waals binding interactions. To that end, our initial sample set included substituents that were larger and more lipophilic than fluorine (Table 1). With the exception of des-fluoro analogue **20a** (TTR FP IC_{50} = 780 nM), all of the analogues of this sample set were well tolerated and exhibited potencies within a twofold range of **14**. Indeed, para-substituted analogues **20b–e** are equipotent to **14**. We also replaced the fluorine of **14** with the larger, more lipophilic, and halogen bond-donating iodine that is featured on T4 (**26**), and this analogue was also found to be an active TTR ligand within our portfolio, exhibiting comparable potency relative to the parent fluoro compound **14** and AG10 (**26** TTR FP IC_{50} = 190 nM). We plan to follow up on this emerging SAR and test future analogues presenting larger and more sterically bulky substituents (*e.g.*, isopropyl, *tert*-butyl, cyclopropyl, cyclobutyl, *etc.*)

https://doi.org/10.1021/acs.jmedchem.1c00099
J. Med. Chem. 2021, 64, 9010–9041

Table 1. TTR FP and RBP4 SPA *In Vitro* Assay Data for Piperazine-Containing TTR Tetramer Kinetic Stabilizers Bearing Various Benzoic Acid Substituents (Bottom-Group Region SAR)[a]

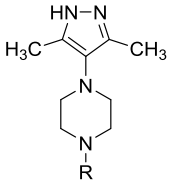

Compound	Benzoic Acid Bottom Group Motif (R)	TTR FP[a] IC_{50} (μM)[d]	RBP4 SPA[b] IC_{50} (μM)[d]	RBP4-TTR HTRF[c] IC_{50} (μM)[d]
Tafamadis (4)	---	0.41	>30	0.981
AG10 (5)	---	0.16	>30	0.512
14	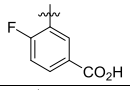	0.22	>3	0.845
20a	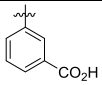	0.78	>30	ND[e]
20b	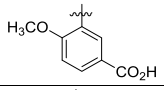	0.30	>3	0.583
20c	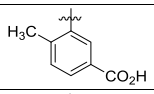	0.21	>3	ND[e]
20d	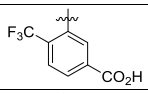	0.26	>3	3.56
20e	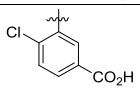	0.20	>3	1.74
20f	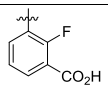	0.55	>3	ND[e]
20g	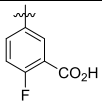	1.44	>3	ND[e]
20h	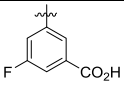	0.62	>3	ND[e]
20i	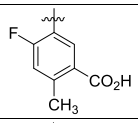	0.60	>3	24.01
26	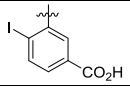	0.19	ND	2.65

[a]IC_{50} values for the TTR FP assay obtained in the presence of a fixed, 25 μM concentration of fluorescein isothiocyanate (FITC)-coupled TTR FP probe. [b]IC_{50} values for the RBP4 SPA assay obtained in the presence of a fixed, 10 nM concentration of ^{3}H-retinol. [c]IC_{50} values for the HTRF assay obtained in the presence of 1 μM concentration of retinol. [d]For compounds tested multiple times (more than twice), the IC_{50} data is represented as the mean ± standard deviation (SD). For those compounds that were only tested twice, the IC_{50} data is shown as the mean of two independent experiments and not as the mean ± standard deviation. [e]ND, not determined.

and polar substituents (*i.e.*, oxetane, nitrile, *etc.*) to further probe the capacity of HBP1 and to determine if such substituents can lead to more potent scaffolds within our series.

The improved potency observed for several analogues within our series relative to tafamidis may suggest the compounds' benefit from increased enthalpic contributions to binding *via* putative H-bonds between their respective pyrazole head groups and Ser117/Ser117′ in a similar manner as AG10, which would be consistent with the binding pose of **14** predicted by our computational docking model. The lack of further improvement in potency for the series relative to AG10 may be attributed to several factors. For example, potential entropic benefits for

https://doi.org/10.1021/acs.jmedchem.1c00099
J. Med. Chem. 2021, 64, 9010−9041

Table 2. TTR FP and RBP4 SPA *In Vitro* Assay Data for Conformationally Constrained Piperazine Isostere TTR Tetramer Kinetic Stabilizer Analogues (Core Scaffold Region SAR)

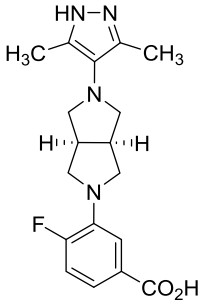

32

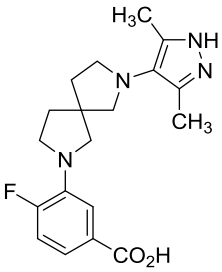

(±)-38

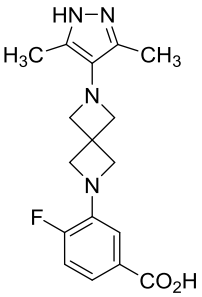

44

compound	TTR FP[a] IC_{50} (μM)[c]	RBP4 SPA[b] IC_{50} (μM)[c]
14	0.22	>3
32	2.82	>3
(±)-**38**	1.08	>3
44	>30	>3

[a]IC_{50} values for the TTR FP assay obtained in the presence of a fixed, 25 μM concentration of fluorescein isothiocyanate (FITC)-coupled TTR FP probe. [b]IC_{50} values for the RBP4 SPA assay obtained in the presence of a fixed, 10 nM concentration of ^{3}H-retinol. [c]For compounds tested multiple times (more than twice), the IC_{50} data is represented as the mean ± standard deviation. For those compounds that were only tested twice, the IC_{50} data is shown as the mean of two independent experiments and not as the mean ± standard deviation.

binding gained may be slightly offset by subtle adverse changes to enthalpic contributions. It is possible that the more electron-rich amino pyrazole head group of our series presents a slightly weaker H-bond-donating group relative to the pyrazole of AG10, which could affect the strength of the Ser117/Ser117′ H-bond interaction. Furthermore, replacing the aryl ether of AG10 with the aryl amine for our compounds may alter the pK_a of the carboxylic acid and modulate the strength of its interactions with Lys15/Lys15′. Additionally, our piperazine-containing scaffolds may be unable to attain a fully suitable bioactive conformation to allow for the optimal pyrazole head group and/or carboxylic acid bottom-group binding interactions due to the reduced flexibility of the core. The increased rigidity imposed by the piperazine core may actually not confer a significant entropic benefit and may prevent optimal occupancy required for fortified H-bond, van der Waals, and hydrophobic effect contributions. Alternatively, it may also be possible that the potencies exhibited by AG10 and **14** and **26** may simply represent the upper limit for ligand binding affinity at the T4 site.

We next investigated whether moving the fluorine of **14** from the para position relative to the carboxylic acid to the corresponding ortho and meta positions would have an effect on TTR potency (**20f**−**h**). Interestingly, the SAR for this group demonstrated a preference for fluorine substitution para to the carboxylic acid. The ortho-fluorinated analogue **20f** (TTR FP IC_{50} = 550 nM) exhibited a >2-fold loss in potency relative to **14**, while the alternate ortho-substituted fluorinated analogue **20g** exhibited a greater loss in potency (∼6.5-fold) (TTR FP IC_{50} = 1.44 μM). The *meta*-fluoro analogue **20h** (TTR FP IC_{50} = 620 nM) was nearly equipotent with **20f**. The relatively modest decrease in potency observed for **20f** and **20h** may be attributed to their respective fluorine atoms being unable to optimally project into and fully occupy the HBP1′ or HBP1 pocket, potentially leading to weaker van der Waals interactions and destabilized binding poses. Contrarily, the substitution pattern of **20g** may potentially project the fluorine atom into an area that does not allow it to occupy either HBP1 or HBP1′ and/or engage in any favorable binding interactions, thus leading to the more significant loss in potency exhibited. Finally, we prepared and tested the disubstituted analogue **20i** that incorporated a methyl group ortho (2-position) to the carboxylic acid, which could serve as a potential blocking group to hinder a possible acyl glucuronidation metabolic pathway. Gratifyingly, the compound was active and exhibited good potency (TTR FP IC_{50} = 600 nM). As previously stated, uridine 5′-diphosphoglucuronosyltransferase (UGT) acyl glucuronidation has been identified as the predominant metabolic pathway of AG10.[61] As acyl glucuronidation is reported to be associated with an increased incidence of idiosyncratic toxicity,[62] the diminishment or elimination of this metabolic pathway should be considered during the early stages of drug discovery to potentially remove or hinder the probability of encountering this liability. Although AG10 has been found to be safe and well tolerated clinically, we wanted to investigate early-stage analogues that may potentially hinder an acyl glucuronidation metabolic pathway for our series. Thus, the introduction of a methyl group within close proximity to the nucleophilic carboxylate moiety was anticipated to sterically encumber and reduce its accessibility to UGT and the UDP-glucuronic acid cofactor, potentially impairing or prohibiting acyl glucuronidation.[63] Future metabolite profiling and structural elucidation studies will be conducted to investigate whether **14** and/or **20i** are subject to acyl glucuronidation *in vivo* and if there are significant differences observed with regard to the extent of this type of metabolism between the two analogues.

In addition to TTR binding, we also tested our compounds, together with tafamidis and AG10, in the *in vitro* RBP4 scintillation proximity (SPA) assay, which is used to measure binding potency of all-*trans*-retinol-competitive ligands at RBP4. Neither tafamidis, AG10, nor any of our novel TTR ligands exhibited activity at RBP4 in this assay (RBP4 SPA IC_{50} for all compounds tested >3 μM). We also tested our most potent TTR ligands in the RBP4−TTR HTRF assay,[3−7] which is typically used to determine the all-*trans*-retinol-competitive RBP4 antagonist potency for inhibiting the holo-RBP4−TTR complex formation. Interestingly, despite a lack of activity in the RBP4 SPA assay, we did observe activity in the RBP4−TTR

https://doi.org/10.1021/acs.jmedchem.1c00099
J. Med. Chem. 2021, 64, 9010−9041

HTRF assay for some of the compounds tested from this portfolio. Tafamidis, AG10, **14**, **20b**, **20d**, **20e**, and **26** were all found to exhibit single-digit to submicromolar IC_{50} potency values in this assay, providing evidence that the compounds are also capable of hindering holo-RBP4−TTR complexation. Interestingly, compound **20i** exhibited very weak activity in this assay, despite presenting TTR potency that is comparable to the aforementioned HTRF-active compounds.

We next explored the SAR effects of a focused sample set of three piperazine ring isostere core linker analogues (Table 2). The (3a*S*,6a*S*)-octahydropyrrolo[3,4-*c*]pyrrole fused bicyclic analogue **32** exhibited an order of magnitude loss in potency relative to **14** (TTR FP IC_{50} = 2.82 μM), while racemic 2,7-diazaspiro[4.4]nonane (±)-**38** was found to be 5-fold less potent (TTR FP IC_{50} = 1.08 μM). 2,6-Diazaspiro[3.3]heptane **44** was inactive at TTR. None of the piperazine isostere analogues demonstrated activity in the *in vitro* RBP4 SPA assay. The diminishment in potency or complete loss of activity for these compounds could be attributed to either the longer lengths or unfavorable geometries (or both) of the linkers, which prohibited the formation of compatible binding poses within the T4 site. Due to their poor binding at TTR, these compounds were not profiled for activity in the RBP4−TTR HTRF assay.

A concise exploration of 3,5-dimethyl-1*H*-pyrazole head group SAR for analogue **14** was also conducted (**46**, **48**, **50**, and **52**) (Table 3). Previous reports indicate very tight SAR for this region as exchanging the methyl groups of the 3,5-dimethyl-1*H*-pyrazole of AG10 (**5**) with ethyl groups or methylation of one of the pyrazole nitrogen atoms was not well tolerated.[29] Thus, we prepared a focused sample set that was designed to further probe the nature of the T4 inner binding cavity. Replacement of the 3,5-dimethyl-1*H*-pyrazole of **14** with a 3,5-dimethylisoxazole ring (**46**) was not well tolerated and leads to a >20-fold loss in potency (TTR FP IC_{50} = 5.3 μM). This observation may be attributed to the installation of a poorer H-bond-accepting isoxazole ring system, which may have led to significantly weaker putative H-bonds with Ser117 and Ser117′ relative to **14**. Incorporation of a tetrazole group (**48**) led to a complete loss in TTR activity, which may be attributed to (1) the contrasting polarity of the tetrazole with the hydrophobic macromolecular interior of the inner T4 binding site and/or (2) the lack of pendant methyl groups to occupy the adjacent HBP3 and HBP3′ pockets. Interestingly, replacing the 3,5-dimethyl-1*H*-pyrazole of **14** with a 2-trifluoromethylphenyl head group (**50**) also led to a diminishment in potency (TTR FP IC_{50} = 1.7 μM), though not as severe as was observed for isoxazole **46** and tetrazole **48**. The 2-trifluoromethylphenyl head group of **50** is significantly more hydrophobic than the 3,5-dimethyl-1*H*-pyrazole, and it is incapable of H-bond interactions with Ser117 and Ser117′. Furthermore, the X-ray crystal structure PDB 4HIQ indicates that there is insufficient space between the symmetry-related side chains of Ser117 to accommodate the size of the 2-trifluoromethylphenyl ring. We speculate that the relatively moderate loss in potency observed for **50** may be due to an alternative binding pose similar to that reported for TTR stabilizer **12**,[51,51] which could involve the benzoic acid of **50** projecting inward and toward HPB3 and Ser117, while the 2-trifluoromethylphenyl ring is positioned closer to the opening of the binding site where it may engage HPB2 and/or HBP3. It is unclear at this time as to why this compound exhibits moderate potency and we plan to obtain an X-ray crystal structure of it cocrystallized with TTR to determine its mode of binding. The 3-methyl-1*H*-pyrazol-4-yl analogue **52** was found to be inactive.

Table 3. TTR FP and RBP4 SPA *In Vitro* Assay Data for TTR Tetramer Kinetic Stabilizer Analogues Bearing 3,5-Dimethyl-1*H*-pyrazole Replacements (Head Group Region SAR)

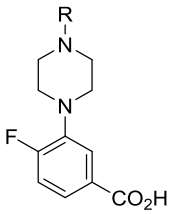

Compound	Head Group (R)	TTR FP[a] IC_{50} (μM)[c]	RBP4 SPA[b] IC_{50} (μM)[c]
14	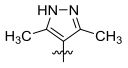	0.22	>3
46	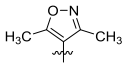	5.3	>3
48		>30	>3
50		1.7	>3
52		>30	>30

[a]IC_{50} values for the TTR FP assay obtained in the presence of a fixed, 25 μM concentration of fluorescein isothiocyanate (FITC)-coupled TTR FP probe. [b]IC_{50} values for the RBP4 SPA assay obtained in the presence of a fixed, 10 nM concentration of ^{3}H-retinol. [c]For compounds tested multiple times (more than twice), the IC_{50} data is represented as the mean ± standard deviation. For those compounds that were only tested twice, the IC_{50} data is shown as the mean of two independent experiments and not as the mean ± standard deviation.

We then examined two replacements for the carboxylic acid of **14**, which included primary carboxamide **53** and the bioisostere tetrazole **54**. Carboxamide **53** exhibited good potency and was approximately 3-fold less potent than **14**. This is presumably due to the fact that the primary carboxamide, although capable of serving as a H-bond donor and acceptor that can form strong charge-reinforced H-bonds with Lys15/Lys15′ and Glu54/Glu54′, is nonionizable and unable to engage in stronger electrostatic interactions that the carboxylic acid of **14** is capable of. The tetrazole of **54** is ionizable at physiological pH and serves as a suitable bioisostere of the carboxylic acid, thus likely allowing it to participate in similar electrostatic interactions with Lys15/Lys15′, which may explain why it is equipotent with **14**. As an additional beneficial attribute, the tetrazole of **54** may also serve to potentially hinder acyl glucuronidation. Interestingly, despite conferring TTR potency and selectivity that is comparable to **14** (TTR FP IC_{50} = 0.26 nM; RBP4 SPA IC_{50} > 3 μM), tetrazole **54** exhibited an approximate 10-fold loss in potency in the RBP4−TTR HTRF assay (RBP4−TTR HTRF IC_{50} = 9.58 μM) (Table 4).

We next evaluated our most potent compounds from our SAR campaign for their corresponding ADME properties. The *in vitro*

https://doi.org/10.1021/acs.jmedchem.1c00099
J. Med. Chem. 2021, 64, 9010−9041

Table 4. TTR FP and RBP4 SPA *In Vitro* Assay Data for Primary Carboxamide and Tetrazole TTR Tetramer Kinetic Stabilizer Analogues (Bottom-Group Region SAR)

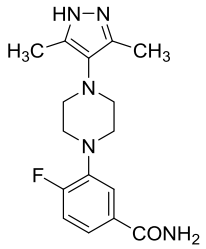

53

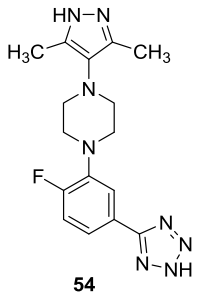

54

compound	TTR FP[a] IC_{50} (μM)[d]	RBP4 SPA[b] IC_{50} (μM)[d]	RBP4−TTR HTRF[c] IC_{50} (μM)[d]
14	0.22	>3	0.845
53	0.67	>3	ND[e]
54	0.26	>3	9.58

[a]IC_{50} values for the TTR FP assay obtained in the presence of a fixed, 25 μM concentration of fluorescein isothiocyanate (FITC)-coupled TTR FP probe. [b]IC_{50} values for the RBP4 SPA assay obtained in the presence of a fixed, 10 nM concentration of ^{3}H-retinol. [c]IC_{50} values for the HTRF assay obtained in the presence of a 1 μM concentration of retinol. [d]For compounds tested multiple times (more than twice), the IC_{50} data is represented as the mean ± standard deviation. For those compounds that were only tested twice, the IC_{50} data is shown as the mean of two independent experiments and not as the mean ± standard deviation. [e]ND, not determined.

pharmacological profiles presented in Table 5 show that all of the compounds possess excellent kinetic aqueous solubility in phosphate-buffered saline (PBS) (pH = 7.4), excellent microsomal stability with low intrinsic clearance (CL_{int}) values across multiple species, and suitable % plasma protein binding (PPB) values that largely indicate relatively low fraction unbound in human, rat, and mouse. Compound **14** emerged from this collection as the lead because it was among the most potent in the series that presented the best cytochrome P450 (CYP) inhibition profile. Further analysis of **14** revealed that the compound did not demonstrate any limiting off-target pharmacology at the human ether-a-go-go (hERG) channel (hERG IC_{50} > 30 μM; five-point dose−response (n = 2), electrophysiological patch-clamp (QPatch) assay) or at the nuclear peroxisome proliferator-activated receptor-γ receptor (PPARγ) (PPARγ EC_{50} > 30 μM). PPARγ agonists may potentially induce adverse effects, which include risk for fluid retention, weight gain, bone loss, and congestive heart failure.[64] Our previously reported RBP4 antagonist **BPN-14136** (structure not shown)[5,10,11] was found to exhibit modest agonist activity for the receptor (PPARγ IC_{50} = 3.6 μM in the agonist-induced corepressor NCoR release assay). Due to the fact that **14** shares some structural complementarity with **BPN-14136** and with reported PPARγ agonists, we surveilled our novel TTR tetramer kinetic stabilizer series for this undesirable off-target pharmacology.

Analogue 14 Inhibits Formation of High-Molecular-Weight Forms of TTR. The ability of TTR ligands to act as kinetic stabilizers of TTR tetramers can be assessed *in vitro* using a low pH-induced TTR aggregation sodium dodecyl sulfate-polyacrylamide gel electrophoresis (SDS-PAGE) assay.[65] A 72 h incubation of TTR tetramers at pH = 4.0 initiates its dissociation into monomeric intermediates that misassemble and oligomerize into amyloid fibrils and other high-molecular-weight forms.[65,66] To confirm the ability of analogue **14** to act as a kinetic stabilizer of TTR tetramers, we tested its ability to suppress low pH-mediated TTR aggregate formation using the previously published protocol. Tafamidis was used as a positive control in the aggregation experiments. As shown in Figure 8A, following 72 h of incubation of TTR tetramers with dimethyl sulfoxide (DMSO) at pH = 4 at 37 °C, the amount of high-molecular-weight forms of TTR is greatly increased in comparison to the DMSO control incubated for 72 h at pH = 7.5. Consistent with its ability to act as a kinetic TTR stabilizer, treatment with analogue **14** (50 μM) as well as with tafamidis (50 μM), significantly inhibited the formation of high-molecular-weight forms of TTR (Figure 9A). Higher intensities of the TTR monomer and dimer bands in samples treated with **14** and tafamidis when compared to that of DMSO correlated with a corresponding reduction in TTR aggregates induced by **14** and tafamidis. Quantification of Western blot band intensities established a 3.1-fold reduction in the amount of aggregates in the presence of **14**, while a 3.0-fold reduction was induced by tafamidis (Figure 9B). Significant increase in the dimer band intensities and appreciable increase in the intensity of TTR monomer bands conferred by **14** and tafamidis were associated with inhibition of the low pH-induced TTR aggregate formation (Figure 9C,D). The results of the conducted aggregation experiments confirmed that **14** can act as a TTR tetramer kinetic stabilizer.

***In Vivo* Activity: PK Characteristics of 14 in Mice.** The PK properties of **14** were determined *via* studies conducted with CD-1 male mice (2 mg/kg intravenous (IV) and 5 mg/kg oral (PO)) (Table 6). The compound exhibited a favorable plasma clearance (0.354 L/(h kg)) and a good half-life of 5.08 h. Rapid oral absorption was observed (T_{max} = 0.42 h) with a maximal concentration (C_{max}) of 1563 ng/mL. Compound **14** presented a low volume of distribution (V_{ss} = 2.19 L/kg), good overall exposure (area under the curve $(AUC)_{INF}$ was 16 073 h ng/mL), and excellent oral bioavailability (%F = 103%). The observed slightly >100% oral bioavailability for **14** may be the result of its low plasma clearance and potential nonlinear pharmacokinetics over the dose range tested or it may be due in part to enterohepatic recycling.

***In Vivo* Activity: RBP4-Lowering and PK−Pharmacodynamics (PD) Correlations of Analogue 14 in Mouse.** Taking into account that the levels of serum RBP4 depend on formation of the RBP4−TTR−all-*trans*-retinol complex in circulation, we wanted to establish that a selective TTR tetramer binding ligand can allosterically antagonize the retinol-dependent RBP4−TTR interaction and potentially be capable of reducing circulating RBP4 levels *in vivo*. We evaluated the effect of a single oral dose of **14** on dynamics of serum RBP4 levels in mice (Figure 10). After a single 25 mg/kg oral dose of **14**, a maximal 66% reduction in serum RBP4 levels was observed 2 h following the dose administration (Figure 10A). Given that T4 and synthetic TTR ligands may stimulate the secretion of certain TTR forms,[67] we assessed the effect of oral administration of **14** on circulating levels of transthyretin. No changes in serum TTR levels in response to **14** dosing were noted (data not shown). The dynamics of serum RBP4 changes induced by **14** demonstrated a very good correlation between the presence of the compound in circulation after oral dosing (Figure 10B) and a reduction in serum RBP4. The maximal RBP4 reduction seen at the 1 and 2 h time points correlated very well with rapid oral absorption (Table 6) that led to the high concentration of **14** in the blood at time points of the maximal serum RBP4 reduction.

https://doi.org/10.1021/acs.jmedchem.1c00099
J. Med. Chem. 2021, 64, 9010−9041

Table 5. ***In Vitro*** **ADME Profile for Selected TTR Tetramer Kinetic Stabilizer Compounds**

compound	TTR FP IC_{50} (μM)	solubility (μM)[a]	microsomal CL_{int} (mL/(min mg))[b]				liver microsomal stability (% remaining at 30 min)[c]				predicted half-life[d] (H, R, M, monkey)	CYP inhibition (% inhibition at 10 μM) 2C9, 2C19, 2D6, 3A4	%PPB[e]		
			H	R	M	monkey	HLM	RLM	MLM	monkey LM			H	R	M
14	0.22	184.5	<0.0231				93	98	102	94	>60 min for all species	2C9—10.4% 2C19—3.1% 2D6—8.1% 3A4—(−)2.2%	83	97	93
20b	0.30	200	<0.0231				108	101	102	102	>60 min for all species	2C9—1.4% 2C19—4.2% 2D6—8.0% 3A4—19.6%	75	78	ND
20d	0.21	200	<0.0231				101	101	97.5	96.7	>60 min for all species	2C9—17.1% 2C19—2.3% 2D6—5.9% 3A4—14.8%	86	91	ND
20c	0.26	200	<0.0231				97.8	96.6	96	100	>60 min for all species	2C9—56.2% 2C19—0.06% 2D6—7.34% 3A4—(−)5.2%	97	97	ND
20e	0.20	200	<0.0231				103	104	98	100	>60 min for all species	2C9—25.2% 2C19—1.85% 2D6—10.0% 3A4—19.5%	91	89	ND
20i	0.60	200	<0.0231				90	105	96	95.2	>60 min for all species	2C9—1.1% 2C19—(−)3.0% 2D6—9.2% 3A4—31.7%	87	93	ND
54	0.26	200	H = 0.0184; R, M, monkey <0.0231				71.4	98.2	91.5	95.7	H = 75.4 min; R, M, monkey <60 min	2C9—26.3% 2C19—(−)4.8% 2D6—0.8% 3A4—18.9%	92	94	ND

[a]Kinetic solubility measured in PBS (pH = 7.4). When the observed mean solubility is greater than 200 μM, the mean value is adjusted to the maximum assay concentration, which is 200 μM. [b]Microsomal intrinsic clearance (CL_{int}); H, human; R, rat; M, mouse; cyno, cynomolgus monkey. [c]Liver microsomal metabolic stability, % of parent drug remaining after a 30 min incubation in the presence of the microsomes; HLM, human liver microsomes; RLM, rat liver microsomes; MLM, mouse liver microsomes; monkey LM, monkey liver microsomes. %Remaining values shown as higher than 100% may be potentially attributed to error. [d]When the calculated half-life is longer than the duration of the experiment, the half-life is expressed as greater than the longest incubation time. [e]%PPB, plasma protein binding; H, human; R, rat; M, mouse.

https://doi.org/10.1021/acs.jmedchem.1c00099
J. Med. Chem. 2021, 64, 9010−9041

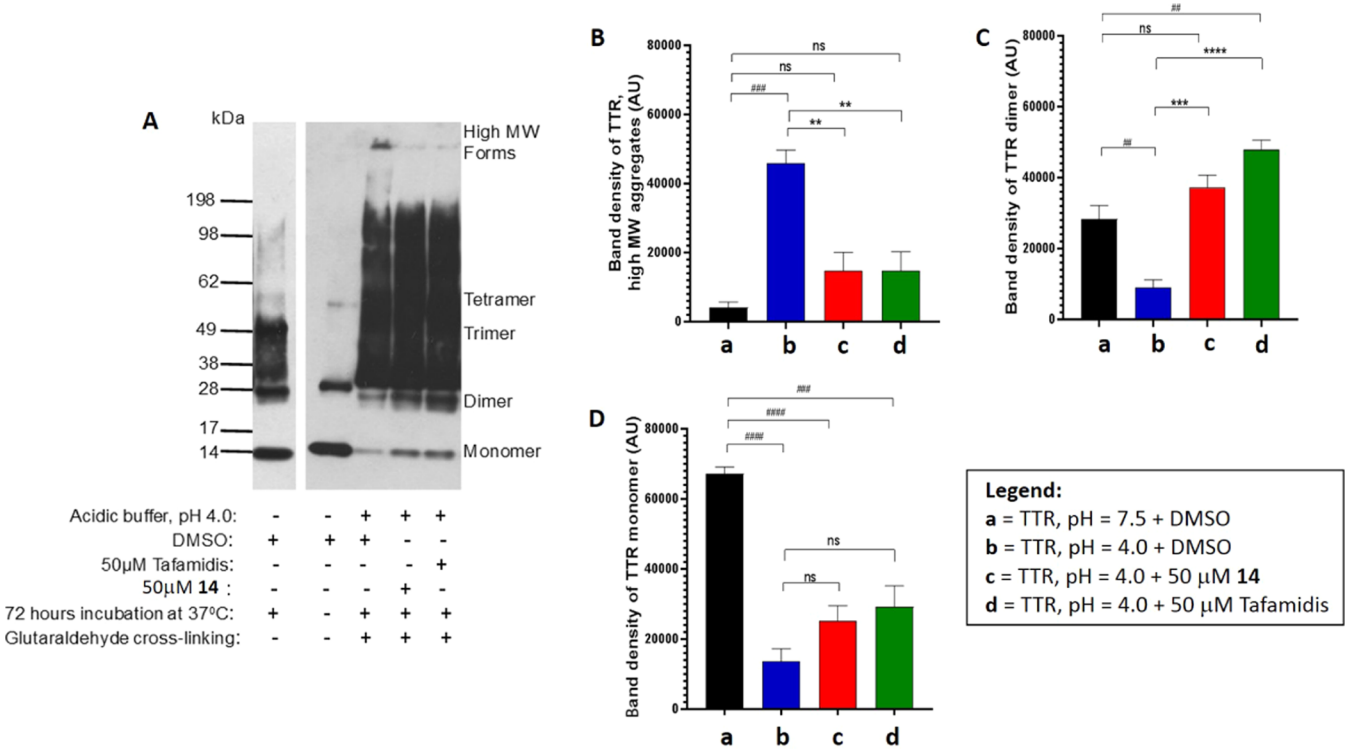

Figure 9. Analogue **14** reduces the formation of high-molecular-weight TTR forms in the acid-induced aggregation assay. TTR protein (5 μg) was aggregated using acetate buffer (pH = 4.0) and incubated for 72 h at 37 °C. TTR tetramer concentration during the incubation was 9 μM. After incubation in the presence of DMSO, 50 μM tafamidis, and 50 μM **14** and cross-linking with glutaraldehyde, samples were subjected to SDS-PAGE followed by Western blot analysis of TTR. The representative blot of at least three independent experiments is presented (A). Bar graphs represent the pixel volume means ± SD of the scanned bands on the immunoblots in arbitrary units for TTR high-molecular-weight aggregates (B), dimers (C), and monomers (D). Statistical significance was determined by one-way analysis of variance (ANOVA) with the Holm−Sidák *post hoc* test; *, $p \leq 0.05$; **, $p \leq 0.01$; ***, $p \leq 0.001$; ****, $p \leq 0.0001$ compared to TTR aggregation + DMSO group (pH 4.0); #, $p \leq 0.05$; ##, $p \leq 0.01$; ###, $p \leq 0.001$; ####, $p \leq 0.0001$ compared to TTR without aggregation group (pH = 7.5).

Table 6. ***In Vivo*** **PK Data for Analogue 14 Following IV and PO Administration in CD-1 Mice**[a]

route	dose (mg/kg)	C_0[b] (ng/mL)	CL[c] (L/(h kg))	$t_{1/2}$[d] (h)	V_{ss}[e] (L/kg)	AUC_{last}[f] (h ng/mL)	AUC_{INF}[g] (h ng/mL)	%F[j]
IV	2	1622 (267)	0.354 (0.139)	5.08 (0.814)	2.18 (0.585)	6214 (2321)	6242 (2303)	NA
route	dose (mg/kg)	C_{max}[h] (ng/mL)	T_{max}[i] (h)	$t_{1/2}$[d] (h)	V_{ss}[e] (mL/kg)	AUC_{last}[f] (h ng/mL)	AUC_{INF}[g] (h ng/mL)	%F[j]
PO	5	1563 (115)	0.42 (0.14)	5.38 (0.624)	NA	16 040 (2778)	16 073 (2783)	103 (17.8)

[a]Data are represented as the mean with standard deviation in parentheses (mean (SD)). Dosing groups consisted of three drug naïve adult male CD-1 mice. IV administration: test article was administered at the 2 mg/kg dose; test article vehicle = 3% dimethylacetamide (DMA)/45% poly(ethylene glycol) 300 (PEG300)/12% ethanol/40% sterile water; PO administration: test article was administered at the 5 mg/kg dose, vehicle = 2% Tween 80 in 0.9% saline. [b]Observed initial concentration of compound in blood at time zero. [c]Total body clearance. [d]Apparent half-life of the terminal phase of elimination of compound from blood. [e]Volume of distribution at steady state. [f]Area under the blood concentration *versus* time curve from 0 to the last time point that the compound was quantifiable in blood. [g]Area under the blood concentration *versus* time curve from 0 to infinity. [h]Maximum observed concentration of compound in blood. [i]Time of maximum observed concentration of compound in blood. [j]Bioavailability; $F = (AUC_{INFpo} \times dose_{iv})/AUC_{INFiv} \times dose_{po}$.

Compound clearance by 24 h matches well with the lack of the PD response at this time point.

To test whether members of the general class of TTR ligands may be able to reduce serum RBP4, we conducted a series of single oral dose experiments in Balb/c mice with established TTR tetramer stabilizers (tafamidis and AG10) as well as with our new analogues **14**, **20c**, and **20e**. Analogues **20c** and **20e** were chosen as they exhibited equivalent potency to **14** in the TTR FP assay and exhibited similar ADME profiles relative to **14**. A bis-hydrochloric salt of **14** (**14a**) was used in these experiments due to an observed improved solubility in the dosing vehicle (0.9% NaCl, 2% Tween 80). Despite variability in baseline levels of serum RBP4 between study groups, all tested compounds induced a significant reduction in circulating levels of RBP4 in comparison to the vehicle (Figure 11). Analogue **14a** showed superior RBP4-lowering efficacy in comparison to AG10 and tafamidis (81% serum RBP4 reduction at the 6 h time point), while tafamidis seems to have a longer duration of action (Figure 11). We plan to obtain PK data for analogues **20e**, **20c**, and **14a** to generate PK−PD correlations in a similar manner to **14**. Given that we and others previously established a very good correlation between pharmacological reduction of serum RBP4 and efficacy in the *Abca4*$^{-/-}$ mouse model of enhanced retinal lipofuscinogenesis,[10,68,69] our RBP4-lowering data for TTR ligands may indicate that members of a general class of TTR tetramer stabilizers could have utility in treating retinal diseases associated with accumulation of RPE lipofuscin.

https://doi.org/10.1021/acs.jmedchem.1c00099
J. Med. Chem. 2021, 64, 9010−9041

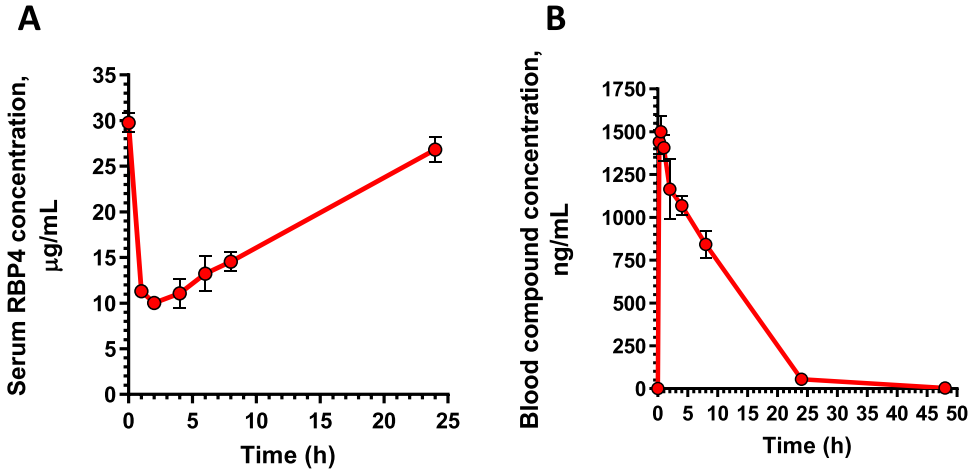

Figure 10. Pharmacokinetic and pharmacodynamic properties of 14 in mice. (A) Serum RBP4 levels following a single 25 mg/kg oral administration of **14**. (B) Blood compound levels following administration of a single oral 5 mg/kg dose of **14**. Data are presented as means ± SD. Three mice per treatment group were used in the PK−PD study.

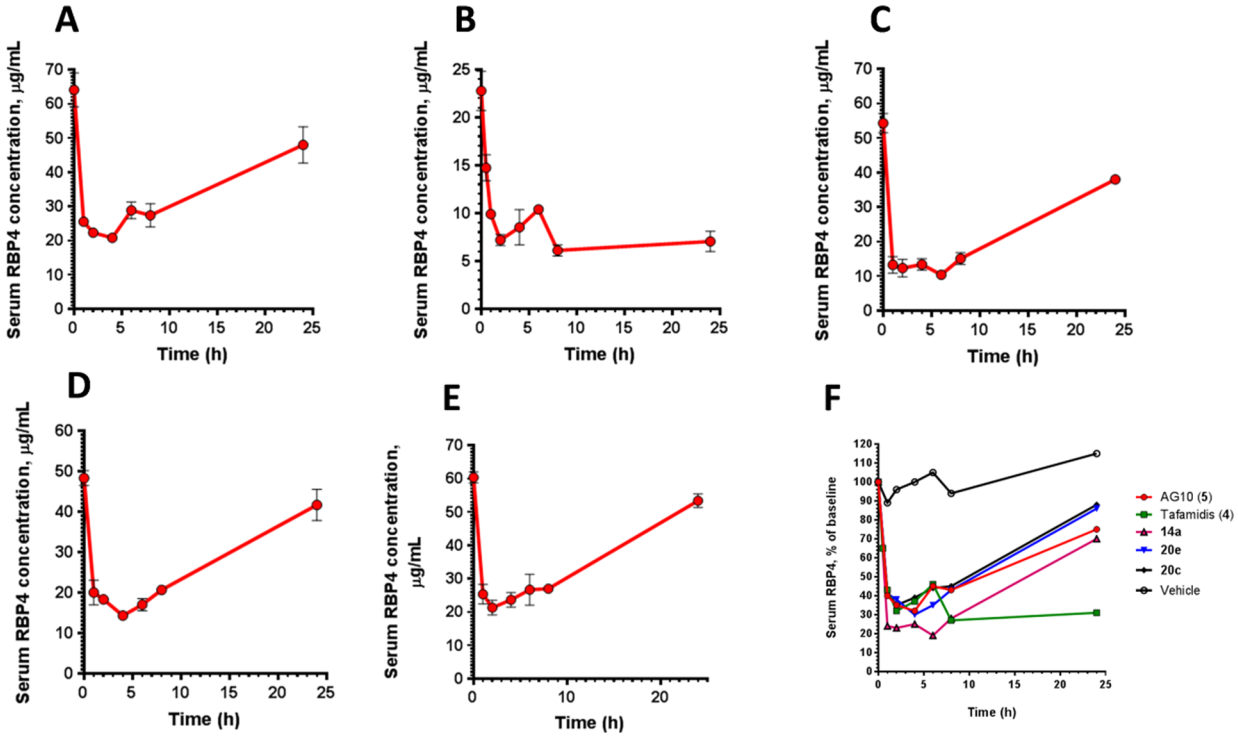

Figure 11. Effect of TTR ligands on circulating levels of serum RBP4 in Balb/c mice. Serum RBP4 levels were measured following a single oral administration of (A) AG10, (B) tafamidis, (C) **14a**, (D) **20e**, and (E) **20c**. Percent changes of serum RBP4 in comparison to the baseline levels (100%) are shown in (F) for test compounds as well as for the dosing vehicle (0.9% NaCl, 2% Tween 80). The oral dose was 25 mg/kg for AG10, **14a**, **20e**, and **20c**; the tafamidis dose was 50 mg/kg. Data represented as the mean ± SD. Three to eight mice per compound treatment group were used in the study.

It is currently unclear how **14** and other TTR ligands inhibit RBP4−TTR−all-*trans*-retinol complex formation, which seems to be the likely cause of serum RBP4-lowering. Indeed, tafamidis, AG10, **14**, and **20e** were all found to exhibit good potency in the RBP4−TTR HTRF assay, providing evidence that the compounds are in fact hindering complex formation. One possible mechanism of action may be that the binding of kinetic stabilizers such as **14** at the T4 site causes conformational changes to occur within the distal PPI interface domain that are unfavorable for holo-RBP4 association. For example, the aforementioned TTR residues Ile84, Val-20, and Ala-81 play pivotal roles in the formation of the PPI interface domain and mutations involving TTR Ile84 have deleterious consequences with regard to complex formation with holo-RBP4.[54] The K_d for the holo-RBP−TTR complex is approximately 0.4 μM, whereas the I84S mutation results in negligible TTR affinity for holo-RBP4 and abrogates complex formation.[54] Indeed, individuals expressing variants of TTR whereby Ile84 is replaced with either Ser or Asn have substantially lowered plasma concentrations of RBP4.[54] It may be possible that ligand binding at the T4 site causes a conformational shift that impedes Ile84 and/or other residues within the TTR hydrophobic patch from facilitating

https://doi.org/10.1021/acs.jmedchem.1c00099
J. Med. Chem. 2021, 64, 9010−9041

docking to holo-RBP4, in much the same manner as RBP4 antagonist prevents loops $\beta3-\beta4$ and $\beta5-\beta6$ to adopt favorable conformations that promote association with the PPI domain of TTR. The emerging RBP4−TTR HTRF SAR is also intriguing. Of the compounds tested in this assay, the two that were found to be the least potent (methylated analogue **20i** and tetrazole **54**) present either a steric blocking group ortho to or a bioisosteric replacement of the carboxylic acid of **14**. We plan to determine if **20i**, carboxamide **53**, and tetrazole **54** also induce a significant lowering of serum RBP4 in mice and we will generate additional amide analogues and isosteres of **53**, carboxylic acid isosteres of **14**, and analogues of **20i** featuring various blocking substituents beyond a methyl group to further probe TTR FP and RBP4−TTR HTRF SAR effects.

It may also be possible that in addition to binding at the T4 site, compound **14** may also be binding at another-to-be-determined site on TTR and/or RBP4 that results in antagonism of holo-RBP4−TTR complex formation. We plan to address questions concerning the putative mechanism of action for holo-RBP4−TTR complex disruption by **14** *via* conducting a series of studies designed to further elucidate the nature of the compound's mode(s) of binding. This includes the generation of an X-ray crystal structure of TTR cocrystallized with **14** to confirm that the compound is binding within the T4 site in the pose predicted by our docking model. Such data, coupled with saturation transfer difference (STD) nuclear magnetic resonance (NMR) experiments,[70] may also allow us to determine if **14** binding at the T4 site imparts conformational changes within the TTR hydrophobic patch and PPI domain that disfavor association with holo-RBP4. An X-ray crystal structure may also determine if **14** is binding at any other potential sites at TTR in addition to the T4 binding site. We also plan to conduct ITC studies with **14**. Generation of ITC data with **14** and TTR will help elucidate the relative magnitude of enthalpic and entropic contributions to binding for **14** relative to tafamidis and AG10, which could guide subsequent drug design campaigns for the series. Furthermore, we will also conduct ITC studies with **14** and RBP4 to probe whether the compound is potentially disrupting the holo-RBP4−TTR complex formation *via* binding to an allosteric site on the protein that overlaps with or is located separately from the all-*trans*-retinol orthosteric binding site. Such potential mechanisms of allosteric binding at RBP4 may not be detected with our RBP4 SPA binding assay if they do not disrupt all-*trans*-retinol binding.

In general, our current data proves that there is a very good PK−PD relationship between **14** exposure and serum RBP4-lowering activity in mice. In our previous work, we proved a direct correlation between serum RBP4-lowering induced by different classes of selective RBP4 antagonists and bisretinoid-lowering efficacy in the *Abca4*$^{-/-}$ mouse model of Stargardt disease.[9,10] Based on the very good *in vivo* RBP4-lowering activity exhibited by **14** and its bis-hydrochloride salt **14a**, it is expected that this compound will be efficacious in suppressing the formation of cytotoxic lipofuscin bisretinoids in the retina, and studies with the *Abca4*$^{-/-}$ mouse model are ongoing. The data presented herein justifies further evaluation of selective TTR ligands as a class of potential therapeutics for the treatment of Stargardt disease, dry AMD, and other conditions characterized by enhanced accumulation of lipofuscin in the retina.

■ CONCLUSIONS

Inherited Stargardt disease and dry AMD are the forms of macular degeneration that may potentially be treated by pharmacological inhibition of lipofuscin bisretinoid synthesis in the retina. Only one class of compounds, competitive antagonists of all-*trans*-retinol binding to RBP4, was currently known to block the all-*trans*-retinol-dependent RBP4−TTR interaction and reduce cytotoxic bisretinoid production in the animal models of excessive lipofuscin accumulation. However, the use of selective RBP4 antagonists may not be optimal in patients who, in addition to macular degeneration, may also be predisposed to genetic or sporadic forms of ATTR. The holo-RBP4−TTR interaction stabilizes a portion of TTR tetramers circulating in the bloodstream, thus preventing formation of TTR amyloid fibrils and ATTR. Selective RBP4 antagonists release the TTR tetramer from the serum holo-RBP4−TTR complex, and the release of a pool of unliganded TTR may be associated with destabilization of TTR tetramers. We hypothesized that ligands that selectively bind to TTR and not to RBP4 may also be capable of allosterically antagonizing all-*trans*-retinol-dependent RBP4−TTR ternary complex formation. Such selective TTR ligands may induce a desired partial reduction in serum RBP4 levels required for inhibition of lipofuscin bisretinoid synthesis in the retina while simultaneously providing adequate TTR tetramer kinetic stabilization. To the best of our knowledge, prior to the work reported herein, TTR had not been considered as a drug target for mechanisms or indications that may be treated *via* selective RBP4 antagonists. In the reported work, we sought to identify novel TTR tetramer kinetic stabilizers that may also demonstrate robust RBP4-lowering capability *in vivo*. We utilized a TTR computational docking model derived from reported X-ray crystallographic data (PDB 4HIQ) and SAR for clinically investigated AG10 to enable our structure-based drug design campaign. Our goal was to identify novel and conformationally constrained compounds that could provide favorable TTR tetramer kinetic stabilization. We initially prepared piperazine ring core linker congener **14**, which was found to exhibit excellent potency at TTR (TTR FP IC_{50} = 220 nM). Our computational docking model derived from PDB 4HIQ provided insights into the molecular determinants responsible for the high-affinity **14** exhibits toward the TTR. Follow-up analogues of **14** included a focused sample set containing alternately substituted benzoic acid appendages as well as analogues that explored SAR effects with alternative pyrazole head groups. Compound **14** emerged as a lead upon conclusion of our SAR and ADME profiling campaigns and was found to possess excellent PK characteristics in mouse. Analogue **14** significantly decreases the formation of TTR high-molecular-weight aggregates in a manner comparable to tafamidis in an *in vitro* TTR aggregation assay, proving its activity as a TTR kinetic stabilizer. Furthermore, the compound and its bis-hydrochloride salt induced robust and sustained lowering of serum RBP4 levels upon oral dosing in mice. As previously stated, it is currently unclear how the TTR kinetic stabilizers studied in this work are inhibiting RBP4−TTR−all-*trans*-retinol complex formation, and future studies will be conducted to help gain a better understanding of these observations. However, the current data suggests that they may be efficacious in suppressing the formation of cytotoxic lipofuscin bisretinoids in the retina while preventing possible TTR amyloid fibril formation. This justifies evaluation of selective TTR tetramer ligands as a class of

https://doi.org/10.1021/acs.jmedchem.1c00099
J. Med. Chem. 2021, 64, 9010−9041

potential therapeutics for Stargardt disease, dry AMD, and other conditions characterized by enhanced accumulation of lipofuscin in the retina, especially in patients who are also prone to ATTR comorbidities such as sporadic SSA or hereditary TTR amyloidosis. Studies with **14** in the *Abca4*$^{-/-}$ mouse model are ongoing, and the data will be reported in due course.

■ EXPERIMENTAL SECTION

Fluorescence Polarization TTR Tetramer Binding Assay. Binding potency (IC_{50} values) of novel compounds for unliganded TTR tetramers isolated from human plasma (Clabiochem-Millipore, cat. no. 52957) was measured using an established fluorescence polarization assay designed for TTR kinetic stabilizers.[41] The assay measured competitive displacement of a fluorescent probe (fluorescein isothiocyanate (FITC) coupled to a diclofenac analogue *via* a PEGylated linker) by a novel compound from TTR. The FITC probe was synthesized at LeadGen Labr, LLC, using the reported route by Alhamadsheh and co-workers.[41] Each well contained 200 nM of TTR and 100 nM of FITC probe in the FP buffer (10 mM Tris−HCl pH 7.5, 150 mM NaCl, 0.01% of 3-(3-cholamidopropyl)-dimethylammonio-1-propanesulfonate (CHAPS), 0.01% Prionex) along with test compounds. Nonspecific binding was determined in the presence of 500 μM unlabeled diclofenac (Sigma-Aldrich). Reactions with test compounds were incubated overnight at 4 °C, and FP was measured on a Spectramax M5e plate reader (Molecular Devices).

TTR Aggregation Assay. The ability of test compounds to prevent TTR aggregation was evaluated under the acidic conditions that favor TTR aggregation and fibril formation.[63,64] A 2 μL solution of 167 μM human TTR (ACRO Biosystems #H5223) was incubated with 7 μL of 50 mM sodium acetate (pH = 4.0) (Sigma-Aldrich # S7545), and 100 mM KCl (Sigma-Aldrich # S5405) in the presence or absence of 1 μL of TTR inhibitor for 72 h at 37 °C. At the end of the incubation, 3.5 μL of a 500 mM sodium phosphate (Sigma-Aldrich #S5136) buffer (pH = 8.0) was added to each sample for neutralization and 0.6 μL of 5% CHAPS (Sigma-Aldrich #C5070) as a detergent to prevent reassociation of protein. The cross-linking was performed by adding 1.5 μL of 5% glutaraldehyde solution (Sigma-Aldrich # G6257). After 4 min, the reaction was stopped by the addition of 2.5 μL of freshly made 5% sodium borohydride ($NaBH_4$). Samples were subjected to TTR Western blotting with prealbumin antibodies (1:500; Dako #A0002). Band intensity for TTR monomer and TTR aggregates was quantified from scanned images of the blots.

***In Vitro* Binding of Compounds to RBP4.** Compound binding to RBP4 was assessed in the radiometric scintillation proximity (SPA) assay that was previously described.[4−7] The assay measured competitive displacement of radiolabeled [^{3}H]-all-*trans*-retinol from native RBP4 purified from human urine (Fitzgerald, 30R-AR022L). The protein was biotinylated using the EZ-link Sulfo-NHS-LC-Biotinylation kit from ThermoFisher (Cat #21335) as recommended by the manufacturer. Binding assays were implemented in a final volume of 100 μL in SPA buffer (1× PBR, pH 7.4, 1 mM ethylenediaminetetraacetic acid (EDTA), 0.1% BRA, 0.5% CHAPS). The assay reaction included a radioligand, 10 nM [^{3}H]-all-*trans*-retinol (48.7 Ci/mmol; PerkinElmer, Waltham, MA), along with the 0.3 mg/well streptavidin-PVT beads (PerkinElmer, RPNQ0006) and 50 nM biotinylated human RBP4. Unlabeled retinol (Sigma-Aldrich, cat # 95144) at 20 μM was added to control wells to assess a nonspecific binding. Radioactivity counts were measured using CHAMELEON plate reader (Hidex Oy, Turku, Finland) after 16 h of incubation at rt with mild shaking.

Assessment of Antagonistic Activity in the HTRF RBP4−TTR Interaction Assay. The ability of analogues to act as antagonists of all-*trans*-retinol-dependent RBP4−TTR interaction was measured in the homogeneous time-resolved fluorescence (HTRF) assay. Untagged TTR (Calbiochem, cat # 529577) and maltose-binding protein-tagged RBP4 expressed in *Escherichia coli* were used in this assay. HTRF Cryptate labeling kit from CisBio (Cisbio, cat # 62EUSPEA, Bedford, MA) was used to label TTR with Eu^{3+} cryptate. The assay was performed in a final assay volume of 16 μL in the buffer that contained 10 mM Tris−HCl (pH = 7.5), 1 mM dithiothreitol (DTT), 0.05% NP-40, 0.05% Prionex, 6% glycerol, and 400 mM KF. Other components of the reaction mix included 60 nM of MBP-RBP4, 5 nM of TTR-Eu, 26.7 nM of anti-MBP antibody conjugated with d2 (Cisbio, cat # 61MBPDAA), and 1 μM of all-*trans*-retinol (Sigma-Aldrich, cat # 95144). All of the reactions were performed under dim red light in the dark. The plates were read in the SpectraMax M5e Multimode Plate Reader (Molecular Devices, Sunnyvale, CA) after the overnight incubation at 4 °C. Fluorescence was excited at 337 nm; emission was measured at 668 and 620 nm with a 75 μs counting delay. The HTRF signal was expressed as the ratio of fluorescence intensity: $Flu_{668}/Flu_{620} \times 10\,000$.

Animal Care and Use Statement. Information regarding *in vivo* experimental protocols is located within the Supporting Information section. All of the protocols used for the *in vivo* experiments disclosed are in compliance with the U.S. Department of Agriculture's (USDA) Animal Welfare Act (nine CFR parts 1−3); the Guide for the Care and Use of Laboratory Animals, Institute of Laboratory Animal Resources, National Academy Press, Washington, DC, 1996; and the National Institutes of Health, Office of Laboratory Animal Welfare. Whenever possible, procedures in this study are designed to avoid or minimize discomfort, distress, and pain to animals.

Docking Models. PDB structures were prepared for molecular docking experiments using the protein structural preparation tool followed by Protonate3D, as implemented in the Molecular Operating Environment (MOE) 2020.09 (Chemical Computing Group, Inc., Montreal, Quebec, Canada, http://www.chemcomp.com). Ligand structures were built with MOE and minimized using the MM-FF94x force field until a root-mean-square deviation (RMSD) gradient of 0.05 kcal/(mol Å) was reached. In the first step for protein preparation, we preprocessed the structure using the standard protocol, which included the assigning of bond orders, the adding of hydrogens, the creating of disulfide bonds, and the prediction of the structural protonation state at a physiological pH of 7.4. The structure was subjected to a short energy minimization routine to relax it using the Amber 99 force field as implemented in MOE. The following standard parameters were selected: receptor van der Waals scaling, 0.50; ligand van der Waals scaling, 0.50; and a maximum of 20 poses per ligand. The best docking pose for **14** was selected based on the lowest RMSD value, which was 1.7 Å.

General Chemistry. All reactions were performed under a dry atmosphere of nitrogen unless otherwise specified. Indicated reaction temperatures refer to the reaction bath, while room temperature (rt) is noted as 25 °C. Commercial-grade reagents and anhydrous solvents were used as received from vendors, and no attempts were made to purify or dry these components further. Removal of solvents under reduced pressure was accomplished with a Buchi rotary evaporator at approximately 28 mmHg pressure using a Teflon-linked KNF vacuum pump. The measurement of pH for neutralizations or acidifications was measured with Hydrion pH paper (MicroEssential Lab). Thin-layer chromatography (TLC) was performed using 1 in. × 3 in. Analtech no. 02521 silica gel plates with a fluorescent indicator. Visualization of TLC plates was made by observation with either short-wave UV light (254 nm lamp), 10% phosphomolybdic acid in ethanol, or in iodine vapors. Preparative thin-layer chromatography was performed using Analtech, 20 × 20 cm^2, 1000 μm preparative TLC plates. Flash column chromatography was carried out using a Teledyne Isco CombiFlash Companion Unit and a Biotage Selekt System with Teledyne Isco RediSep Rf and Biotage Sfär silica gel columns. If needed, products were purified by reverse-phase chromatography, using a Teledyne Isco CombiFlash Companion Unit and a Biotage Selekt System with a RediSep Gold C18 reverse-phase column. Proton NMR spectra were obtained on a 400 MHz Varian nuclear magnetic resonance spectrometer. Chemical shifts (δ) are reported in parts per million (ppm), and coupling constant (J) values are given in hertz, with the following spectral pattern designations: s, singlet; d, doublet; t, triplet, q, quartet; quint, quintet; m, multiplet; dd, doublet of doublets; dt, doublet of triplets; dq; doublet of quartets; br, broad signal. Tetramethylsilane was used as an internal reference. Peak listing,

https://doi.org/10.1021/acs.jmedchem.1c00099
J. Med. Chem. 2021, 64, 9010−9041

multiplicity designations, and coupling constant calculations were conducted using Mnova v.14 software (Mestrelab Research). Carbon NMR spectra were obtained on a 500 MHz Bruker AV III nuclear magnetic resonance spectrometer, and tetramethylsilane was used as an internal reference. Fluorine NMR spectra were obtained on a 400 MHz Bruker AV III nuclear magnetic resonance spectrometer. Any melting points provided are uncorrected and were obtained using a Stanford Research Systems OptiMelt melting point apparatus (MPA100) with an automated melting point system. Mass spectroscopic analyses were performed using electrospray ionization (ESI) on a Waters AQUITY UPLC MS triple quadrapole mass spectrometer. High-pressure liquid chromatography (HPLC) purity analysis was performed using a Waters Breeze2 HPLC system with binary solvent systems A and B using a gradient elusion [A, H_2O with 0.1% formic acid; B, CH_3CN with 0.1% formic acid] and flow rate = 0.5 mL/min, with UV detection at 254 nm (system equipped with a photodiode array (PDA) detector). An ACQUITY UPLC BEH C18 column, 130 Å, 1.7 μm, 2.1 mm × 50 mm, was used. High-resolution mass spectrometry (HRMS) analysis was performed using an Agilent 6530 Accurate-Mass Q-TOF. All final compounds tested for *in vitro* and *in vivo* biological testing were purified to ≥95% purity, and these purity levels were measured by both ^{1}H NMR and HPLC.

*3-(4-(3,5-Dimethyl-1H-pyrazol-4-yl)piperazin-1-yl)-4-fluorobenzoic Acid (**14**). Step A.* A mixture of *tert*-butyl piperazine-1-carboxylate (**15**, 2.00 g, 10.7 mmol) and methyl 3-bromo-4-fluorobenzoate (2.25 g, 9.65 mmol) in anhydrous 1,4-dioxane (50 mL) was degassed with N_2 for 5 min. Cs_2CO_3 (10.0 g, 30.6 mmol), X-Phos (0.600 g, 1.25 mmol), and $Pd_2(dba)_3{\cdot}CHCl_3$ (0.555 g, 0.536 mmol) were then added, and the mixture was stirred reflux for 16 h under an atmosphere of N_2. The mixture was allowed to cool to rt and then concentrated under reduced pressure. The resulting residue was chromatographed over silica gel (0−30% ethyl acetate (EtOAc) in hexanes) to give *tert*-butyl 4-(2-fluoro-5-(methoxycarbonyl)phenyl)piperazine-1-carboxylate (**16a**) as a brown oil (3.0 g, 83%). The material was used as is in the next step: ESI MS m/z 339 $[M + H]^+$.

Step B. To a 0 °C cooled solution of *tert*-butyl 4-(2-fluoro-5-(methoxycarbonyl)phenyl)piperazine-1-carboxylate (**16a**, 3.00 g, 8.87 mmol) in CH_2Cl_2 (30 mL) was added TFA (6.7 mL, 87.5 mmol), and the resulting solution was stirred at rt for 16 h while gradually warming to rt. The mixture was then concentrated under reduced pressure and diluted with H_2O (30 mL), basified with saturated aqueous $NaHCO_3$ solution (50 mL), and extracted with EtOAc (3 × 50 mL). The combined organic extracts were washed with brine (50 mL), dried over Na_2SO_4, filtered, and concentrated under reduced pressure. The crude material was triturated with Et_2O and filtered to give pure methyl 4-fluoro-3-(piperazin-1-yl)benzoate (**17a**) as a white solid (1.20 g, 57%): ^{1}H NMR (400 MHz, $CDCl_3$) δ 9.85 (br, 1H), 7.72−7.69 (m, 1H), 7.63−7.60 (m, 1H), 7.21−7.04 (m, 1H), 3.87 (s, 3H), 3.35 (s, 8H); ESI MS m/z 239 $[M + H]^+$.

Step C. To a 0 °C cooled solution of methyl 4-fluoro-3-(piperazin-1-yl)benzoate (**17a**, 1.20 g, 5.03 mmol) in anhydrous THF (10 mL) were added *i*-Pr_2NEt (0.9 mL, 5.16 mmol) and 3-chloropentane-2,4-dione (0.67 mL, 5.96 mmol) simultaneously, and the resulting solution was stirred for 16 h under a N_2 atmosphere while gradually warming to rt. The mixture was then diluted with H_2O (50 mL) and extracted with EtOAc (3 × 50 mL). The combined organic extracts were washed with brine, dried over Na_2SO_4, and concentrated under reduced pressure. The resulting residue was chromatographed over silica gel (0−50% EtOAc in hexanes) to give methyl 3-(4-(2,4-dioxopentan-3-yl)-piperazin-1-yl)-4-fluorobenzoate (**18a**) as a brown oil (0.600 g, 35%): ^{1}H NMR (400 MHz, $CDCl_3$) δ 7.64−7.62 (m, 2H), 7.06−7.01 (m, 1H), 3.86 (s, 1H), 3.31−3.09 (m, 4H), 3.09−3.05 (m, 4H), 2.27 (s, 1H), 2.24 (s, 6H); ESI MS m/z 337 $[M + H]^+$.

Step D. To a solution of methyl 3-(4-(2,4-dioxopentan-3-yl)-piperazin-1-yl)-4-fluorobenzoate (**18a**, 0.500 g, 1.48 mmol) in CH_3OH (10 mL) was added $N_2H_4{\cdot}H_2O$ (0.2 mL, 2.67 mmol, 64−65% solution in H_2O), and the resulting mixture was stirred at rt for 1 h. The mixture was then concentrated under reduced pressure, and the resulting residue was chromatographed over silica gel (0−50% EtOAc in hexanes) to give methyl 3-(4-(3,5-dimethyl-1*H*-pyrazol-4-yl)piperazin-1-yl)-4-fluorobenzoate (**19a**) as a brown solid (0.420 g, 85%): ^{1}H NMR (400 MHz, $CDCl_3$) δ 7.67−7.63 (m, 2H), 7.04−7.01 (m, 1H), 3.86 (s, 1H), 3.16−3.15 (m, 4H), 3.15−3.11 (m, 4H), 2.24 (s, 6H); ESI MS m/z 333 $[M + H]^+$.

Step E. To a solution of methyl 3-(4-(3,5-dimethyl-1*H*-pyrazol-4-yl)piperazin-1-yl)-4-fluorobenzoate (**19a**, 0.420 g, 1.26 mmol) in CH_3OH (4 mL), THF (4 mL), and H_2O (2 mL) was added anhydrous LiOH (91 mg, 3.79 mmol). The reaction mixture was stirred at rt for 16 h and concentrated under reduced pressure. The aqueous layer was then diluted with H_2O (30 mL) and neutralized to approximately pH = 7 with 2 N aqueous HCl (monitored with Hydrion pH paper). The aqueous mixture was extracted with EtOAc (3 × 50 mL), and the combined organic solution was washed with brine, dried over Na_2SO_4, and concentrated under reduced pressure. The crude residue was chromatographed over silica gel (0−10% CH_3OH in CH_2Cl_2) to give 3-(4-(3,5-dimethyl-1*H*-pyrazol-4-yl)piperazin-1-yl)-4-fluorobenzoic acid (**14**) as a white solid (0.390 g, 97%): melting point = 220−222 °C; ^{1}H NMR (400 MHz, DMSO-d_6) δ 7.53−7.55 (m, 2H, H_1 and H_2), 7.23−7.18 (dt, J = 12, 3.2 Hz, 1H, H_3), 3.04 (m, 4H, H_4), 3.01 (m, 4H, H_5), 2.10 (s, 6H, H_6); ^{13}C NMR (500 MHz, DMSO-d_6) δ 128.7, 121.7, 124.1, 124.0, 120.2, 120.2, 116.3, 116.2; ^{19}F NMR (400 MHz, DMSO-d_6) δ −116.0 (s, F); ESI MS m/z 319 $[M + H]^+$; HRMS (ESI$^+$) $C_{16}H_{19}FN_4O_2$ calcd $[M + H]^+$ = 319.1565, observed $[M + H]^+$ = 319.1562; combustion analysis (%C, H, N): calcd for $C_{16}H_{19}FN_4O_2{\cdot}0.5H_2O{\cdot}0.5HCl$: %C = 55.61; %H = 5.98; %N = 16.21; found: %C = 55.88; %H = 5.74; %N = 15.97; HPLC >99% (AUC), t_R = 11.5 min.

*3-(4-(3,5-Dimethyl-1H-pyrazol-4-yl)piperazin-1-yl)-4-fluorobenzoic Acid Bis-hydrochloride (**14a**). Step A.* To a solution of 3-(4-(3,5-dimethyl-1*H*-pyrazol-4-yl)piperazin-1-yl)-4-fluorobenzoic acid (**14**, 0.700 g, 2.20 mmol) in anhydrous Et_2O (5 mL) at 0 °C was slowly added a 2 N HCl solution in Et_2O dropwise (11.0 mL, 22.0 mmol), and the pH of the mixture was observed at approximately pH = 2 (monitored with Hydrion pH paper). The mixture was then stirred at rt for 3 h, and the Et_2O was removed under reduced pressure. The resulting material was triturated with Et_2O and dried under reduced pressure to give 3-(4-(3,5-dimethyl-1*H*-pyrazol-4-yl)piperazin-1-yl)-4-fluorobenzoic acid bis-hydrochloride (**14a**) as a white solid (0.800 g, 93%): ^{1}H NMR (400 MHz, DMSO-d_6) δ 7.63 (m, 2H), 7.29 (dt, J = 8.8 Hz, 3.2 Hz, 1H), 3.26 (m, 8H), 2.39 (s, 6H); ^{13}C NMR (500 MHz, DMSO-d_6) δ 167.0, 159.1, 157.1, 140.0, 139.2, 128.1, 124.8, 120.8, 116.9, 52.2, 50.0, 10.8; ESI MS m/z 319 $[M + H]^+$; HRMS (ESI$^+$) $C_{16}H_{19}FN_4O_2$ calcd $[M + H]^+$ = 319.1565, observed $[M + H]^+$ = 319.1561; combustion analysis (%C, H, N, Cl): calcd for $C_{16}H_{19}FN_4O_2{\cdot}1.2H_2O{\cdot}2.0HCl$: %C = 46.54; %H = 5.71; %N = 13.57; %Cl = 17.17; found: %C = 46.57; %H = 5.52; %N = 13.39; %Cl = 16.97; HPLC >99% (AUC), t_R = 11.4 min.

*3-(4-(3,5-Dimethyl-1H-pyrazol-4-yl)piperazin-1-yl)benzoic Acid (**20a**). Step A.* A mixture of *tert*-butyl piperazine-1-carboxylate (**15**, 3.46 g, 18.5 mmol) and methyl 3-bromobenzoate (2.0 g, 9.30 mmol) in anhydrous 1,4-dioxane (50 mL) was degassed with N_2 for 5 min. Cs_2CO_3 (1.04 g, 3.19 mmol), X-Phos (0.600 g, 1.25 mmol), and $Pd_2(dba)_3{\cdot}CHCl_3$ (0.621 g, 0.600 mmol) were then added, and the mixture was stirred in a sealed tube at 110 °C for 16 h. The mixture was allowed to cool to rt and then concentrated under reduced pressure. The resulting residue was chromatographed over silica gel (0−20% EtOAc in hexanes) to give *tert*-butyl 4-(3-(methoxycarbonyl)phenyl)-piperazine-1-carboxylate (**16b**) as a brown solid (0.440 g, 14%). The material was used as is in the next step: ESI MS m/z 321 $[M + H]^+$.

Step B. To a 0 °C cooled solution of *tert*-butyl 4-(3-(methoxycarbonyl)phenyl)piperazine-1-carboxylate (**16b**, 0.430 g, 1.34 mmol) in CH_2Cl_2 (30 mL) was added TFA (3.0 mL, 39.2 mmol), and the resulting solution was stirred at rt for 16 h while gradually warming to rt. The mixture was then concentrated under reduced pressure and diluted with H_2O (30 mL), basified with saturated aqueous $NaHCO_3$ solution (50 mL), and extracted with EtOAc (3 × 50 mL). The combined organic extracts were washed with brine (50 mL), dried over Na_2SO_4, filtered, and concentrated under reduced pressure to give crude methyl 3-(piperazin-1-yl)benzoate (**17b**) as a white solid (0.292 g, >99%, crude): ESI MS m/z 221 $[M + H]^+$.

https://doi.org/10.1021/acs.jmedchem.1c00099
J. Med. Chem. 2021, 64, 9010−9041

Step C. To a 0 °C cooled solution of methyl 3-(piperazin-1-yl)benzoate (**17b**, 0.290 g, 1.32 mmol) in anhydrous THF (5 mL) were added *i*-Pr_2NEt (1.2 mL, 6.88 mmol) and 3-chloropentane-2,4-dione (0.44 mL, 3.90 mmol) simultaneously, and the resulting solution was stirred for 16 h under a N_2 atmosphere while gradually warming to rt. Upon *in situ* formation of methyl 3-(4-(2,4-dioxopentan-3-yl)-piperazin-1-yl)benzoate (**18b**) (monitored by liquid chromatography-mass spectrometry (LC-MS); ESI MS *m/z* 319 [M + H]$^+$), $N_2H_4 \cdot H_2O$ (0.26 mL, 3.15 mmol, 64−65% solution in H_2O) was then added, and the mixture was continued to stir at rt for an additional 1 h. The mixture was then diluted with H_2O (50 mL) and extracted with EtOAc (3 × 50 mL). The combined organic extracts were washed with brine, dried over Na_2SO_4, filtered, and concentrated under reduced pressure. The resulting crude residue was chromatographed over silica gel (0−10% CH_3OH in CH_2Cl_2) to give methyl 3-(4-(3,5-dimethyl-1*H*-pyrazol-4-yl)piperazin-1-yl)benzoate as a brown solid (**19b**) along with an inseparable and uncharacterized impurity (0.280 g, 67%, impure): ESI MS *m/z* 315 [M + H]$^+$.

Step D. To a solution of methyl 3-(4-(3,5-dimethyl-1*H*-pyrazol-4-yl)piperazin-1-yl)benzoate (**19b**, 0.130 g, 0.413 mmol) in CH_3OH (4 mL), THF (4 mL), and H_2O (2 mL) was added anhydrous LiOH (49.5 mg, 2.06 mmol). The reaction mixture was stirred at rt for 3 h and concentrated under reduced pressure. The aqueous layer was then diluted with H_2O (30 mL) and neutralized to approximately pH = 7 with 2 N aqueous HCl (monitored with Hydrion pH paper). The aqueous mixture was extracted with EtOAc (3 × 50 mL), and the combined organic solution was washed with brine, dried over Na_2SO_4, and concentrated under reduced pressure. The crude residue was chromatographed over silica gel (0−10% CH_3OH in CH_2Cl_2) to give 3-(4-(3,5-dimethyl-1*H*-pyrazol-4-yl)piperazin-1-yl)benzoic acid (**20a**) as a white solid (7.8 mg, 6.2%): ^{1}H NMR (400 MHz, DMSO-d_6) δ 7.48 (s, 1H), 7.36 (m, 2H), 7.23 (m, 1H), 3.23 (m, 4H), 3.04 (m, 4H), 2.14 (s, 6H); ESI MS *m/z* 301 [M + H]$^+$; HPLC >99% (AUC), t_R = 10.7 min.

*3-(4-(3,5-Dimethyl-1H-pyrazol-4-yl)piperazin-1-yl)-4-methoxybenzoic Acid (**20b**). Step A.* A mixture of *tert*-butyl piperazine-1-carboxylate (**15**, 0.911 g, 4.89 mmol) and methyl 3-bromo-4-methoxybenzoate (1.0 g, 4.08 mmol) in anhydrous 1,4-dioxane (50 mL) was degassed with N_2 for 5 min. Cs_2CO_3 (2.6 g, 7.97 mmol), X-Phos (0.230 g, 0.482 mmol), and $Pd_2(dba)_3 \cdot CHCl_3$ (0.124 g, 0.120 mmol) were then added, and the mixture was stirred in a sealed tube at 110 °C for 16 h. The mixture was allowed to cool to rt and then concentrated under reduced pressure. The resulting residue was chromatographed over silica gel (0−30% EtOAc in hexanes) to give *tert*-butyl 4-(2-methoxy-5-(methoxycarbonyl)phenyl)piperazine-1-carboxylate (**16c**) as a light yellow solid (1.40 g, 98%): ^{1}H NMR (400 MHz, acetone-d_6) δ 7.68 (d, *J* = 8.0 Hz, 1H), 7.51 (s, 1H), 7.04 (d, *J* = 8.4 Hz, 1H), 3.93 (s, 3H), 3.82 (s, 3H), 3.53 (brs, 4 h), 2.98 (brs, 4 h), 1.41 (s, 9H): ESI MS *m/z* 351 [M + H]$^+$.

Step B. To a 0 °C cooled solution of *tert*-butyl 4-(2-methoxy-5-(methoxycarbonyl)phenyl)piperazine-1-carboxylate (**16c**, 1.4 g, 3.99 mmol) in CH_2Cl_2 (30 mL) was added TFA (5.0 mL, 65.33 mmol), and the resulting solution was stirred at rt for 3 h while gradually warming to rt. The mixture was then concentrated under reduced pressure and diluted with H_2O (30 mL), basified with saturated aqueous $NaHCO_3$ solution (50 mL), and extracted with EtOAc (3 × 50 mL). The combined organic extracts were washed with brine (50 mL), dried over Na_2SO_4, filtered, and concentrated under reduced pressure to give crude methyl 4-methoxy-3-(piperazin-1-yl)benzoate (**17c**) as a brown oil (0.650 g, 65%, crude): ESI MS *m/z* 251 [M + H]$^+$.

Step C. To a 0 °C cooled solution of methyl 4-methoxy-3-(piperazin-1-yl)benzoate (**17c**, 0.650 g, 2.59 mmol) in anhydrous THF (10 mL) were added *i*-Pr_2NEt (1.4 mL, 8.03 mmol) and 3-chloropentane-2,4-dione (0.6 mL, 5.32 mmol) simultaneously, and the resulting solution was stirred for 16 h under a N_2 atmosphere while gradually warming to rt. Upon *in situ* formation of **18c** (monitored by LC-MS; ESI MS *m/z* 349 [M + H]$^+$), $N_2H_4 \cdot H_2O$ (0.26 mL, 3.15 mmol, 64−65% solution in H_2O) was then added and the mixture was continued to stir at rt for an additional 1 h. The mixture was then diluted with H_2O (50 mL) and extracted with EtOAc (3 × 50 mL). The combined organic extracts were washed with brine, dried over Na_2SO_4, filtered, and concentrated under reduced pressure. The resulting crude residue was chromatographed over silica gel (0−10% CH_3OH in CH_2Cl_2) to give methyl 3-(4-(3,5-dimethyl-1*H*-pyrazol-4-yl)piperazin-1-yl)-4-methoxybenzoate (**19c**) along with an inseparable and uncharacterized impurity (0.100 g, 11%, crude): ESI MS *m/z* 345 [M + H]$^+$.

Step D. To a solution of methyl 3-(4-(3,5-dimethyl-1*H*-pyrazol-4-yl)piperazin-1-yl)-4-methoxybenzoate (**19c**, 0.100 g, 0.290 mmol) in CH_3OH (4 mL), THF (4 mL), and H_2O (2 mL) was added anhydrous LiOH (34.0 mg, 1.41 mmol). The reaction mixture was stirred at rt for 3 h and concentrated under reduced pressure. The aqueous layer was then diluted with H_2O (30 mL) and neutralized to approximately pH = 7 with 2 N aqueous HCl (monitored with Hydrion pH paper). The aqueous mixture was extracted with EtOAc (3 × 50 mL), and the combined organic solution was washed with brine, dried over Na_2SO_4, and concentrated under reduced pressure. The crude residue was chromatographed over silica gel (0−10% CH_3OH in CH_2Cl_2) to give 3-(4-(3,5-dimethyl-1*H*-pyrazol-4-yl)piperazin-1-yl)-4-methoxybenzoic acid (**20b**) as a white solid (38.0 mg, 39%): ^{1}H NMR (400 MHz, DMSO-d_6) δ 7.58 (dd, *J* = 8.4 Hz, 2.0 Hz, 1H), 7.44 (d, *J* = 2.0 Hz, 1H), 7.01 (d, *J* = 8.4 Hz, 1H), 3.83 (s, 3H), 2.99 (s, 8H), 2.08 (s, 6H); ESI MS *m/z* 331 [M + H]$^+$; HPLC 94.6% (AUC), t_R = 10.2 min.

*3-(4-(3,5-Dimethyl-1H-pyrazol-4-yl)piperazin-1-yl)-4-methylbenzoic Acid (**20c**). Step A.* A mixture of *tert*-butyl piperazine-1-carboxylate (**15**, 0.978 g, 5.26 mmol) and methyl 3-bromo-4-methylbenzoate (1.0 g, 4.36 mmol) in anhydrous 1,4-dioxane (50 mL) was degassed with N_2 for 5 min. Cs_2CO_3 (2.8 g, 8.59 mmol), X-Phos (0.248 g, 0.520 mmol), and $Pd_2(dba)_3 \cdot CHCl_3$ (0.136 g, 0.131 mmol) were then added, and the mixture was stirred in a sealed tube at 110 °C for 16 h. The mixture was allowed to cool to rt and then concentrated under reduced pressure. The resulting residue was chromatographed over silica gel (0−30% EtOAc in hexanes) to give *tert*-butyl 4-(5-(methoxycarbonyl)-2-methylphenyl)piperazine-1-carboxylate (**16d**) as a brown solid (0.600 g, 41%). The material was used as is in the next step: ESI MS *m/z* 335 [M + H]$^+$.

Step B. To a 0 °C cooled solution of *tert*-butyl 4-(5-(methoxycarbonyl)-2-methylphenyl)piperazine-1-carboxylate (**16d**, 0.600 g, 1.79 mmol) in CH_2Cl_2 (30 mL) was added TFA (5.0 mL, 65.3 mmol), and the resulting solution was stirred at rt for 3 h while gradually warming to rt. The mixture was then concentrated under reduced pressure and diluted with H_2O (30 mL), basified with saturated aqueous $NaHCO_3$ solution (50 mL), and extracted with EtOAc (3 × 50 mL). The combined organic extracts were washed with brine (50 mL), dried over Na_2SO_4, filtered, and concentrated under reduced pressure. The crude material was triturated with Et_2O and filtered to give pure methyl 4-methyl-3-(piperazin-1-yl)benzoate (**17d**) as a white solid (0.300 g, 71%, crude): ESI MS *m/z* 235 [M + H]$^+$.

Step C. To a 0 °C cooled solution of methyl 4-methyl-3-(piperazin-1-yl)benzoate (**17d**, 0.300 g, 1.28 mmol) in anhydrous THF (10 mL) were added *i*-Pr_2NEt (0.74 mL, 4.24 mmol) and 3-chloropentane-2,4-dione (0.30 mL, 2.66 mmol) simultaneously, and the resulting solution was stirred for 16 h under a N_2 atmosphere while gradually warming to rt. Upon *in situ* formation of **18d** (monitored by LC-MS; ESI MS *m/z* 333 [M + H]$^+$), $N_2H_4 \cdot H_2O$ (0.14 mL, 1.68 mmol, 64−65% solution in H_2O) was then added, and the mixture was continued to stir at rt for an additional 1 h. The mixture was then diluted with H_2O (50 mL) and extracted with EtOAc (3 × 50 mL). The combined organic extracts were washed with brine, dried over Na_2SO_4, filtered, and concentrated under reduced pressure. The resulting crude residue was chromatographed over silica gel (0−10% CH_3OH in CH_2Cl_2) to give methyl 3-(4-(3,5-dimethyl-1*H*-pyrazol-4-yl)piperazin-1-yl)-4-methylbenzoate (**19d**) as a brown oil along with an inseparable and uncharacterized impurity (0.100 g, 23%, crude): ESI MS *m/z* 329 [M + H]$^+$.

Step D. To a solution of methyl 3-(4-(3,5-dimethyl-1*H*-pyrazol-4-yl)piperazin-1-yl)-4-methylbenzoate (**19d**, 0.100 g, 0.304 mmol) in CH_3OH (4 mL), THF (4 mL), and H_2O (2 mL) was added anhydrous LiOH (24.0 mg, 1.00 mmol). The reaction mixture was stirred at rt for 3 h and concentrated under reduced pressure. The aqueous layer was then diluted with H_2O (30 mL) and neutralized to approximately pH = 7 with 2 N aqueous HCl (monitored with Hydrion pH paper). The aqueous mixture was extracted with EtOAc (3 × 50 mL), and the

https://doi.org/10.1021/acs.jmedchem.1c00099
J. Med. Chem. 2021, 64, 9010−9041

combined organic solution was washed with brine, dried over Na_2SO_4, and concentrated under reduced pressure. The crude residue was chromatographed over silica gel (0−10% CH_3OH in CH_2Cl_2) to give 3-(4-(3,5-dimethyl-1*H*-pyrazol-4-yl)piperazin-1-yl)-4-methylbenzoic acid (**20c**) as a white solid (31.0 mg, 32%): ^{1}H NMR (400 MHz, DMSO-d_6) δ 7.57 (d, J = 1.2 Hz, 1H), 7.53 (d, J = 8.0 Hz, 1H), 7.27 (d, J = 8.0 Hz, 1H), 3.01 (m, 4H), 2.90 (m, 4H), 2.46 (s, 3H), 2.12 (s, 6H); ESI MS m/z 315 [M + H]$^+$; HPLC >99% (AUC), t_R = 11.2 min.

*3-(4-(3,5-Dimethyl-1H-pyrazol-4-yl)piperazin-1-yl)-4-(trifluoromethyl)benzoic Acid (**20d**). Step A.* A mixture of *tert*-butyl piperazine-1-carboxylate (**15**, 0.700 g, 3.75 mmol) and methyl 3-bromo-4-(trifluoromethyl)benzoate (0.957 g, 3.38 mmol) in anhydrous 1,4-dioxane (50 mL) was degassed with N_2 for 5 min. Cs_2CO_3 (3.6 g, 11.04 mmol), X-Phos (0.212 g, 0.444 mmol), and $Pd_2(dba)_3$·$CHCl_3$ (0.192 g, 0.186 mmol) were then added, and the mixture was stirred in a sealed tube at 110 °C for 16 h. The mixture was allowed to cool to rt and then concentrated under reduced pressure. The resulting residue was chromatographed over silica gel (0−30% EtOAc in hexanes) to give *tert*-butyl 4-(5-(methoxycarbonyl)-2-(trifluoromethyl)phenyl)piperazine-1-carboxylate (**16e**) as a brown oil (0.450 g, 31%). The material was used as is in the next step: ESI MS m/z 389 [M + H]$^+$.

Step B. To a 0 °C cooled solution of *tert*-butyl 4-(5-(methoxycarbonyl)-2-(trifluoromethyl)phenyl)piperazine-1-carboxylate (**16e**, 0.450 g, 1.15 mmol) in CH_2Cl_2 (30 mL) was added TFA (3.0 mL, 39.2 mmol), and the resulting solution was stirred at rt for 3 h while gradually warming to rt. The mixture was then concentrated under reduced pressure and diluted with H_2O (30 mL), basified with saturated aqueous $NaHCO_3$ solution (50 mL), and extracted with EtOAc (3 × 50 mL). The combined organic extracts were washed with brine (50 mL), dried over Na_2SO_4, filtered, and concentrated under reduced pressure. The crude material was triturated with Et_2O and filtered to give pure methyl 3-(piperazin-1-yl)-4-(trifluoromethyl)-benzoate (**17e**) as a white solid (0.350 g, >99%, crude): ESI MS m/z 289 [M + H]$^+$.

Step C. To a 0 °C cooled solution of methyl 3-(piperazin-1-yl)-4-(trifluoromethyl)benzoate (**17e**, 0.350 g, 1.21 mmol) in anhydrous THF (10 mL) were added *i*-Pr_2NEt (1.0 mL, 5.74 mmol) and 3-chloropentane-2,4-dione (0.40 mL, 3.54 mmol) simultaneously, and the resulting solution was stirred for 16 h under a N_2 atmosphere while gradually warming to rt. Upon *in situ* formation of **18e** (monitored by LC-MS; ESI MS m/z 387 [M + H]$^+$), N_2H_4·H_2O (0.20 mL, 1.82 mmol, 64−65% solution in H_2O) was then added and the mixture was continued to stir at rt for an additional 1 h. The mixture was then diluted with H_2O (50 mL) and extracted with EtOAc (3 × 50 mL). The combined organic extracts were washed with brine, dried over Na_2SO_4, filtered, and concentrated under reduced pressure. The resulting crude residue was chromatographed over silica gel (0−10% CH_3OH in CH_2Cl_2) to give methyl 3-(4-(3,5-dimethyl-1*H*-pyrazol-4-yl)piperazin-1-yl)-4-(trifluoromethyl)benzoate (**19e**) as a brown oil (0.150 g, 32%): ESI MS m/z 383 [M + H]$^+$.

Step D. To a solution of methyl 3-(4-(3,5-dimethyl-1*H*-pyrazol-4-yl)piperazin-1-yl)-4-(trifluoromethyl)benzoate (**19e**, 0.130 g, 0.34 mmol) in CH_3OH (4 mL), THF (4 mL), and H_2O (2 mL) was added anhydrous LiOH (81 mg, 3.38 mmol). The reaction mixture was stirred at rt for 3 h and concentrated under reduced pressure. The aqueous layer was then diluted with H_2O (30 mL) and neutralized to approximately pH = 7 with 2 N aqueous HCl (monitored with Hydrion pH paper). The aqueous mixture was extracted with EtOAc (3 × 50 mL), and the combined organic solution was washed with brine, dried over Na_2SO_4, and concentrated under reduced pressure. The crude residue was chromatographed over silica gel (0−10% CH_3OH in CH_2Cl_2) to give 3-(4-(3,5-dimethyl-1*H*-pyrazol-4-yl)piperazin-1-yl)-4-(trifluoromethyl)benzoic acid (**20d**) as an amorphous white solid (79.0 mg, 63%): ^{1}H NMR (400 MHz, DMSO-d_6) δ 7.99 (s, 1H), 7.84 (d, J = 8.4 Hz, 1H), 7.78 (d, J = 8.4 Hz, 1H), 2.97 (m, 4H), 2.94 (m, 4H), 2.11 (s, 6H); ESI MS m/z 369 [M + H]$^+$; HPLC 98.7% (AUC), t_R = 11.9 min.

*4-Chloro-3-(4-(3,5-dimethyl-1H-pyrazol-4-yl)piperazin-1-yl)-benzoic Acid (**20e**). Step A.* A mixture of *tert*-butyl piperazine-1-carboxylate (**15**, 0.700 g, 3.75 mmol) and methyl 3-bromo-4-chlorobenzoate (0.844 g, 3.38 mmol) in anhydrous 1,4-dioxane (50 mL) was degassed with N_2 for 5 min. Cs_2CO_3 (3.6 g, 11.04 mmol), X-Phos (0.212 g, 0.44 mmol), and $Pd_2(dba)_3$·$CHCl_3$ (0.192 g, 0.186 mmol) were then added, and the mixture was stirred in a sealed tube at 110 °C for 16 h. The mixture was allowed to cool to rt and then concentrated under reduced pressure. The resulting residue was chromatographed over silica gel (0−30% EtOAc in hexanes) to give *tert*-butyl 4-(2-chloro-5-(methoxycarbonyl)phenyl)piperazine-1-carboxylate (**16f**) as a yellow oil (0.800 g, 60%): ^{1}H NMR (400 MHz, acetone-d_6) δ 7.71 (s, 1H), 7.68−7.66 (m, 1H), 7.54 (d, J = 8.0 Hz, 1H), 3.88 (s, 3H), 3.58 (brs, 4H), 3.02 (brs, 4H), 1.46 (s, 9H); ESI MS m/z 355 [M + H]$^+$.

Step B. To a 0 °C cooled solution of *tert*-butyl 4-(2-chloro-5-(methoxycarbonyl)phenyl)piperazine-1-carboxylate (**16f**, 0.700 g, 1.97 mmol) in CH_2Cl_2 (30 mL) was added TFA (5.0 mL, 65.33 mmol), and the resulting solution was stirred at rt for 16 h while gradually warming to rt. The mixture was then concentrated under reduced pressure and diluted with H_2O (30 mL), basified with saturated aqueous $NaHCO_3$ solution (50 mL), and extracted with EtOAc (3 × 50 mL). The combined organic extracts were washed with brine (50 mL), dried over Na_2SO_4, filtered, and concentrated under reduced pressure. The crude material was triturated with Et_2O and filtered to give pure methyl 4-chloro-3-(piperazin-1-yl)benzoate (**17f**) as a white solid (0.450 g, 89%, crude): ESI MS m/z 255 [M + H]$^+$.

Step C. To a 0 °C cooled solution of methyl 4-chloro-3-(piperazin-1-yl)benzoate (**17f**, 0.200 g, 0.787 mmol) in anhydrous THF (10 mL) were added *i*-Pr_2NEt (0.7 mL, 4.01 mmol) and 3-chloropentane-2,4-dione (0.26 mL, 2.38 mmol) simultaneously, and the resulting solution was stirred for 16 h under a N_2 atmosphere while gradually warming to rt. Upon *in situ* formation of **18f** (monitored by LC-MS; ESI MS m/z 353 [M + H]$^+$), N_2H_4·H_2O (0.1 mL, 1.18 mmol, 64−65% solution in H_2O) was then added and the mixture was continued to stir at rt for an additional 1 h. The mixture was then diluted with H_2O (50 mL) and extracted with EtOAc (3 × 50 mL). The combined organic extracts were washed with brine, dried over Na_2SO_4, filtered, and concentrated under reduced pressure. The resulting crude residue was chromatographed over silica gel (0−10% CH_3OH in CH_2Cl_2) to give methyl 4-chloro-3-(4-(3,5-dimethyl-1*H*-pyrazol-4-yl)piperazin-1-yl)benzoate (**19f**) as a brown oil (80.0 mg, 29%): ESI MS m/z 349 [M + H]$^+$.

Step D. To a solution of methyl 4-chloro-3-(4-(3,5-dimethyl-1*H*-pyrazol-4-yl)piperazin-1-yl)benzoate (**19f**, 80.0 mg, 0.23 mmol) in CH_3OH (4 mL), THF (4 mL), and H_2O (2 mL) was added anhydrous LiOH (55.0 mg, 2.29 mmol). The reaction mixture was stirred at rt for 3 h and concentrated under reduced pressure. The aqueous layer was then diluted with H_2O (30 mL) and neutralized to approximately pH = 7 with 2 N aqueous HCl (monitored with Hydrion pH paper). The aqueous mixture was extracted with EtOAc (3 × 50 mL), and the combined organic solution was washed with brine, dried over Na_2SO_4, and concentrated under reduced pressure. The crude residue was chromatographed over silica gel (0−10% CH_3OH in CH_2Cl_2) to give 4-chloro-3-(4-(3,5-dimethyl-1*H*-pyrazol-4-yl)piperazin-1-yl)benzoic acid (**20e**) as an amorphous white solid (30.0 mg, 39%): ^{1}H NMR (400 MHz, DMSO-d_6) δ 7.66 (s, 1H), 7.58 (d, J = 8.4 Hz, 1H), 7.51 (d, J = 10.8 Hz, 1H), 3.04 (brs, 8H), 2.12 (s, 6H); ESI MS m/z 335 [M + H]$^+$; HPLC 98.0% (AUC), t_R = 11.5 min.

*3-(4-(3,5-Dimethyl-1H-pyrazol-4-yl)piperazin-1-yl)-2-fluorobenzoic Acid (**20f**). Step A.* A mixture of *tert*-butyl piperazine-1-carboxylate (**15**, 0.700 g, 3.75 mmol) and methyl 3-bromo-2-fluorobenzoate (0.787 g, 3.38 mmol) in anhydrous 1,4-dioxane (50 mL) was degassed with N_2 for 5 min. Cs_2CO_3 (3.6 g, 11.04 mmol), X-Phos (0.212 g, 0.444 mmol), and $Pd_2(dba)_3$·$CHCl_3$ (0.192 g, 0.186 mmol) were then added, and the mixture was stirred in a sealed tube at 110 °C for 16 h. The mixture was allowed to cool to rt and then concentrated under reduced pressure. The resulting residue was chromatographed over silica gel (0−30% EtOAc in hexanes) to give *tert*-butyl 4-(2-fluoro-3-(methoxycarbonyl)-phenyl)piperazine-1-carboxylate (**16g**) as a yellow oil (1.0 g, 78%): ^{1}H NMR (400 MHz, acetone-d_6) δ 7.47−7.45 (m, 1H), 7.31−7.27 (m, 1H), 7.19 (t, J = 8.0 Hz, 1H), 3.87 (s, 3H), 3.56 (brs, 4H), 3.02 (brs, 4H), 1.45 (s, 9H); ESI MS m/z 339 [M + H]$^+$.

https://doi.org/10.1021/acs.jmedchem.1c00099
J. Med. Chem. 2021, 64, 9010−9041

Step B. To a 0 °C cooled solution of *tert*-butyl 4-(2-fluoro-3-(methoxycarbonyl)phenyl)piperazine-1-carboxylate (**16g**, 1.0 g, 2.95 mmol) in CH_2Cl_2 (30 mL) was added TFA (5.0 mL, 65.33 mmol), and the resulting solution was stirred at rt for 3 h while gradually warming to rt. The mixture was then concentrated under reduced pressure and diluted with H_2O (30 mL), basified with saturated aqueous $NaHCO_3$ solution (50 mL), and extracted with EtOAc (3 × 50 mL). The combined organic extracts were washed with brine (50 mL), dried over Na_2SO_4, filtered, and concentrated under reduced pressure. The crude material was triturated with Et_2O and filtered to give pure methyl 2-fluoro-3-(piperazin-1-yl)benzoate (**17g**) as a brown oil (0.600 g, 85%, crude): ESI MS *m/z* 239 $[M + H]^+$.

Step C. To a 0 °C cooled solution of methyl 2-fluoro-3-(piperazin-1-yl)benzoate (**17g**, 300 mg, 1.26 mmol) in anhydrous THF (3 mL) were added *i*-Pr_2NEt (0.5 mL, 2.52 mmol) and 3-chloropentane-2,4-dione (0.3 mL, 2.52 mmol) simultaneously, and the resulting solution was stirred for 16 h under a N_2 atmosphere while gradually warming to rt. Upon *in situ* formation of **18g** (monitored by LC-MS; ESI MS *m/z* 337 $[M + H]^+$), $N_2H_4{\cdot}H_2O$ (0.16 mL, 1.89 mmol, 64−65% solution in H_2O) was then added and the mixture was continued to stir at rt for an additional 1 h. The mixture was then diluted with H_2O (50 mL) and extracted with EtOAc (3 × 50 mL). The combined organic extracts were washed with brine, dried over Na_2SO_4, filtered, and concentrated under reduced pressure. The resulting crude residue was chromatographed over silica gel (0−10% CH_3OH in CH_2Cl_2) to give methyl 3-(4-(3,5-dimethyl-1*H*-pyrazol-4-yl)piperazin-1-yl)-2-fluorobenzoate (**19g**) as a brown oil (0.160 g, 38%): ^1H NMR (400 MHz, DMSO-d_6) δ 11.79 (brs, 1H), 7.40−7.36 (m, 1H), 7.32−7.28 (m, 1H), 7.21−7.17 (m, 1H), 3.81 (s, 3H), 3.05−3.00 (m, 8H), 2.11 (s, 6H); ESI MS *m/z* 333 $[M + H]^+$.

Step D. To a solution of methyl 3-(4-(3,5-dimethyl-1*H*-pyrazol-4-yl)piperazin-1-yl)-2-fluorobenzoate (**19g**, 0.150 g, 0.451 mmol) in CH_3OH (4 mL), THF (4 mL), and H_2O (2 mL) was added anhydrous LiOH (0.108 g, 4.50 mmol). The reaction mixture was stirred at rt for 16 h and concentrated under reduced pressure. The aqueous layer was then diluted with H_2O (30 mL) and neutralized to approximately pH = 7 with 2 N aqueous HCl (monitored with Hydrion pH paper). The aqueous mixture was extracted with EtOAc (3 × 50 mL), and the combined organic solution was washed with brine, dried over Na_2SO_4, and concentrated under reduced pressure. The crude residue was chromatographed over silica gel (0−10% CH_3OH in CH_2Cl_2) to give 3-(4-(3,5-dimethyl-1*H*-pyrazol-4-yl)piperazin-1-yl)-2-fluorobenzoic acid (**20f**) as an amorphous white solid (90.0 mg, 63%): ^1H NMR (400 MHz, DMSO-d_6) δ 7.29 (m, 1H), 7.19 (m, 1H), 7.12 (t, J = 9.6 Hz, 1H), 3.03 (br, 8H), 2.12 (s, 6H); ESI MS *m/z* 319 $[M + H]^+$; HPLC 98.3% (AUC), t_R = 10.3 min.

*5-(4-(3,5-Dimethyl-1H-pyrazol-4-yl)piperazin-1-yl)-2-fluorobenzoic Acid (**20g**). Step A.* A mixture of *tert*-butyl piperazine-1-carboxylate (**15**, 0.700 g, 3.75 mmol) and methyl 5-bromo-2-fluorobenzoate (0.787 g, 3.38 mmol) in anhydrous 1,4-dioxane (50 mL) was degassed with N_2 for 5 min. Cs_2CO_3 (3.6 g, 11.04 mmol), X-Phos (0.212 g, 0.44 mmol), and $Pd_2(dba)_3{\cdot}CHCl_3$ (0.192 g, 0.186 mmol) were then added, and the mixture was stirred in a sealed tube at 110 °C for 16 h. The mixture was allowed to cool to rt and then concentrated under reduced pressure. The resulting residue was chromatographed over silica gel (0−30% EtOAc in hexanes) to give *tert*-butyl 4-(4-fluoro-3-(methoxycarbonyl)phenyl)piperazine-1-carboxylate (**16h**) as a yellow oil (1.05 g, 83%). The material was used as is in the next step: ESI MS *m/z* 339 $[M + H]^+$.

Step B. To a 0 °C cooled solution of *tert*-butyl 4-(4-fluoro-3-(methoxycarbonyl)phenyl)piperazine-1-carboxylate (**16h**, 1.2 g, 3.55 mmol) in CH_2Cl_2 (30 mL) was added TFA (5.0 mL, 65.33 mmol), and the resulting solution was stirred at rt for 3 h while gradually warming to rt. The mixture was then concentrated under reduced pressure and diluted with H_2O (30 mL), basified with saturated aqueous $NaHCO_3$ solution (50 mL), and extracted with EtOAc (3 × 50 mL). The combined organic extracts were washed with brine (50 mL), dried over Na_2SO_4, filtered, and concentrated under reduced pressure. The crude material was triturated with Et_2O and filtered to give pure methyl 2-fluoro-5-(piperazin-1-yl)benzoate (**17h**) as a white solid (0.540 g, 64%, crude): ESI MS *m/z* 239 $[M + H]^+$.

Step C. To a 0 °C cooled solution of methyl 2-fluoro-5-(piperazin-1-yl)benzoate (**17h**, 0.300 g, 1.26 mmol) in anhydrous THF (3 mL) were added *i*-Pr_2NEt (0.5 mL, 2.87 mmol) and 3-chloropentane-2,4-dione (0.30 mL, 2.66 mmol) simultaneously, and the resulting solution was stirred for 16 h under a N_2 atmosphere while gradually warming to rt. Upon *in situ* formation of **18h** (monitored by LC-MS; ESI MS *m/z* 337 $[M + H]^+$), $N_2H_4{\cdot}H_2O$ (0.16 mL, 1.89 mmol, 64−65% solution in H_2O) was then added and the mixture was continued to stir at rt for an additional 1 h. The mixture was then diluted with H_2O (50 mL) and extracted with EtOAc (3 × 50 mL). The combined organic extracts were washed with brine, dried over Na_2SO_4, filtered, and concentrated under reduced pressure. The resulting crude residue was chromatographed over silica gel (0−10% CH_3OH in CH_2Cl_2) to give methyl 5-(4-(3,5-dimethyl-1*H*-pyrazol-4-yl)piperazin-1-yl)-2-fluorobenzoate (**19h**) as a brown oil along with an inseparable and uncharacterized impurity (0.140 g, 33%, crude): ESI MS *m/z* 333 $[M + H]^+$.

Step D. To a solution of methyl 5-(4-(3,5-dimethyl-1*H*-pyrazol-4-yl)piperazin-1-yl)-2-fluorobenzoate (**19h**, 0.140 g, 0.421 mmol) in CH_3OH (4 mL), THF (4 mL) and H_2O (2 mL) was added anhydrous LiOH (99.4 mg, 4.15 mmol). The reaction mixture was stirred at rt for 16 h and concentrated under reduced pressure. The aqueous layer was then diluted with H_2O (30 mL) and neutralized to approximately pH = 7 with 2 N aqueous HCl (monitored with Hydrion pH paper). The aqueous mixture was extracted with EtOAc (3 × 50 mL), and the combined organic solution was washed with brine, dried over Na_2SO_4, and concentrated under reduced pressure. The crude residue was chromatographed over silica gel (0−10% CH_3OH in CH_2Cl_2) to give 5-(4-(3,5-dimethyl-1*H*-pyrazol-4-yl)piperazin-1-yl)-2-fluorobenzoic acid (**20g**) as an amorphous white solid (75.0 mg, 56%): ^1H NMR (400 MHz, DMSO-d_6) δ 7.29 (m, 1H), 7.19 (m, 1H), 7.12 (t, J = 9.6 Hz, 1H), 3.13 (br, 4H), 2.99 (br, 4H), 2.10 (s, 6H); ESI MS *m/z* 319 $[M + H]^+$; HPLC >99% (AUC), t_R = 10.6 min.

*3-(4-(3,5-Dimethyl-1H-pyrazol-4-yl)piperazin-1-yl)-5-fluorobenzoic Acid (**20h**). Step A.* A mixture of *tert*-butyl piperazine-1-carboxylate (**15**, 0.700 g, 3.75 mmol) and methyl 3-bromo-5-fluorobenzoate (0.787 g, 3.38 mmol) in anhydrous 1,4-dioxane (50 mL) was degassed with N_2 for 5 min. Cs_2CO_3 (3.6 g, 11.04 mmol), X-Phos (0.212 g, 0.44 mmol), and $Pd_2(dba)_3{\cdot}CHCl_3$ (0.192 g, 0.186 mmol) were then added, and the mixture was stirred in a sealed tube at 110 °C for 16 h. The mixture was allowed to cool to rt and then concentrated under reduced pressure. The resulting residue was chromatographed over silica gel (0−30% EtOAc in hexanes) to give *tert*-butyl 4-(3-fluoro-5-(methoxycarbonyl)phenyl)piperazine-1-carboxylate (**16i**) as a brown oil (0.800 g, 70%): ^1H NMR (400 MHz, acetone-d_6) δ 7.39 (s, 1H), 7.08 (d, J = 8.4 Hz, 1H), 6.97 (d, J = 12.0 Hz, 1H), 3.87 (s, 3H), 3.56 (brs, 4 h), 3.26 (brs, 4 h), 1.45 (s, 9H): ESI MS *m/z* 339 $[M + H]^+$.

Step B. To a 0 °C cooled solution of *tert*-butyl 4-(3-fluoro-5-(methoxycarbonyl)phenyl)piperazine-1-carboxylate (**16i**, 0.800 g, 2.37 mmol) in CH_2Cl_2 (30 mL) was added TFA (3.0 mL, 39.20 mmol), and the resulting solution was stirred at rt for 3 h while gradually warming to rt. The mixture was then concentrated under reduced pressure and diluted with H_2O (30 mL), basified with saturated aqueous $NaHCO_3$ solution (50 mL), and extracted with EtOAc (3 × 50 mL). The combined organic extracts were washed with brine (50 mL), dried over Na_2SO_4, filtered, and concentrated under reduced pressure. The crude material was triturated with Et_2O and filtered to give pure methyl 3-fluoro-5-(piperazin-1-yl)benzoate (**17i**) as an off-white solid (0.540 g, 96%, crude): ESI MS *m/z* 239 $[M + H]^+$.

Step C. To a 0 °C cooled solution of methyl 3-fluoro-5-(piperazin-1-yl)benzoate (**17i**, 0.500 g, 2.09 mmol) in anhydrous THF (10 mL) were added *i*-Pr_2NEt (1.0 mL, 5.74 mmol) and 3-chloropentane-2,4-dione (0.545 mL, 4.83 mmol) simultaneously, and the resulting solution was stirred for 16 h under a N_2 atmosphere while gradually warming to rt. Upon *in situ* formation of **18i** (monitored by LC-MS; ESI MS *m/z* 337 $[M + H]^+$), $N_2H_4{\cdot}H_2O$ (0.26 mL, 3.15 mmol, 64−65% solution in H_2O) was then added and the mixture was continued to stir at rt for an additional 1 h. The mixture was then diluted with H_2O (50

https://doi.org/10.1021/acs.jmedchem.1c00099
J. Med. Chem. 2021, 64, 9010−9041

mL) and extracted with EtOAc (3 × 50 mL). The combined organic extracts were washed with brine, dried over Na_2SO_4, filtered, and concentrated under reduced pressure. The resulting crude residue was chromatographed over silica gel (0−10% CH_3OH in CH_2Cl_2) to give methyl 3-(4-(3,5-dimethyl-1*H*-pyrazol-4-yl)piperazin-1-yl)-5-fluorobenzoate (**19i**) as a brown oil along with an inseparable and uncharacterized impurity (0.230 g, 33%, crude): ESI MS *m/z* 337 [M + H]$^+$.

Step D. To a solution of methyl 3-(4-(3,5-dimethyl-1*H*-pyrazol-4-yl)piperazin-1-yl)-5-fluorobenzoate (**19i**, 0.230 g, 0.692 mmol) in CH_3OH (4 mL), THF (4 mL), and H_2O (2 mL) was added anhydrous LiOH (0.166 g, 6.93 mmol). The reaction mixture was stirred at rt for 3 h and concentrated under reduced pressure. The aqueous layer was then diluted with H_2O (30 mL) and neutralized to approximately pH = 7 with 2 N aqueous HCl (monitored with Hydrion pH paper). The aqueous mixture was extracted with EtOAc (3 × 50 mL), and the combined organic solution was washed with brine, dried over Na_2SO_4, and concentrated under reduced pressure. The crude residue was chromatographed over silica gel (0−10% CH_3OH in CH_2Cl_2) to give 3-(4-(3,5-dimethyl-1*H*-pyrazol-4-yl)piperazin-1-yl)-5-fluorobenzoic acid (**20h**) as an amorphous off-white solid (90.0 mg, 41%): ^{1}H NMR (400 MHz, DMSO-d_6) δ 7.28 (s, 1H), 6.99 (m, 2H), 3.24 (m, 4H), 2,98 (m, 4H), 2.10 (s, 6H); ESI MS *m/z* 319 [M + H]$^+$; HPLC 97.6% (AUC), t_R = 11.3 min.

*5-(4-(3,5-Dimethyl-1H-pyrazol-4-yl)piperazin-1-yl)-4-fluoro-2-methylbenzoic Acid (**20i**). Step A.* A mixture of *tert*-butyl piperazine-1-carboxylate (**15**, 0.771 g, 4.13 mmol) and methyl 5-bromo-4-fluoro-2-methylbenzoate (0.930 g, 3.76 mmol) in anhydrous 1,4-dioxane (50 mL) was degassed with N_2 for 5 min. Cs_2CO_3 (3.70 g, 11.35 mmol), X-Phos (0.213 g, 0.446 mmol), and $Pd_2(dba)_3{\cdot}CHCl_3$ (0.218 g, 0.211 mmol) were then added, and the mixture was stirred in a sealed tube at 110 °C for 16 h. The mixture was allowed to cool to rt and then concentrated under reduced pressure. The resulting residue was chromatographed over silica gel (0−30% EtOAc in hexanes) to give *tert*-butyl 4-(2-fluoro-5-(methoxycarbonyl)-4-methylphenyl)-piperazine-1-carboxylate (**16j**) as a brown oil (0.260 g, 18%). The material was used as is in the next step: ESI MS *m/z* 353 [M + H]$^+$.

Step B. To a 0 °C cooled solution of *tert*-butyl 4-(2-fluoro-5-(methoxycarbonyl)-4-methylphenyl)piperazine-1-carboxylate (**16j**, 0.250 g, 1.34 mmol) in CH_2Cl_2 (30 mL) was added TFA (3.0 mL, 39.20 mmol), and the resulting solution was stirred at rt for 3 h while gradually warming to rt. The mixture was then concentrated under reduced pressure and diluted with H_2O (30 mL), basified with saturated aqueous $NaHCO_3$ solution (50 mL), and extracted with EtOAc (3 × 50 mL). The combined organic extracts were washed with brine (50 mL), dried over Na_2SO_4, filtered, and concentrated under reduced pressure. The crude material was triturated with Et_2O and filtered to give pure methyl 4-fluoro-2-methyl-5-(piperazin-1-yl)-benzoate (**17j**) as a brown oil (0.160 g, 47%, crude): ESI MS *m/z* 253 [M + H]$^+$.

Step C. To a 0 °C cooled solution of methyl 4-fluoro-2-methyl-5-(piperazin-1-yl)benzoate (**17j**, 0.150 g, 0.594 mmol) in anhydrous THF (5 mL) were added *i*-Pr_2NEt (0.54 mL, 3.10 mmol) and 3-chloropentane-2,4-dione (0.20 mL, 1.77 mmol) simultaneously, and the resulting solution was stirred for 16 h under a N_2 atmosphere while gradually warming to rt. Upon *in situ* formation of **18j** (monitored by LC-MS; ESI MS *m/z* 351 [M + H]$^+$), $N_2H_4{\cdot}H_2O$ (0.5 mL, 5.95 mmol, 64−65% solution in H_2O) was then added and the mixture was continued to stir at rt for an additional 1 h. The mixture was then diluted with H_2O (50 mL) and extracted with EtOAc (3 × 50 mL). The combined organic extracts were washed with brine, dried over Na_2SO_4, filtered, and concentrated under reduced pressure. The resulting crude residue was chromatographed over silica gel (0−10% CH_3OH in CH_2Cl_2) to give methyl 5-(4-(3,5-dimethyl-1*H*-pyrazol-4-yl)piperazin-1-yl)-4-fluoro-2-methylbenzoate (**19j**) as a brown oil along with an inseparable and uncharacterized impurity (0.140 g, 68%, crude): ESI MS *m/z* 347 [M + H]$^+$.

Step D. To a solution of methyl 5-(4-(3,5-dimethyl-1*H*-pyrazol-4-yl)piperazin-1-yl)-4-fluoro-2-methylbenzoate (**19j**, 0.140 g, 0.404 mmol) in CH_3OH (4 mL), THF (4 mL), and H_2O (2 mL) was added anhydrous LiOH (48.3 mg, 2.02 mmol). The reaction mixture was stirred at rt for 3 h and concentrated under reduced pressure. The aqueous layer was then diluted with H_2O (30 mL) and neutralized to approximately pH = 7 with 2 N aqueous HCl (monitored with Hydrion pH paper). The aqueous mixture was extracted with EtOAc (3 × 50 mL), and the combined organic solution was washed with brine, dried over Na_2SO_4, and concentrated under reduced pressure. The crude residue was chromatographed over silica gel (0−10% CH_3OH in CH_2Cl_2) to give 5-(4-(3,5-dimethyl-1*H*-pyrazol-4-yl)piperazin-1-yl)-4-fluoro-2-methylbenzoic acid (**20i**) as an amorphous off-white solid (14.6 mg, 11%): ^{1}H NMR (400 MHz, DMSO-d_6) δ 7.52 (d, *J* = 8.4 Hz, 1H), 7.13 (d, *J* = 13.2 Hz, 1H), 3.04 (br, 8H), 2.45 (s, 1H), 2.13 (s, 6H); ESI MS *m/z* 333 [M + H]$^+$; HPLC 98.7% (AUC), t_R = 11.6 min.

*3-(4-(3,5-Dimethyl-1H-pyrazol-4-yl)piperazin-1-yl)-4-iodobenzoic Acid (**26**). Step A.* A mixture of *tert*-butyl piperazine-1-carboxylate (**15**, 1.05 g, 5.63 mmol), ethyl 3-fluoro-4-nitrobenzoate (1.0 g, 4.69 mmol), and K_2CO_3 (1.3 g, 9.38 mmol) in anhydrous CH_3CN (20 mL) was heated at 60 °C for 16 h under an atmosphere of N_2. The mixture was then allowed to cool to rt and concentrated under reduced pressure. The resulting residue was diluted with H_2O (50 mL), and the aqueous mixture was extracted with EtOAc (3 × 75 mL). The combined organic extracts were washed with brine, dried over Na_2SO_4, filtered, and concentrated under reduced pressure. The crude residue was chromatographed over silica gel (0−15% EtOAc in hexanes) to give *tert*-butyl 4-(5-(ethoxycarbonyl)-2-nitrophenyl)piperazine-1-carboxylate (**21**) as an orange oil (1.6 g, 90%): ^{1}H NMR (400 MHz, acetone-d_6) δ 7.89−7.87 (m, 2H), 7.76 (d, *J* = 8.0 Hz, 1H), 4.38 (q, 2H), 3.54 (brs, 4H), 3.08 (brs, 4H), 1.42 (s, 9H), 1.37 (t, *J* = 6.8 Hz, 3H); ESI MS *m/z* 380 [M + H]$^+$.

Step B. A mixture of *tert*-butyl 4-(5-(ethoxycarbonyl)-2-nitrophenyl)piperazine-1-carboxylate (**21**, 1.6 g, 4.21 mmol) and Pd/C (10% w/w, 0.160 g) in anhydrous EtOH (30 mL) was stirred at rt under an atmosphere of H_2 gas *via* balloon (1 atm of pressure) for 24 h. The mixture was filtered through a pad of CELITE pad with repeat rinsing using anhydrous EtOH. The filtrate was concentrated under reduced pressure, and the resulting crude residue was chromatographed over silica gel (0−25% EtOAc in hexanes) to give *tert*-butyl 4-(2-amino-5-(ethoxycarbonyl)phenyl)piperazine-1-carboxylate (**22**) as a white solid (1.3 g, 88%): ^{1}H NMR (400 MHz, acetone-d_6) δ 7.60 (s, 1H), 7.57 (d, *J* = 8.8 Hz, 1H), 6.77 (d, *J* = 8.0 Hz, 1H), 5.30 (brs, 2H), 4.24 (q, 2H), 3.57 (brs, 4H), 2.89 (brs, 4H), 1.43 (s, 9H), 1.30 (t, *J* = 6.8 Hz, 3H): ESI MS *m/z* 350 [M + H]$^+$.

Step C. A mixture of *tert*-butyl 4-(2-amino-5-(ethoxycarbonyl)-phenyl)piperazine-1-carboxylate (**22**, 0.500 g, 1.43 mmol) dissolved in 3 N aqueous H_2SO_4 (5.7 mL, 0.25 M) was cooled to 0 °C. A solution of $NaNO_2$ (0.108 g, 1.57 mmol) in H_2O (10 mL) was added dropwise slowly at 0 °C over a period of 30 min. A solution of KI (0.356 mg, 2.15 mmol) and urea (17.2 mg, 0.29 mmol) in H_2O (5 mL) was subsequently added, and the resulting mixture was continued to stir at 0 °C for an additional 1 h. The mixture was then quenched *via* addition of 10% $NaHCO_3$ (50 mL) and extracted with ethyl acetate (3 × 50 mL). The organic extracts were dried over Na_2SO_4, filtered, and concentrated under reduced pressure. The resulting crude residue was dissolved in CH_2Cl_2 (10 mL) and cooled to 0 °C. TFA (3 mL, 39.2 mmol) was added, and the resulting solution was stirred for 3 h, gradually warming to rt. The mixture was concentrated under reduced pressure and diluted with H_2O (30 mL), basified with saturated $NaHCO_3$ solution, and extracted with EtOAc (3 × 50 mL). The combined organic extracts were washed with brine, dried over Na_2SO_4, filtered, and concentrated under reduced pressure to give crude ethyl 4-iodo-3-(piperazin-1-yl)benzoate (**23**) as a brown oil, which was carried forward as is without further purification (0.300 g, 58%, crude): ESI MS *m/z* 361[M + H]$^+$.

Step D. To a 0 °C cooled solution of crude ethyl 4-iodo-3-(piperazin-1-yl)benzoate (**23**, 0.300 g, 0.83 mmol) in THF (6 mL) were added *i*-Pr_2NEt (0.75 mL, 4.30 mmol) and 3-chloropentane-2,4-dione (0.28 mL, 2.48 mmol) simultaneously, and the resulting solution was stirred at rt for 16 h. Upon *in situ* formation of **24** (monitored by LC-MS; ESI MS *m/z* 459 [M + H]$^+$), $N_2H_4{\cdot}H_2O$ (0.5 mL, 5.95 mmol, 64−65% solution in H_2O) was then added and the mixture was continued to stir

https://doi.org/10.1021/acs.jmedchem.1c00099
J. Med. Chem. 2021, 64, 9010−9041

at rt for an additional 1 h. The mixture was then diluted with H_2O (50 mL) and extracted with EtOAc (3 × 50 mL). The combined organic extracts were washed with brine, dried over Na_2SO_4, filtered, and concentrated under reduced pressure. The resulting crude residue was chromatographed over silica gel (0−10% CH_3OH in CH_2Cl_2) to give ethyl 3-(4-(3,5-dimethyl-1*H*-pyrazol-4-yl)piperazin-1-yl)-4-iodobenzoate (**25**) as a brown oil, which was carried forward as is without further purification (0.200 g, 53%, crude).

Step E. To a solution of ethyl 3-(4-(3,5-dimethyl-1*H*-pyrazol-4-yl)piperazin-1-yl)-4-iodobenzoate (**25**, 0.200 g, 0.44 mmol) in EtOH (4 mL), THF (4 mL) and H_2O (2 mL) was added anhydrous LiOH (0.105 g, 4.38 mmol). The reaction mixture was stirred at rt for 3 h and concentrated under reduced pressure. The resulting aqueous mixture was diluted with H_2O (10 mL) and acidified with 2 N HCl to pH 3. The mixture was extracted with EtOAc (3 × 50 mL), and the combined organic extracts were washed with brine, dried over Na_2SO_4, and concentrated under reduced pressure. The resulting crude residue was chromatographed over silica gel (0−10% CH_3OH in CH_2Cl_2) to give 3-(4-(3,5-dimethyl-1*H*-pyrazol-4-yl)piperazin-1-yl)-4-iodobenzoic acid (**26**) as an off-white solid (80.0 mg, 43%): ^{1}H NMR (acetone-d_6, 400 MHz) δ 7.95 (d, J = 8.0 Hz, 1H), 7.58 (s, 1H), 7.34 (d, J = 8.4 Hz, 2H), 3.12−3.10 (m, 4H), 3.03−2.98 (m, 4H), 2.11 (s, 6H); ESI MS m/z 427 $[M + H]^+$.

*3-((3aR,6aS)-5-(3,5-Dimethyl-1H-pyrazol-4-yl)hexahydropyrrolo-[3,4-c]pyrrol-2(1H)-yl)-4-fluorobenzoic Acid (**32**). Step A.* A mixture of *tert*-butyl (3a*R*,6a*S*)-hexahydropyrrolo[3,4-*c*]pyrrole-2(1*H*)-carboxylate (**27**, 1.0 g, 4.71 mmol) and methyl 3-bromo-4-fluorobenzoate (1.0 g, 4.29 mmol) in anhydrous 1,4-dioxane (50 mL) was degassed with N_2 for 5 min. Cs_2CO_3 (4.17 g, 12.8 mmol), X-Phos (0.240 g, 0.503 mmol), and $Pd_2(dba)_3{\cdot}CHCl_3$ (0.248 g, 0.240 mmol) were then added, and the mixture was stirred in a sealed tube at 110 °C for 16 h. The mixture was allowed to cool to rt and then concentrated under reduced pressure. The resulting residue was chromatographed over silica gel (0−30% EtOAc in hexanes) to give *tert*-butyl (3a*R*,6a*S*)-5-(2-fluoro-5-(methoxycarbonyl)phenyl)hexahydropyrrolo[3,4-*c*]pyrrole-2(1*H*)-carboxylate (**28**) as a brown oil (0.400 g, 26%): ^{1}H NMR (400 MHz, acetone-d_6) δ 7.37−7.35 (m, 2H), 7.14−7.08 (m, 1H), 3.88 (s, 3H), 3.61 (brs, 4H), 3.36−3.29 (m, 4H), 3.03 (brs, 2H), 1.38 (s, 9H); ESI MS m/z 365 $[M + H]^+$.

Step B. To a 0 °C cooled solution of *tert*-butyl (3a*R*,6a*S*)-5-(2-fluoro-5-(methoxycarbonyl)phenyl)hexahydropyrrolo[3,4-*c*]pyrrole-2(1*H*)-carboxylate (**28**, 0.390 g, 1.07 mmol) in CH_2Cl_2 (30 mL) was added TFA (5.0 mL, 65.33 mmol), and the resulting solution was stirred at rt for 3 h while gradually warming to rt. The mixture was then concentrated under reduced pressure and diluted with H_2O (30 mL), basified with saturated aqueous $NaHCO_3$ solution (50 mL), and extracted with EtOAc (3 × 50 mL). The combined organic extracts were washed with brine (50 mL), dried over Na_2SO_4, filtered, and concentrated under reduced pressure. The crude material was triturated with Et_2O and filtered to give pure methyl 4-fluoro-3-((3a*R*,6a*S*)-hexahydropyrrolo[3,4-*c*]pyrrol-2(1*H*)-yl)benzoate (**29**) as a brown solid (0.220 mg, 78%, crude): ESI MS m/z 265 $[M + H]^+$.

Step C. To a 0 °C cooled solution of methyl 4-fluoro-3-((3a*R*,6a*S*)-hexahydropyrrolo[3,4-*c*]pyrrol-2(1*H*)-yl)benzoate (**29**, 0.210 g, 0.79 mmol) in anhydrous THF (10 mL) were added *i*-Pr_2NEt (0.73 mL, 4.19 mmol) and 3-chloropentane-2,4-dione (0.27 mL, 2.39 mmol) simultaneously, and the resulting solution was stirred for 16 h under a N_2 atmosphere while gradually warming to rt. Upon *in situ* formation of diketone **30** (monitored by LC-MS; ESI MS m/z 337 $[M + H]^+$), $N_2H_4{\cdot}H_2O$ (0.26 mL, 3.15 mmol, 64−65% solution in H_2O) was then added and the mixture was continued to stir at rt for an additional 1 h. The mixture was then diluted with H_2O (50 mL) and extracted with EtOAc (3 × 50 mL). The combined organic extracts were washed with brine, dried over Na_2SO_4, filtered, and concentrated under reduced pressure. The resulting crude residue was chromatographed over silica gel (0−10% CH_3OH in CH_2Cl_2) to give 3-((3a*R*,6a*S*)-5-(3,5-dimethyl-1*H*-pyrazol-4-yl)hexahydropyrrolo[3,4-*c*]pyrrol-2(1*H*)-yl)-4-fluorobenzoate (**31**) as a brown oil along with an inseparable and uncharacterized impurity (0.100 g, 35%, crude): ESI MS m/z 359 $[M + H]^+$.

Step D. To a solution of methyl 3-((3a*R*,6a*S*)-5-(3,5-dimethyl-1*H*-pyrazol-4-yl)hexahydropyrrolo[3,4-*c*]pyrrol-2(1*H*)-yl)-4-fluorobenzoate (**31**, 60.0 mg, 0.16 mmol) in CH_3OH (4 mL), THF (4 mL), and H_2O (2 mL) was added anhydrous LiOH (20.0 mg, 0.84 mmol). The reaction mixture was stirred at rt for 3 h and concentrated under reduced pressure. The aqueous layer was then diluted with H_2O (30 mL) and neutralized to approximately pH = 7 with 2 N aqueous HCl (monitored with Hydrion pH paper). The aqueous mixture was extracted with EtOAc (3 × 50 mL), and the combined organic solution was washed with brine, dried over Na_2SO_4, and concentrated under reduced pressure. The crude residue was chromatographed over silica gel (0−10% CH_3OH in CH_2Cl_2) to give 3-((3a*R*,6a*S*)-5-(3,5-dimethyl-1*H*-pyrazol-4-yl)hexahydropyrrolo[3,4-*c*]pyrrol-2(1*H*)-yl)-4-fluorobenzoic acid (**32**) as an amorphous off-white solid (4.8 mg, 8.7%): ^{1}H NMR (400 MHz, DMSO-d_6) δ 7.40 (m, 2H), 7.16 (m, 1H), 3.60 (m, 2H), 3.20 (m, 2H), 3.01 (m, 2H), 2.88 (m, 4H), 2.11 (s, 6H); ESI MS m/z 345 $[M + H]^+$; HPLC 95.4% (AUC), t_R = 11.0 min.

*(±)-3-(7-(3,5-Dimethyl-1H-pyrazol-4-yl)-2,7-diazaspiro[4.4]-nonan-2-yl)-4-fluorobenzoic Acid ((±)-**38**). Step A.* A mixture of (±)-*tert*-butyl 2,7-diazaspiro[4.4]nonane-2-carboxylate ((±)-**33**, 1.07 g, 4.72 mmol) and methyl 3-bromo-4-fluorobenzoate (1.0 g, 4.29 mmol) in anhydrous 1,4-dioxane (50 mL) was degassed with N_2 for 5 min. Cs_2CO_3 (4.16 g, 12.84 mmol), X-Phos (240 mg, 0.51 mmol), and $Pd_2(dba)_3{\cdot}CHCl_3$ (0.217 g, 0.21 mmol) were then added, and the mixture was stirred in a sealed tube at 110 °C for 16 h. The mixture was allowed to cool to rt and then concentrated under reduced pressure. The resulting residue was chromatographed over silica gel (0−30% EtOAc in hexanes) to give (±)-*tert*-butyl 7-(2-fluoro-5-(methoxycarbonyl)phenyl)-2,7-diazaspiro[4.4]nonane-2-carboxylate ((±)-**34**) as a yellow solid (0.480 g, 30%): ^{1}H NMR (400 MHz, acetone-d_6) δ 7.33−7.31 (m, 2H), 7.12−7.07 (m, 1H), 3.84 (s, 3H), 3.56−3.44 (m, 2H), 3.42−3.27 (m, 6H), 1.99−1.91 (m, 4H), 1.42 (s, 9H); ESI MS m/z 379 $[M + H]^+$.

Step B. To a 0 °C cooled solution of (±)-*tert*-butyl 7-(2-fluoro-5-(methoxycarbonyl)phenyl)-2,7-diazaspiro[4.4]nonane-2-carboxylate ((±)-**34**, 0.470 g, 1.24 mmol) in CH_2Cl_2 (30 mL) was added TFA (3.0 mL, 39.20 mmol), and the resulting solution was stirred at rt for 16 h while gradually warming to rt. The mixture was then concentrated under reduced pressure and diluted with H_2O (30 mL), basified with saturated aqueous $NaHCO_3$ solution (50 mL), and extracted with EtOAc (3 × 50 mL). The combined organic extracts were washed with brine (50 mL), dried over Na_2SO_4, filtered, and concentrated under reduced pressure. The crude material was triturated with Et_2O and filtered to give pure (±)-methyl 4-fluoro-3-(2,7-diazaspiro[4.4]nonan-2-yl)benzoate ((±)-**35**) as a white solid (0.340 g, 99%, crude): ESI MS m/z 279 $[M + H]^+$.

Step C. To a 0 °C cooled solution of (±)-methyl 4-fluoro-3-(2,7-diazaspiro[4.4]nonan-2-yl)benzoate ((±)-**35**, 0.340 g, 1.22 mmol) in anhydrous THF (10 mL) were added *i*-Pr_2NEt (1.1 mL, 6.31 mmol) and 3-chloropentane-2,4-dione (0.40 mL, 3.66 mmol) simultaneously, and the resulting solution was stirred for 16 h under a N_2 atmosphere while gradually warming to rt. Upon *in situ* formation of (±)-**36** (monitored by LC-MS; ESI MS m/z 377 $[M + H]^+$), $N_2H_4{\cdot}H_2O$ (0.62 mL, 12.23 mmol, 64−65% solution in H_2O) was then added and the mixture was continued to stir at rt for an additional 1 h. The mixture was then diluted with H_2O (50 mL) and extracted with EtOAc (3 × 50 mL). The combined organic extracts were washed with brine, dried over Na_2SO_4, filtered, and concentrated under reduced pressure. The resulting crude residue was chromatographed over silica gel (0−10% CH_3OH in CH_2Cl_2) to give (±)-methyl 3-(7-(3,5-dimethyl-1*H*-pyrazol-4-yl)-2,7-diazaspiro[4.4]nonan-2-yl)-4-fluorobenzoate ((±)-**37**) as a brown oil (65.0 mg, 14%, crude): ESI MS m/z 373 $[M + H]^+$.

Step D. To a solution of (±)-methyl 3-(7-(3,5-dimethyl-1*H*-pyrazol-4-yl)-2,7-diazaspiro[4.4]nonan-2-yl)-4-fluorobenzoate ((±)-**37**, 60.0 mg, 0.16 mmol) in CH_3OH (4 mL), THF (4 mL), and H_2O (2 mL) was added anhydrous LiOH (19.2 mg, 0.81 mmol). The reaction mixture was stirred at rt for 16 h and concentrated under reduced pressure. The aqueous layer was then diluted with H_2O (30 mL) and neutralized to approximately pH = 7 with 2 N aqueous HCl (monitored with Hydrion

https://doi.org/10.1021/acs.jmedchem.1c00099
J. Med. Chem. 2021, 64, 9010−9041

pH paper). The aqueous mixture was extracted with EtOAc (3 × 50 mL) and the combined organic solution was washed with brine, dried over Na_2SO_4, and concentrated under reduced pressure. The crude residue was chromatographed over silica gel (0−10% CH_3OH in CH_2Cl_2) to give (±)-3-(7-(3,5-dimethyl-1*H*-pyrazol-4-yl)-2,7-diazaspiro[4.4]nonan-2-yl)-4-fluorobenzoic acid ((±)-**38**) as an amorphous white solid (10.5 mg, 18%): ^{1}H NMR (400 MHz, DMSO-d_6) δ 7.25 (m, 2H), 7.14 (m, 1H), 3.46 (m, 4H), 3.02 (m, 2H), 2.99 (m, 2H), 2.11 (s, 6H), 1.94−1.87 (m, 4); ESI MS *m/z* 359 [M + H]$^+$; HPLC 97.3% (AUC), t_R = 11.3 min.

*3-(6-(3,5-Dimethyl-1H-pyrazol-4-yl)-2,6-diazaspiro[3.3]heptan-2-yl)-4-fluorobenzoic Acid (**44**). Step A.* A mixture of *tert*-butyl 2,6-diazaspiro[3.3]heptane-2-carboxylate (**39**, 1.0 g, 5.04 mmol) and methyl 3-bromo-4-fluorobenzoate (2.25 g, 9.65 mmol) in anhydrous 1,4-dioxane (50 mL) was degassed with N_2 for 5 min. Cs_2CO_3 (4.17 g, 12.79 mmol), X-Phos (0.240 g, 0.50 mmol) and $Pd_2(dba)_3{\cdot}CHCl_3$ (0.248 g, 0.24 mmol) were then added and the mixture was stirred in a sealed tube at 110 °C for 16 h. The mixture was allowed to cool to rt and then concentrated under reduced pressure. The resulting residue was chromatographed over silica gel (0−30% EtOAc in hexanes) to give *tert*-butyl 6-(2-fluoro-5-(methoxycarbonyl)phenyl)-2,6-diazaspiro-[3.3]heptane-2-carboxylate (**40**) as a brown oil (1.34 g, 76%): ^{1}H NMR (acetone-d_6, 400 MHz) δ 7.39−7.35 (m, 1 H), 7.11−7.05 (m, 2 H), 4.13 (s, 3 H), 4.12−4.09 (m, 4 H), 3.85−3.78 (m, 4 H), 1.37 (s, 9 H); ESI MS *m/z* 351 [M + H]$^+$.

Step B. To a 0 °C cooled solution of *tert*-butyl 6-(2-fluoro-5-(methoxycarbonyl)phenyl)-2,6-diazaspiro[3.3]heptane-2-carboxylate (**40**, 1.30 g, 3.71 mmol) in CH_2Cl_2 (30 mL) was added TFA (5.0 mL, 65.33 mmol) and the resulting solution was stirred at rt for 3 h while gradually warming to rt. The mixture was then concentrated under reduced pressure and diluted with H_2O (30 mL), basified with saturated aqueous $NaHCO_3$ solution (50 mL), and extracted with EtOAc (3 × 50 mL). The combined organic extracts were washed with brine (50 mL), dried over Na_2SO_4, filtered, and concentrated under reduced pressure. The crude material was triturated with Et_2O and filtered to give pure methyl 4-fluoro-3-(2,6-diazaspiro[3.3]heptan-2-yl)benzoate (**41**) as a brown oil (0.600 g, 65%, crude): ESI MS *m/z* 251 [M + H]$^+$.

Step C. To a 0 °C cooled solution of methyl 4-fluoro-3-(2,6-diazaspiro[3.3]heptan-2-yl)benzoate (**41**, 0.600 g, 1.65 mmol) in anhydrous THF (5 mL) were added *i*-Pr_2NEt (1.37 mL, 7.89 mmol) and 3-chloropentane-2,4-dione (0.55 mL, 4.91 mmol) simultaneously and the resulting solution was stirred for 16 h under N_2 atmosphere while gradually warming to rt. Upon *in situ* formation of **42** (monitored by LC-MS; ESI MS *m/z* 349 [M + H]$^+$), $N_2H_4{\cdot}H_2O$ (0.82 g, 16.5 mmol, 64−65% solution in H_2O) was then added and the mixture continued to stir at rt for an additional 1 h. The mixture was then diluted with H_2O (50 mL) and extracted with EtOAc (3 × 50 mL). The combined organic extracts were washed with brine, dried over Na_2SO_4, filtered, and concentrated under reduced pressure. The resulting crude residue was chromatographed over silica gel (0−10% CH_3OH in CH_2Cl_2) to give 3-(6-(3,5-dimethyl-1*H*-pyrazol-4-yl)-2,6-diazaspiro-[3.3]heptan-2-yl)-4-fluorobenzoate (**43**) as a brown oil (0.100 g, 18%): ESI MS *m/z* 345 [M + H]$^+$.

Step D. To a solution of methyl 3-(6-(3,5-dimethyl-1*H*-pyrazol-4-yl)-2,6-diazaspiro[3.3]heptan-2-yl)-4-fluorobenzoate (**43**, 51.0 mg, 0.14 mmol) in CH_3OH (4 mL), THF (4 mL) and H_2O (2 mL) was added anhydrous LiOH (17.0 mg, 0.70 mmol). The reaction mixture was stirred at rt for 16 h and was concentrated under reduced pressure. The aqueous layer was then diluted with H_2O (30 mL) and neutralized to approximately pH = 7 with 2 N aqueous HCl (monitored with Hydrion pH paper). The aqueous mixture was extracted with EtOAc (3 × 50 mL), and the combined organic solution was washed with brine, dried over Na_2SO_4, and concentrated under reduced pressure. The crude residue was chromatographed over silica gel (0−10% CH_3OH in CH_2Cl_2) to give 3-(6-(3,5-dimethyl-1*H*-pyrazol-4-yl)-2,6-diazaspiro-[3.3]heptan-2-yl)-4-fluorobenzoic acid (**44**) as an amorphous white solid (13.0 mg, 26%): ^{1}H NMR (400 MHz, DMSO-d_6) δ 7.31 (m, 1H), 7.17 (t, *J* = 9.2 Hz, 1H), 7.7 (d, *J* = 8.4 Hz, 1H), 4.09 (m, 4H), 3.96 (m, 4H), 2.10 (s, 6H); ESI MS *m/z* 331 [M + H]$^+$; HPLC 98.8% (AUC), t_R = 10.7 min.

*3-(4-(3,5-Dimethylisoxazol-4-yl)piperazin-1-yl)-4-fluorobenzoic Acid (**46**). Step A.* To a solution of methyl 3-(4-(2,4-dioxopentan-3-yl)piperazin-1-yl)-4-fluorobenzoate (**18a**, 80.0 mg, 0.23 mmol) in CH_3OH (2 mL) was added $NH_2OH{\cdot}HCl$ (32.0 mg, 0.47 mmol), and the resulting solution was stirred at rt for 16 h. The mixture was concentrated under reduced pressure, and the resulting residue was chromatographed over silica gel (0−50% EtOAc in hexanes) to give methyl 3-(4-(3,5-dimethylisoxazol-4-yl)piperazin-1-yl)-4-fluorobenzoate (**45**) as a brown solid (20.1 mg, 25%); ESI MS *m/z* 334 [M + H]$^+$.

Step B. To a solution of methyl 3-(4-(3,5-dimethylisoxazol-4-yl)piperazin-1-yl)-4-fluorobenzoate (**45**, 8.1 mg, 0.023 mmol) in CH_3OH (1 mL), THF (1 mL), and H_2O (0.5 mL) was added anhydrous LiOH (2.7 mg, 0.11 mmol). The reaction mixture was stirred at rt for 1 h and then concentrated under reduced pressure. The aqueous layer was diluted with H_2O (15 mL) and neutralized with 2 N aqueous HCl. The aqueous mixture was extracted with EtOAc (3 × 10 mL), and the combined organic extracts were washed with brine, dried over Na_2SO_4, filtered, and concentrated under reduced pressure. The resulting residue was chromatographed over silica gel (0−10% CH_3OH in CH_2Cl_2) to give 3-(4-(3,5-dimethylisoxazol-4-yl)piperazin-1-yl)-4-fluorobenzoic acid (**46**) as a white solid (2.5 mg, 34%): ^{1}H NMR (400 MHz, DMSO-d_6) δ 7.71−7.59 (m, 1H), 7.19−7.10 (m, 2H), 3.18−3.3.17 (m, 4H), 3.12−3.11 (m, 4H), 2.38 (s, 3H), 2.25 (s, 3H); ESI MS *m/z* 320 [M + H]$^+$; HPLC 96.8% (AUC), t_R = 13.7 min.

*3-(4-(2H-Tetrazol-5-yl)piperazin-1-yl)-4-fluorobenzoic Acid (**48**). Step A.* To a 0 °C cooled solution of methyl 4-fluoro-3-(piperazin-1-yl)benzoate (**17a**, 0.200 g, 0.84 mmol) and *i*-Pr_2NEt (0.5 mL, 2.52 mmol) in THF (3 mL) was added CNBr (0.106 g, 1.01 mmol), and the mixture was stirred for 1 h while gradually warming to rt. The mixture was concentrated under reduced pressure, and the residue was dissolved in DMF (3 mL). To this solution were added NH_4Cl (0.449 g, 8.4 mmol) and NaN_3 (0.546 g, 8.4 mmol), and the resulting mixture was heated at 120 °C for 12 h. The mixture was then allowed to cool to rt, diluted with H_2O (10 mL), and extracted with EtOAc (3 × 50 mL). The combined organic extracts were washed with brine, dried over Na_2SO_4, filtered, and concentrated under reduced pressure to give methyl 3-(4-(2*H*-tetrazol-5-yl)piperazin-1-yl)-4-fluorobenzoate (**47**) (0.160 g, 62%), which was taken into the next step as is without purification: ESI MS *m/z* 307 [M + H]$^+$.

Step B. To a solution of methyl 3-(4-(2*H*-tetrazol-5-yl)piperazin-1-yl)-4-fluorobenzoate (**47**, 0.160 g, 0.52 mmol) in CH_3OH (4 mL), THF (4 mL), and H_2O (2 mL) was added anhydrous LiOH (0.125 g, 5.2 mmol), and the resulting mixture was stirred at rt for 1 h. The mixture was then concentrated under reduced pressure, and the aqueous layer was diluted with H_2O (15 mL) and acidified to pH = 3 with 2 N aqueous HCl. The aqueous mixture was then extracted with EtOAc (3 × 10 mL), and the combined organic extracts were washed with brine, dried over Na_2SO_4, filtered, and concentrated under reduced pressure. The resulting residue was chromatographed over silica gel (0−10% CH_3OH in CH_2Cl_2) to give 3-(4-(2*H*-tetrazol-5-yl)piperazin-1-yl)-4-fluorobenzoic acid (**48**) as a white solid (80.2 mg, 53%): ^{1}H NMR (400 MHz, DMSO-d_6) δ 7.59 (m, 2H), 7.25 (dd, *J* = 7.6, 3.6 Hz, 1H), 3.52 (br, 4H), 3.14 (br, 4H); ESI MS *m/z* 293 [M + H]$^+$; HPLC 98.3% (AUC), t_R = 11.3 min.

*4-Fluoro-3-(4-(2-(trifluoromethyl)phenyl)piperazin-1-yl)benzoic Acid (**50**). Step A.* A mixture of methyl 4-fluoro-3-(piperazin-1-yl)benzoate (**17a**, 0.200 g, 0.84 mmol) and 1-bromo-2-(trifluoromethyl)benzene (0.263 g, 1.17 mmol) in anhydrous 1,4-dioxane (10 mL) was degassed with N_2 for 5 min. Cs_2CO_3 (0.816 g, 2.50 mmol), X-Phos (79.1 mg, 0.16 mmol), and $Pd_2(dba)_3{\cdot}CHCl_3$ (73.2 mg, 0.08 mmol) were then added, and the reaction mixture was stirred at reflux for 16 h under an atmosphere of N_2. The mixture was allowed to cool to rt and concentrated under reduced pressure. The resulting residue was chromatographed over silica gel (0−30% EtOAc in hexanes) to give methyl 4-fluoro-3-(4-(2-(trifluoromethyl)phenyl)-piperazin-1-yl)benzoate (**49**) (30.2 mg, 9%) as a brown solid: ^{1}H NMR (400 MHz, $CDCl_3$) δ 7.69−7.63 (m, 3H), 7.61−7.60 (m, 1H), 7.52−

https://doi.org/10.1021/acs.jmedchem.1c00099
J. Med. Chem. 2021, 64, 9010−9041

7.41 (m, 1H), 7.08−7.03 (m, 2H), 3.88 (m, 3H), 3.25−3.23 (m, 4H), 3.10−3.08 (m, 4H); ESI MS m/z 383 $[M + H]^+$.

Step B. To a solution of methyl 4-fluoro-3-(4-(2-(trifluoromethyl)-phenyl)piperazin-1-yl)benzoate (**49**, 30.0 mg, 0.78 mmol) in CH_3OH (4 mL), THF (4 mL), and H_2O (2 mL) was added anhydrous LiOH (9 mg, 0.39 mmol). The mixture was stirred at rt for 1 h and then concentrated under reduced pressure. The aqueous layer was diluted with H_2O (10 mL) and acidified to pH = 3 with 2 N aqueous HCl. The aqueous mixture was extracted with EtOAc (3 × 10 mL), and the combined organic extracts were washed with brine, dried over Na_2SO_4, filtered, and concentrated under reduced pressure. The resulting residue was chromatographed over silica gel (0−10% CH_3OH in CH_2Cl_2) to give 4-fluoro-3-(4-(2-(trifluoromethyl)phenyl)piperazin-1-yl)benzoic acid (**50**) as a white solid (15.2 mg, 53%): ^{1}H NMR (400 MHz, $CDCl_3$) δ 7.76−7.72 (m, 2H), 7.64 (d, J = 8.0 Hz, 1H), 7.52−7.50 (m, 1H), 7.42 (d, J = 8.0 Hz, 1H), 7.23 (m, 1H), 7.10 (dd, J = 8.0, 4.0 Hz, 1H), 3.26 (m, 4H), 3.11 (m, 4H); ESI MS m/z 369 $[M + H]^+$; HPLC 96.7% (AUC), t_R = 16.0 min.

*4-Fluoro-3-(4-((3-methyl-1H-pyrazol-5-yl)methyl)piperazin-1-yl)-benzoic Acid (**52**). Step A.* A solution of methyl 4-fluoro-3-(piperazin-1-yl)benzoate (**17a**, 0.200 g, 0.84 mmol) and 3-methyl-1*H*-pyrazole-5-carbaldehyde (0.111 g, 1.0 mmol) in 1,2-dichloroethane (5 mL) and HOAc (0.01 mL, 0.17 mmol) was stirred at rt for 1 h. $NaBH(OAc)_3$ (0.267 g, 1.26 mmol) was then added, and the mixture was stirred for 12 h at 60 °C. The mixture was then allowed to cool to rt and diluted with CH_2Cl_2 (10 mL). The organic mixture was washed with saturated aqueous $NaHCO_3$ (10 mL), H_2O (10 mL), and brine. The organic layer was then dried over Na_2SO_4, filtered, and concentrated under reduced pressure. The resulting residue was chromatographed over silica gel (0−10% CH_3OH in CH_2Cl_2) to give methyl 4-fluoro-3-(4-((3-methyl-1*H*-pyrazol-5-yl)methyl)piperazin-1-yl)benzoate (**51**) as a white solid (0.210 g, 76%): ESI MS m/z 333 $[M + H]^+$.

Step B. To a solution of methyl 4-fluoro-3-(4-((3-methyl-1*H*-pyrazol-5-yl)methyl)piperazin-1-yl)benzoate (**51**, 0.200 g, 0.60 mmol) in CH_3OH (4 mL), THF (4 mL), and H_2O (2 mL) was added anhydrous LiOH (144.5 mg, 6.0 mmol), and the resulting mixture was stirred at rt for 3 h. The mixture was concentrated under reduced pressure, and the resulting aqueous layer was diluted with H_2O (10 mL) and neutralized with 2 N aqueous HCl. The aqueous mixture was then extracted with EtOAc (13 × 10 mL), and the combined organic extracts were washed with brine, dried over Na_2SO_4, filtered, and concentrated under reduced pressure. The resulting residue was chromatographed over silica gel (0−10% CH_3OH in CH_2Cl_2) to give 4-fluoro-3-(4-((3-methyl-1*H*-pyrazol-5-yl)methyl)piperazin-1-yl)benzoic acid (**52**) as a white solid (0.120 g, 63%): ^{1}H NMR (400 MHz, DMSO-d_6) δ 7.50−7.46 (m, 2H), 7.33 (s, 1H), 7.13 (dd, J = 8.8, 4.0 Hz, 1H), 3.30 (s, 2H), 2.95 (br, 4H), 2.45 (br, 4H), 2.12 (s, 3H); ESI MS m/z 319 $[M + H]^+$; HPLC 98.7% (AUC), t_R = 10.2 min.

*3-(4-(3,5-Dimethyl-1H-pyrazol-4-yl)piperazin-1-yl)-4-fluorobenzamide (**53**). Step A.* To a mixture of 3-(4-(3,5-dimethyl-1*H*-pyrazol-4-yl)piperazin-1-yl)-4-fluorobenzoic acid (**14**, 0.100 g, 0.314 mmol), HBTU (0.178 g, 0.471 mmol), and *i*-Pr_2NEt (0.218 mL, 1.26 mmol) in DMF (4 mL) was added NH_4Cl (16.7 mg, 0.314 mmol). The resulting solution was stirred at rt for 18 h under an atmosphere of N_2. The mixture was diluted with H_2O (10 mL) and extracted with EtOAc (3 × 20 mL). The combined organic extracts were washed with H_2O (3 × 20 mL) and brine, dried over Na_2SO_4, filtered, and concentrated under reduced pressure. The resulting crude residue was chromatographed over silica gel (0−80% EtOAc in hexanes) to give 3-(4-(3,5-dimethyl-1*H*-pyrazol-4-yl)piperazin-1-yl)-4-fluorobenzamide (**53**) as a white solid (71.7 mg, 72%): ^{1}H NMR (400 MHz, DMSO-d_6) δ 11.84 (br, 1H), 7.94 (bs, 1H), 7.54-7,48 (m, 2H), 7.31 (s, 1H), 7.14 (m, 1H), 3.06−3.01 (m, 8H), 2.10 (s, 6H); ESI MS m/z 318 $[M + H]^+$; HPLC >99% (AUC), t_R = 10.5 min.

*1-(3,5-Dimethyl-1H-pyrazol-4-yl)-4-(2-fluoro-5-(2H-tetrazol-5-yl)phenyl)piperazine (**54**). Step A.* A mixture of 3-(4-(3,5-dimethyl-1*H*-pyrazol-4-yl)piperazin-1-yl)-4-fluorobenzamide (**53**, 0.180 g, 0.526 mmol), NaN_3 (0.142 g, 0.375 mmol), and tetrachlorosilane (98.5 mg, 0.579 mmol) in CH_3CN (4 mL) was stirred at 80 °C for 18 h in a sealed vessel. The reaction mixture was allowed to cool to rt and diluted with saturated $NaHCO_3$ (5 mL). The aqueous mixture was extracted with $CHCl_3$ (3 × 50 mL), and the combined organic extracts were washed with brine (50 mL), dried over Na_2SO_4, filtered, and concentrated under reduced pressure. The resulting residue was chromatographed over silica gel (0−10% CH_3OH in CH_2Cl_2) to give 1-(3,5-dimethyl-1*H*-pyrazol-4-yl)-4-(2-fluoro-5-(2H-tetrazol-5-yl)phenyl)piperazine (**54**) as a white solid (60.3 mg, 30%): ^{1}H NMR (400 MHz, DMSO-d_6) δ 7.69 (m, 1H), 7.67 (m, 1H), 7.36−7. (dd, J = 4, 8.4 Hz, 1H); 3.12 (m, 4H), 3.09 (m, 4H), 2.13 (s, 6H); ESI MS m/z 343 $[M + H]^+$; HPLC >99% (AUC), t_R = 11.1 min.

■ ASSOCIATED CONTENT

Supporting Information

The Supporting Information is available free of charge at https://pubs.acs.org/doi/10.1021/acs.jmedchem.1c00099.

TTR in vitro assay information, RBP4 *in vitro* assay information, mouse PK information, serum RBP4 measurement information, *in vitro* ADME assay information, general chemistry information, and spectroscopic and analytical data for compounds **14** (^{1}H NMR, ^{13}C NMR, ^{19}F NMR, MS, HRMS, and HPLC), **20c**, and **20e** (^{1}H NMR, MS, and HPLC) and all of the remaining biologically tested compounds (HPLC), and molecular formula strings for biologically tested compounds (PDF)

■ AUTHOR INFORMATION

Corresponding Authors

Christopher L. Cioffi − *Departments of Basic and Clinical Sciences and Pharmaceutical Sciences, Albany College of Pharmacy and Health Sciences, Albany, New York 12208, United States*; orcid.org/0000-0003-0642-7905; Phone: 518-694-7224; Email: christopher.cioffi@acphs.edu

Konstantin Petrukhin − *Department of Ophthalmology, Columbia University Medical Center, New York 10032, United States*; Phone: 212-305-9040; Email: kep4@cumc.columbia.edu

Authors

Arun Raja − *Departments of Basic and Clinical Sciences and Pharmaceutical Sciences, Albany College of Pharmacy and Health Sciences, Albany, New York 12208, United States*

Parthasarathy Muthuraman − *Departments of Basic and Clinical Sciences and Pharmaceutical Sciences, Albany College of Pharmacy and Health Sciences, Albany, New York 12208, United States*

Aravindan Jayaraman − *Departments of Basic and Clinical Sciences and Pharmaceutical Sciences, Albany College of Pharmacy and Health Sciences, Albany, New York 12208, United States*

Srinivasan Jayakumar − *Departments of Basic and Clinical Sciences and Pharmaceutical Sciences, Albany College of Pharmacy and Health Sciences, Albany, New York 12208, United States*

Andras Varadi − *Department of Ophthalmology, Columbia University Medical Center, New York 10032, United States*

Boglarka Racz − *Department of Ophthalmology, Columbia University Medical Center, New York 10032, United States*

Complete contact information is available at: https://pubs.acs.org/10.1021/acs.jmedchem.1c00099

Notes

The authors declare no competing financial interest.

ACKNOWLEDGMENTS

Research reported in this publication was supported by the National Eye Institute of the National Institutes of Health under Award Number R01EY028549. The content is solely the responsibility of the authors and does not necessarily represent the official views of the National Institutes of Health. This project has been funded in whole or in part with Federal funds from the National Eye Institute, the National Institutes of Health, the Department of Health and Human Services, NIH Grant R01EY028549 (to K.P. and C.L.C.). This study was supported by NIH Grant P30 EY019007 (Core Support for Vision Research) and unrestricted funds from the Research to Prevent Blindness (New York, NY) to the Department of Ophthalmology, Columbia University.

ABBREVIATIONS

Aβ, β-amyloid; *Abca*4, ATP-binding cassette, subfamily A (ABC), member 4; ADME, absorption, distribution, metabolism, elimination; AMD, age-related macular degeneration; Arg, arginine; Asn, asparagine; ATTR, transthyretin amyloidosis; ATTR-CM, transthyretin amyloidosis cardiomyopathy; ATTR-PN, transthyretin amyloidosis polyneuropathy; AUC, area under the curve; CH_2Cl_2, dichloromethane; CH_3CN, acetonitrile; CH_3OH, methyl alcohol; CL, clearance; CL_{int}, intrinsic clearance; Cs_2CO_3, cesium carbonate; CSF, cerebrospinal fluid; CYP, cytochrome P450; DMF, *N*,*N*-dimethylformamide; Et_2O, diethyl ether; EtOAc, ethyl acetate; %*F*, % oral bioavailability; FAC, familial amyloid cardiomyopathy; FAP, familial amyloid neuropathy; FITC, fluorescein isothiocyanate; FP, fluorescence polarization; Glu, glutamic acid; Gly, glycine; h, hour(s); HBP, halogen binding pocket; HBTU, (2-(1*H*-benzotriazol-1-yl)-1,1,3,3-tetramethyluronium hexafluorophosphate; $N_2H_4{\cdot}H_2O$, hydrazine hydrate; HCl, hydrochloric acid; hERG, human ether-a-go-go channel; HLM, human liver microsomes; HOAc, acetic acid; HRMS, high-resolution mass spectrometry; H_2SO_4, sulfuric acid; *i*-Pr_2NEt, *N*,*N*-diisopropylethylamine; Ile, isoleucine; IV, intravenous; K_2CO_3, potassium carbonate; Leu, leucine; LiOH, lithium hydroxide; Lys, lysine; min, minutes; MLM, mouse liver microsomes; $NaBH_4$, sodium borohydride; $NaBH(OAc)_3$, sodium triacetoxyborohydride; NaN_3, sodium azide; $NaNO_2$, sodium nitrite; NH_4Cl, ammonium chloride; PBS, phosphate-buffered saline; PD, pharmacodynamics; PDB, Protein Data Bank; $Pd_2(dba)_3{\cdot}CHCl_3$, Tris-(dibenzylideneacetone)dipalladium(0)-chloroform adduct; Phe, phenylalanine; PK, pharmacokinetics; PO, oral; PPARγ, nuclear peroxisome proliferator-activated receptor-γ; %PPB, % plasma protein binding; RBP4, retinol binding protein-4; RLM, rat liver microsomes; RPE, retinal pigment epithelium; rt, room temperature; SAR, structure−activity relationship; Ser, serine; SPA, scintillation proximity assay; SSA, senile systemic amyloidosis; STD NMR, saturation transfer difference nuclear magnetic resonance; TBG, thyroxine binding globulin; TFA, trifluoroacetic acid; THF, tetrahydrofuran; Thr, threonine; TTR, transthyretin; Trp, tryptophan; Tyr, tyrosine; T4, thyroxine; Val, valine; V_{ss}, volume of distribution at steady state; X-Phos, 2-dicyclohexylphosphino-2′,4′,6′-triisopropylbiphenyl

REFERENCES

(1) Sundaram, M.; Sivaprasadarao, A.; DeSousa, M. M.; Findlay, J. B. The transfer of retinol from serum retinol-binding protein to cellular retinol-binding protein is mediated by a membrane receptor. *J. Biol. Chem.* **1998**, *273*, 3336−3342.

(2) Kawaguchi, R.; Zhong, M.; Kassai, M.; Ter-Stepanian, M.; Sun, H. Vitamin A Transport Mechanism of the Multitransmembrane Cell-Surface Receptor STRA6. *Membranes* **2015**, *5*, 425−453.

(3) Wang, Y.; Connors, R.; Fan, P.; Wang, X.; Wang, Z.; Liu, J.; Kayser, F.; Medina, J. C.; Johnstone, S.; Xu, H.; Thibault, S.; Walker, N.; Conn, M.; Zhang, Y.; Liu, Q.; Grillo, M. P.; Motani, A.; Coward, P.; Wang, Z. Structure-assisted discovery of the first non-retinoid ligands for Retinol-Binding Protein 4. *Bioorg. Med. Chem. Lett.* **2014**, *24*, 2885−2891.

(4) Cioffi, C. L.; Dobri, N.; Freeman, E. E.; Conlon, M. P.; Chen, P.; Stafford, D. G.; Schwarz, D. M.; Golden, K. C.; Zhu, L.; Kitchen, D. B.; Barnes, K. D.; Racz, B.; Qin, Q.; Michelotti, E.; Cywin, C. L.; Martin, W. H.; Pearson, P. G.; Johnson, G.; Petrukhin, K. Design, synthesis, and evaluation of nonretinoid retinol binding protein 4 antagonists for the potential treatment of atrophic age-related macular degeneration and Stargardt disease. *J. Med. Chem.* **2014**, *57*, 7731−7757.

(5) Cioffi, C. L.; Racz, B.; Freeman, E. E.; Conlon, M. P.; Chen, P.; Stafford, D. G.; Schwarz, D. M.; Zhu, L.; Kitchen, D. B.; Barnes, K. D.; Dobri, N.; Michelotti, E.; Cywin, C. L.; Martin, W. H.; Pearson, P. G.; Johnson, G.; Petrukhin, K. Bicyclic [3.3.0]-octahydrocyclopenta[c]-pyrrolo antagonists of retinol binding protein 4: potential treatment of atrophic age-related macular degeneration and Stargardt disease. *J. Med. Chem.* **2015**, *58*, 5863−5888.

(6) Cioffi, C. L.; Racz, B.; Varadi, A.; Freeman, E. E.; Conlon, M. P.; Chen, P.; Zhu, L.; Kitchen, D. B.; Barnes, K. D.; Martin, W. H.; Pearson, P. G.; Johnson, G.; Blaner, W. S.; Petrukhin, K. Design, synthesis, and preclinical efficacy of novel nonretinoid antagonists of retinol-binding protein 4 in the mouse model of hepatic steatosis. *J. Med. Chem.* **2019**, *62*, 5470−5500.

(7) Cioffi, C. L.; Muthuraman, P.; Raja, A.; Varadi, A.; Racz, B.; Petrukhin, K. Discovery of bispecific antagonists of retinol binding protein 4 that stabilize transthyretin tetramers: scaffolding hopping, optimization, and preclinical pharmacological evaluation as a potential therapy for two common age-related comorbidities. *J. Med. Chem.* **2020**, *63*, 11054−11084.

(8) Radu, R. A.; Han, Y.; Bui, T. V.; Nusinowitz, S.; Bok, D.; Lichter, J.; Widder, K.; Travis, G. H.; Mata, N. L. Reductions in serum vitamin A arrest accumulation of toxic retinal fluorophores: a potential therapy for treatment of lipofuscin-based retinal diseases. *Invest. Ophthalmol. Visual Sci.* **2005**, *46*, 4393−43401.

(9) Dobri, N.; Qin, Q.; Kong, J.; Yamamoto, K.; Liu, Z.; Moiseyev, G.; Ma, J. X.; Allikmets, R.; Sparrow, J. R.; Petrukhin, K. A1120, a nonretinoid RBP4 antagonist, inhibits formation of cytotoxic bisretinoids in the animal model of enhanced retinal lipofuscinogenesis. *Invest. Ophthalmol. Visual Sci.* **2013**, *54*, 85−95.

(10) Racz, B.; Varadi, A.; Kong, J.; Allikmets, R.; Pearson, P. G.; Johnson, G.; Cioffi, C. L.; Petrukhin, K. A non-retinoid antagonist of retinol-binding protein 4 rescues phenotype in a model of Stargardt disease without inhibiting the visual cycle. *J. Biol. Chem.* **2018**, *293*, 11574−11588.

(11) Racz, B.; Varadi, A.; Pearson, P. G.; Petrukhin, K. Comparative pharmacokinetics and pharmacodynamics of the advanced retinol-binding protein 4 antagonist in dog and cynomolgus monkey. *PLoS One* **2020**, *15*, No. e0228291.

(12) Gimeno, A.; Santos, L. M.; Alemi, M.; Rivas, J.; Blasi, D.; Cotrina, E. Y.; Llop, J.; Valencia, G.; Cardoso, I.; Quintana, J.; Arsequell, G.; Jimenez-Barbero, J. Insights on the interaction between transthyretin and Aβ in solution. A saturation transfer difference (STD) NMR analysis of the role of iododiflunisal. *J. Med. Chem.* **2017**, *60*, 5749−5758.

(13) Jesus, C. S.; Almeida, Z. L.; Vaz, D. C.; Faria, T. Q.; Brito, R. M. A new folding kinetic mechanism for human transthyretin and the influence of the amyloidogenic V30M mutation. *Int. J. Mol. Sci.* **2016**, *17*, No. 1428.

(14) Damrauer, S. M.; Chaudhary, K.; Cho, J. H.; Liang, L. W.; Argulian, E.; Chan, L.; Dobbyn, A.; Guerraty, M. A.; Judy, R.; Kay, J.; Kember, R. L.; Levin, M. G.; Saha, A.; Van Vleck, T.; Verma, S. S.; Weaver, J.; Abul-Husn, N. S.; Baras, A.; Chirinos, J. A.; Drachman, B.; Kenny, E. E.; Loos, R. J. F.; Narula, J.; Overton, J.; Reid, J.; Ritchie, M.;

Sirugo, G.; Nadkarni, G.; Rader, D. J.; Do, R. Association of the V122I hereditary transthyretin amyloidosis genetic variant with heart failure among individuals of african or hispanic/latino ancestry. *JAMA* **2019**, *322*, 2191−2202.
(15) Liz, M. A.; Coelho, T.; Bellotti, V.; Fernandez-Arias, M. I.; Mallaina, P.; Obici, L. A narrative review of the role of transthyretin in health and disease. *Neurol. Ther.* **2020**, *9*, 395−402.
(16) Sousa, M. M.; Fernandes, R.; Palha, J. A.; Taboada, A.; Vieira, P.; Saraiva, M. J. Evidence for Early Cytotoxic Aggregates in Transgenic Mice for Human Transthyretin Leu55Pro. *Am. J. Pathol.* **2002**, *161*, 1935−1948.
(17) Connors, L. H.; Doros, G.; Sam, F.; Badiee, A.; Seldin, D. C.; Skinner, M. Clinical features and survival in senile systemic amyloidosis: comparison to familial transthyretin cardiomyopathy. *Amyloid* **2011**, *18*, 157−159.
(18) Buxbaum, J. N.; Ruberg, F. L. Transthyretin V122I (pV142I)* cardiac amyloidosis: an age-dependent autosomal dominant cardiomyopathy too common to be overlooked as a cause of significant heart disease in elderly African Americans. *Genet. Med.* **2017**, *19*, 733−742.
(19) Buxbaum, J.; Koziol, J.; Connors, L. H. Serum transthyretin levels in senile systemic amyloidosis: effects of age, gender and ethnicity. *Amyloid* **2008**, *15*, 255−261.
(20) Kanai, M.; Raz, A.; Goodman, D. S. Retinol-binding protein: the transport protein for vitamin A in human plasma. *J. Clin. Invest.* **1968**, *47*, 2025−2044.
(21) Rando, R. R.; Bangerter, F. W. On the labelling of oxidized cell surface membranes by acyl hydrazides. *Biochim. Biophys. Acta, Biomembr.* **1979**, *557*, 354−362.
(22) Vieira, M.; Saraiva, M. J. Transthyretin: a multifaceted protein. *Biomol. Concepts* **2014**, *5*, 45−54.
(23) Kassem, N. A.; Deane, R.; Segal, M. B.; Preston, J. E. Role of transthyretin in thyroxine transfer from cerebrospinal fluid to brain and choroid plexus. *Am. J. Physiol.: Regul., Integr. Comp. Physiol.* **2006**, *291*, R1310−R1315.
(24) Silva, C. S.; Eira, J.; Ribeiro, C. A.; Oliveira, Â.; Sousa, M. M.; Cardoso, I.; Liz, M. A. Transthyretin neuroprotection in Alzheimer's disease is dependent on proteolysis. *Neurobiol. Aging* **2017**, *59*, 10−14.
(25) Gião, T.; Saavedra, J.; Cotrina, E.; Quintana, J.; Llop, J.; Arsequell, G.; Cardoso, I. Undiscovered roles for transthyretin: from a transporter protein to a new therapeutic target for alzheimer's disease. *Int. J. Mol. Sci.* **2020**, *21*, No. 2075.
(26) Sun, X.; Dyson, H. J.; Wright, P. E. Kinetic analysis of the multistep aggregation pathway of human transthyretin. *Proc. Natl. Acad. Sci. U.S.A.* **2018**, *115*, E6201−E6208.
(27) Ruberg, F. L.; Grogan, M.; Hanna, M.; Kelly, J. W.; Maurer, M. S. Transthyretin amyloid cardiomyopathy: JACC state-of-the-art review. *J. Am. Coll. Cardiol.* **2019**, *73*, 2872−2891.
(28) Yamamoto, H.; Yokochi, T. Transthyretin cardiac amyloidosis: an update on diagnosis and treatment. *ESC Heart Fail.* **2019**, *6*, 1128−1139.
(29) Waddington-Cruz, M.; Schmidt, H.; Botteman, M. F.; Carter, J. A.; Stewart, M.; Hopps, M.; Fallet, S.; Amass, L. Epidemiological and clinical characteristics of symptomatic hereditary transthyretin amyloid polyneuropathy: a global case series. *Orphanet J. Rare Dis.* **2019**, *14*, No. 34.
(30) Park, G. Y.; Jamerlan, A.; Shim, K. H.; An, S. S. A. Diagnostic and treatment approaches involving transthyretin in amyloidogenic diseases. *Int. J. Mol. Sci.* **2019**, *20*, No. 2982.
(31) Guo, X.; Nanus, D. M.; Ruiz, A.; Rando, R. R.; Bok, D.; Gudas, L. J. Reduced levels of retinyl esters and vitamin A in human renal cancers. *Cancer Res.* **2001**, *61*, 2774−2781.
(32) Kamata, M.; Susanto, M. T.; Chen, I. S. Enhanced transthyretin tetramer stability following expression of an amyloid disease trans-suppressor variant in mammalian cells. *J. Gene Med.* **2009**, *11*, 103−111.
(33) Mathew, V.; Wang, A. K. Inotersen: new promise for the treatment of hereditary transthyretin amyloidosis. *Drug Des., Dev. Ther.* **2019**, *13*, 1515−1525.
(34) Hoy, S. M. Patisiran: first global approval. *Drugs* **2018**, *78*, 1625−1631.
(35) Bulawa, C. E.; Connelly, S.; Devit, M.; Wang, L.; Weigel, C.; Fleming, J. A.; Packman, J.; Powers, E. T.; Wiseman, R. L.; Foss, T. R.; Wilson, I. A.; Kelly, J. W.; Labaudiniere, R. Tafamidis, a potent and selective transthyretin kinetic stabilizer that inhibits the amyloid cascade. *Proc. Natl. Acad. Sci. U.S.A.* **2012**, *109*, 9629−9634.
(36) Coelho, T.; Merlini, G.; Bulawa, C. E.; Fleming, J. A.; Judge, D. P.; Kelly, J. W.; Maurer, M. S.; Plante-Bordeneuve, V.; Labaudiniere, R.; Mundayat, R.; Riley, S.; Lombardo, I.; Huertas, P. Mechanism of action and clinical application of tafamidis in hereditary transthyretin amyloidosis. *Neurol. Ther.* **2016**, *5*, 1−25.
(37) Coelho, T.; Maia, L. F.; da Silva, A. M.; Cruz, M. W.; Plante-Bordeneuve, V.; Suhr, O. B.; Conceicao, I.; Schmidt, H. H.; Trigo, P.; Kelly, J. W.; Labaudiniere, R.; Chan, J.; Packman, J.; Grogan, D. R. Long-term effects of tafamidis for the treatment of transthyretin familial amyloid polyneuropathy. *J. Neurol.* **2013**, *260*, 2802−2814.
(38) Cruz, M. W. Tafamidis for autonomic neuropathy in hereditary transthyretin (ATTR) amyloidosis: a review. *Clin. Auton. Res.* **2019**, *29*, 19−24.
(39) Lamb, Y. N.; Deeks, E. D. Tafamidis: a review in transthyretin amyloidosis with polyneuropathy. *Drugs* **2019**, *79*, 863−874.
(40) Park, J.; Egolum, U.; Parker, S.; Andrews, E.; Ombengi, D.; Ling, H. Tafamidis: a first-in-class transthyretin stabilizer for transthyretin amyloid cardiomyopathy. *Ann. Pharmacother.* **2020**, *54*, 470−477.
(41) Alhamadsheh, M. M.; Connelly, S.; Cho, A.; Reixach, N.; Powers, E. T.; Pan, D. W.; Wilson, I. A.; Kelly, J. W.; Graef, I. A. Potent kinetic stabilizers that prevent transthyretin-mediated cardiomyocyte proteotoxicity. *Sci. Transl. Med.* **2011**, *3*, No. 97ra81.
(42) Miller, M.; Pal, A.; Albusairi, W.; Joo, H.; Pappas, B.; Haque Tuhin, M. T.; Liang, D.; Jampala, R.; Liu, F.; Khan, J.; Faaij, M.; Park, M.; Chan, W.; Graef, I.; Zamboni, R.; Kumar, N.; Fox, J.; Sinha, U.; Alhamadsheh, M. enthalpy-driven stabilization of transthyretin by AG10 mimics a naturally occurring genetic variant that protects from transthyretin amyloidosis. *J. Med. Chem.* **2018**, *61*, 7862−7876.
(43) Penchala, S. C.; Connelly, S.; Wang, Y.; Park, M. S.; Zhao, L.; Baranczak, A.; Rappley, I.; Vogel, H.; Liedtke, M.; Witteles, R. M.; Powers, E. T.; Reixach, N.; Chan, W. K.; Wilson, I. A.; Kelly, J. W.; Graef, I. A.; Alhamadsheh, M. M. AG10 inhibits amyloidogenesis and cellular toxicity of the familial amyloid cardiomyopathy-associated V122I transthyretin. *Proc. Natl. Acad. Sci. U.S.A.* **2013**, *110*, 9992−9997.
(44) Maurer, M. S.; Schwartz, J. H.; Gundapaneni, B.; Elliott, P. M.; Merlini, G.; Waddington-Cruz, M.; Kristen, A. V.; Grogan, M.; Witteles, R.; Damy, T.; Drachman, B. M.; Shah, S. J.; Hanna, M.; Judge, D. P.; Barsdorf, A. I.; Huber, P.; Patterson, T. A.; Riley, S.; Schumacher, J.; Stewart, M.; Sultan, M. B.; Rapezzi, C. Tafamidis treatment for patients with transthyretin amyloid cardiomyopathy. *N. Engl. J. Med.* **2018**, *379*, 1007−1016.
(45) Judge, D. P.; Heitner, S. B.; Falk, R. H.; Maurer, M. S.; Shah, S. J.; Witteles, R. M.; Grogan, M.; Selby, V. N.; Jacoby, D.; Hanna, M.; Nativi-Nicolau, J.; Patel, J.; Rao, S.; Sinha, U.; Turtle, C. W.; Fox, J. C. Transthyretin stabilization by AG10 in symptomatic transthyretin amyloid cardiomyopathy. *J. Am. Coll. Cardiol.* **2019**, *74*, 285−295.
(46) Monteiro, C.; Mesgazardeh, J. S.; Anselmo, J.; Fernandes, J.; Novais, M.; Rodrigues, C.; Brighty, G. J.; Powers, D. L.; Powers, E. T.; Coelho, T.; Kelly, J. W. Predictive model of response to tafamidis in hereditary ATTR polyneuropathy. *JCI Insight* **2019**, *4*, No. e126526.
(47) Berk, J. L.; Suhr, O. B.; Obici, L.; Sekijima, Y.; Zeldenrust, S. R.; Yamashita, T.; Heneghan, M. A.; Gorevic, P. D.; Litchy, W. J.; Wiesman, J. F.; Nordh, E.; Corato, M.; Lozza, A.; Cortese, A.; Robinson-Papp, J.; Colton, T.; Rybin, D. V.; Bisbee, A. B.; Ando, Y.; Ikeda, S.; Seldin, D. C.; Merlini, G.; Skinner, M.; Kelly, J. W.; Dyck, P. J.; Diflunisal Trial Consortium. Repurposing diflunisal for familial amyloid polyneuropathy: a randomized clinical trial. *JAMA* **2013**, *310*, 2658−2667.
(48) Sant'Anna, R.; Gallego, P.; Robinson, L. Z.; Pereira-Henriques, A.; Ferreira, N.; Pinheiro, F.; Esperante, S.; Pallares, I.; Huertas, O.; Almeida, M. R.; Reixach, N.; Insa, R.; Velazquez-Campoy, A.; Reverter, D.; Reig, N.; Ventura, S. Repositioning tolcapone as a potent inhibitor

of transthyretin amyloidogenesis and associated cellular toxicity. *Nat. Commun.* **2016**, *7*, No. 10787.

(49) Vilaró, M.; Nieto, J.; La Parra, J. R.; Almeida, M. R.; Ballesteros, A.; Planas, A.; Arsequell, G.; Valencia, G. Tuning transthyretin amyloidosis inhibition properties of iododiflunisal by combinatorial engineering of the nonsalicylic ring substitutions. *ACS Comb. Sci.* **2015**, *17*, 32−38.

(50) Jahng, W. J.; Cheung, E.; Rando, R. R. Lecithin retinol acyltransferase forms functional homodimers. *Biochemistry* **2002**, *41*, 6311−6319.

(51) Wang, H.; Tang, Y.; Lei, M. Models for binding cooperativities of inhibitors with transthyretin. *Arch. Biochem. Biophys.* **2007**, *466*, 85−97.

(52) Rando, R. R.; Orr, G. A.; Bangerter, F. W. Threshold effects on the concanavalin A-mediated agglutination of modified erythrocytes. *J. Biol. Chem.* **1979**, *254*, 8318−8323.

(53) Johnson, S. M.; Petrassi, H. M.; Palaninathan, S. K.; Mohamedmohaideen, N. N.; Purkey, H. E.; Nichols, C.; Chiang, K. P.; Walkup, T.; Sacchettini, J. C.; Sharpless, K. B.; Kelly, J. W. Bisaryloxime ethers as potent inhibitors of transthyretin amyloid fibril formation. *J. Med. Chem.* **2005**, *48*, 1576−1587.

(54) Petrukhin, K. Tranthyretin ligands capable of inhibitng retinol-dependent RBP4-TTR interaction for treatment of age-related macular degneration, Stargardt disease, and other retinal disease characterized by excessive lipofuscin accumulation. US2015/0057320A1, Feb 26, 2015.

(55) Cotrina, E. Y.; Oliveira, A.; Leite, J. P.; Llop, J.; Gales, L.; Quintana, J.; Cardoso, I.; Arsequell, G. Repurposing benzbromarone for familial amyloid polyneuropathy: a new transthyretin tetramer stabilizer. *Int. J. Mol. Sci.* **2020**, *21*, No. 7166.

(56) Rando, R. R.; Bangerter, F. W. Threshold effects on the lectin-mediated aggregation of synthetic glycolipid-containing liposomes. *J. Supramol. Struct.* **1979**, *11*, 295−309.

(57) Orr, G. A.; Rando, R. R.; Bangerter, F. W. Synthetic glycolipids and the lectin-mediated aggregation of liposomes. *J. Biol. Chem.* **1979**, *254*, 4721−4725.

(58) Zanotti, G.; Folli, C.; Cendron, L.; Alfieri, B.; Nishida, S. K.; Gliubich, F.; Pasquato, N.; Negro, A.; Berni, R. Structural and mutational analyses of protein-protein interactions between transthyretin and retinol-binding protein. *FEBS J.* **2008**, *275*, 5841−5854.

(59) Orr, G. A.; Rando, R. R. Synthetic concanavalin A receptors and erythrocyte agglutination. *Nature* **1978**, *272*, 722−725.

(60) Campos-Sandoval, J. A.; Redondo, C.; Kinsella, G. K.; Pal, A.; Jones, G.; Eyre, G. S.; Hirst, S. C.; Findlay, J. B. Fenretinide derivatives act as disrupters of interactions of serum retinol binding protein (sRBP) with transthyretin and the sRBP receptor. *J. Med. Chem.* **2011**, *54*, 4378−4387.

(61) Fox, J. C.; Hellawell, J. L.; Rao, S.; O'Reilly, T.; Lumpkin, R.; Jernelius, J.; Gretler, D.; Sinha, U. First-in-human study of AG10, a novel, oral, specific, selective, and potent transthyretin stabilizer for the treatment of transthyretin amyloidosis: a phase 1 safety, tolerability, pharmacokinetic, and pharmacodynamic study in healthy adult volunteers. *Clin. Pharmacol. Drug Dev.* **2020**, *9*, 115−129.

(62) Regan, S. L.; Maggs, J. L.; Hammond, T. G.; Lambert, C.; Williams, D. P.; Park, B. K. Acyl glucuronides: the good, the bad and the ugly. *Biopharm. Drug Dispos.* **2010**, *31*, 367−395.

(63) Bäurle, S.; Nagel, J.; Peters, O.; Brauer, N.; Ter Laak, A.; Preusse, C.; Rottmann, A.; Heldmann, D.; Bothe, U.; Blume, T.; Zorn, L.; Walter, D.; Zollner, T. M.; Steinmeyer, A.; Langer, G. Identification of a benzimidazolecarboxylic acid derivative (BAY 1316957) as a potent and selective human prostaglandin e2 receptor subtype 4 (hEP4-R) antagonist for the treatment of endometriosis. *J. Med. Chem.* **2019**, *62*, 2541−2563.

(64) Ahmadian, M.; Suh, J. M.; Hah, N.; Liddle, C.; Atkins, A. R.; Downes, M.; Evans, R. M. PPARgamma signaling and metabolism: the good, the bad and the future. *Nat. Med.* **2013**, *19*, 557−566.

(65) Niemietz, C.; Fleischhauer, L.; Sandfort, V.; Guttmann, S.; Zibert, A.; Schmidt, H. H. Hepatocyte-like cells reveal novel role of SERPINA1 in transthyretin amyloidosis. *J. Cell Sci.* **2018**, *131*, No. jcs219824.

(66) Klabunde, T.; Petrassi, H. M.; Oza, V. B.; Raman, P.; Kelly, J. W.; Sacchettini, J. C. Rational design of potent human transthyretin amyloid disease inhibitors. *Nat. Struct. Biol.* **2000**, *7*, 312−321.

(67) Sekijima, Y.; Wiseman, R. L.; Matteson, J.; Hammarstrom, P.; Miller, S. R.; Sawkar, A. R.; Balch, W. E.; Kelly, J. W. The biological and chemical basis for tissue-selective amyloid disease. *Cell* **2005**, *121*, 73−85.

(68) Radu, R. A.; Han, Y.; Bui, T. V.; Nusinowitz, S.; Bok, D.; Lichter, J.; Widder, K.; Travis, G. H.; Mata, N. L. Reductions in serum vitamin A arrest accumulation of toxic retinal fluorophores: a potential therapy for treatment of lipofuscin-based retinal diseases. *Invest. Ophthalmol. Visual Sci.* **2005**, *46*, 4393−4401.

(69) Dobri, N.; Qin, Q.; Kong, J.; Yamamoto, K.; Liu, Z.; Moiseyev, G.; Ma, J.-X.; Allikmets, R.; Sparrow, J. R.; Petrukhin, K. A1120, a Nonretinoid RBP4 Antagonist, Inhibits Formation of Cytotoxic Bisretinoids in the Animal Model of Enhanced Retinal Lipofuscinogenesis. *Invest. Ophthalmol. Visual Sci.* **2013**, *54*, 85−95.

(70) Haselhorst, T.; Lamerz, A.-C.; Itzstein, M. V. Saturation transfer difference NMR spectroscopy as a technique to investigate protein-carbohydrate interactions in solution. *Methods Mol. Biol.* **2009**, *534*, 375−386.

https://doi.org/10.1021/acs.jmedchem.1c00099
J. Med. Chem. 2021, 64, 9010−9041